University of Strathclyde, Glasgow

Department of Naval Architecture, Ocean and Marine Engineering

Numerical Study on Hydrodynamic Performance of Bio-mimetic Locomotion

By

Jianxin Hu

A thesis submitted in fulfilment of the requirements for the degree of Doctor of Philosophy

2016

Declaration

This thesis is the result of the author's original research. It has been composed by the author and has not been previously submitted for examination which has led to the award of a degree.

The copyright of this thesis belongs to the author under the terms of the United Kingdom Copyright Acts as qualified by University of Strathclyde Regulation 3.51. Due acknowledgement must always be made of the use of any material contained in, or derived from, this thesis.

Jianxin Hu

Signature: *Jianxin HU* Date: 21 Dec. 2016

Acknowledgements

I would like to thank my leading supervisor, Dr. Qing Xiao, for her guidance and support throughout all phases of this research work. She is the most important person who leads me to the field of academia. She delivers rigorous training on improving my ability to learn, and provides precious opportunities for developing my future career. It has been a privilege to work with and learn from her. I would always follow her trace for achieving those professional records, which represents an impressive way of being a successful female researcher.

I would also like to show my gratitude to my second supervisor, Professor Atilla Incecik. With his expertise, optimism and generosity he gave me constant opportunities and invaluable advice in all aspects. He is not only a mentor who guides me the ways for proper career, but also a friend who encourage me pursing for better life.

I would like formally acknowledge Dr Jing Lou and Dr Vinh Tan Nguyen in A*STAR in Singapore, who provide me position for exchanging study, and Professor Frederic Boyer and Dr. Mathieu Porez in IRCCyN in France, who give me opportunity for collaboration. I thoroughly enjoyed these experiences, and have benefited greatly from it.

I am grateful to the faculty and staff in the department, especially Thelma Will, who is always eager to offer help with smile, for their kind support and help.

I wish to express my gratitude to my colleagues in the department, for many useful discussions and help. I would also like to thank all my friends in Glasgow, for enlightening me and bringing fun to my life.

Table of Contents

List of Figures

List of Tables

Abstract

Inspired by the novel flapping caudal fin and body undulatory mechanisms in nature swimmers, simplified physical models are built in Computational Fluid Dynamic (CFD) solvers, and used to investigate the self-propulsion performance under different conditions with various kinetic and geometric parameters. Two simplified physical models, three-dimensional flapping wing model with flexibilities in lateral and rotational directions and multi-body system model with rigid components connected by revolute joints, are investigated for mimicking typical bio-inspired locomotion.

The study was firstly carried out on a three-dimensional wing with a freedom in translational direction under a prescribed flapping motion. The investigation focused on how the system kinematics and structural parameters affect the dynamic response of a wing with a relatively small span length. It shows that the induced wing motion is a result of the system stability breakdown, which has only been observed by previous researches in the two-dimensional case. The results obtained indicate that the evolution of the wing locomotion is controlled not only by the flapping frequency and amplitude, but also influenced by the system inertia as well as the wing aspect ratio and density ratio. Moreover, initial perturbation effect on wings flexibility plays a role in the evolution development.

Subsequently, a comprehensive investigation is carried out on the dynamics response of a three-dimensional flapping wing with two degree of freedoms in lateral and rotational direction under a zero initial velocity condition. Distinguishing from the limited existing studies, present work performs a systematic examination on the effects of wing aspect ratio, inertia, torsional stiffness and pivot point on the dynamics response of a low aspect ratio rectangular wing under an initial zero speed flow field

condition. The reduced rotational pitching help with the symmetry breakdown of the flapping wing and results in a forward/backward motion. When the wing reaches its stable periodic state, the induced pitching frequency is identical to its forced flapping frequency. However, depending on various kinematic and dynamic system parameters, (i.e. flapping frequency, density ratio and pitching axis), the lateral induced velocity shows a number of different oscillating frequency. Furthermore, compared with one degree of freedom wing in lateral direction only, the propulsion performance of such a two degree of freedom wing relies very much on the magnitude of torsional stiffness adding on the pivot point, as well as its pitching axis. In all cases examined, thrust force and moment generated by a long span wing is larger than that of a short wing, which is remarkably linked to the strong reverse von Kármán vortex street formed in the wake of a wing.

In a separate study, the undulatory motion of fish body is mimicked with a series of linked rigid bodies, i.e. a multi-body system. The connection between two adjacent rigid components can be modelled as the revolute hinge joint, with either a passively induced pitch motion or actively prescribed pitch motion. Emphasis is put on the development for solving the problems of coupling multi-body dynamics with fluid dynamics by implementing Mobile Multi-body System (MMS) algorithm with CFD solver. Verifications are carried out by repeating the previous work, and innovative cases are tested on a prototype with three-linked rigid body system with an active joint and a passive joint. The investigation is made on the flexibility effect of tail on the propulsion performance. It shows there are optimized stiffness and damper coefficients at the passive joint leading the most efficient propulsion and fastest velocity through varying the posture of undulatory trajectory.

Chapter 1 Introduction

1.1 Introduction to Bio-Inspired Locomotion System

The so-called bio-inspired engineering/design is a new scientific discipline and has drawn a lot of attentions in the last few decades. It is a subject of learning the advanced principles from animals and then applying on the improvement of industrial devices. The principles come from wide range of species in nature, from the nano-scaled and micro-scaled living cells, tissues to the macro-scaled reptiles, bird, fish and mammal, and their applications cover many industry fields, e.g. biomedical devices, robot design, aerospace, naval architecture, etc.

The bio-inspired locomotion system is a sub-category of bio-inspired system, and it is about learning biological concepts from nature and applying them into the design of man-made propulsion devices. After billion years of evolution and natural selection, the flying and swimming animals in nature have developed their extraordinary locomotion abilities. They have high locomotion efficiency, low noise production, fast maneuvering and are normally environment friendly. All of these abilities can be utilized for designing vehicles with better propulsion performance and less damage to the environment. In this thesis, we concern only normal scale aquatic animals, and the hydro-wing models as well as multi-body models are designed and tested accordingly for exploring their propulsion performances.

Studies of bio-inspired locomotion system can be divided into two stages. In the first stage, the biological shapes and locomotion are directly copied into man-made vehicles, called bio-mimicry stage. Most of the robotic fishes and birds are the examples in this stage. The second stage, which is more advanced, is to learn from the nature, understand the mechanism and apply to improve the existed devices, such as the muscle-like bio-actuators, etc. In this thesis, most of the effort is devoted to focus on the simplified bio-mimicry system and investigate the fundamental mechanisms, while in the last past of this thesis, we present our preliminary study which can be

classified in the second stage. In the following, we combine these two stages together and review the most relevant work.

In this section, the classification of ways of fish swimming is firstly reviewed. The classic studies mimicking both undulatory body motion and tail flapping motion with models of simplified geometry are examined. The hydrodynamic performance of the bio-inspired locomotion systems is indicated on mainly two aspects, high quality of propulsion performance and outstanding energy harvesting ability. The concept of biomimetic applications has been developed for a few decades, and the robotic devices are also briefly introduced.
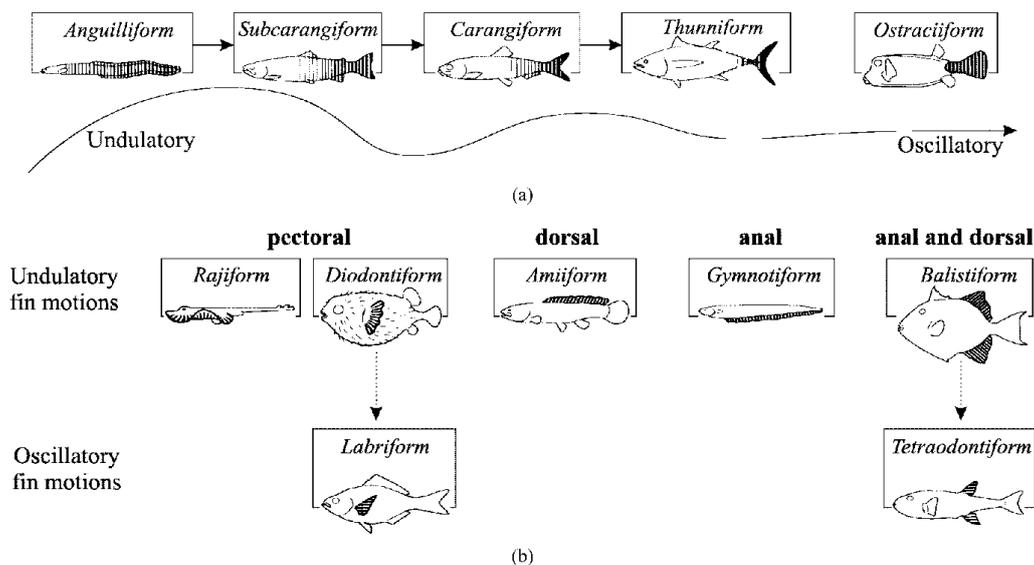
Figure 1.1 Classification of fish cruise. Courtesy of Sfakiotakis et al. (1999).

1.1.1   Classification of Bio-inspired Locomotion System

The bio-inspired locomotion system can be classified in different ways, and one of the typical classifications is to sort them by the flexibility of the fish body. As shown in Figure 1.1, fish under undulatory locomotion propel themselves by waving the entire

body, whereas those under oscillatory locomotion generate propulsion by flapping their caudal fins. The relevant simplified physical models are developed for scientific studies. For example, following the undulatory mode, the slender body theory is developed with the assumption that the entire body undergoes a traveling wave, and considering the different ways of oscillatory motion on the fish fin, there are investigations on the models of fish fins with the rest parts of body relatively rigid and stationary. In the present study, the flapping foil and flapping wing models are developed to represent the oscillation fins, and the undulatory motion is mimicked by a multi-body system that is inspired from the concept of muscle-like bio-actuators. The studies are reviewed based on two physical models, i.e. undulatory motion and flapping motion.
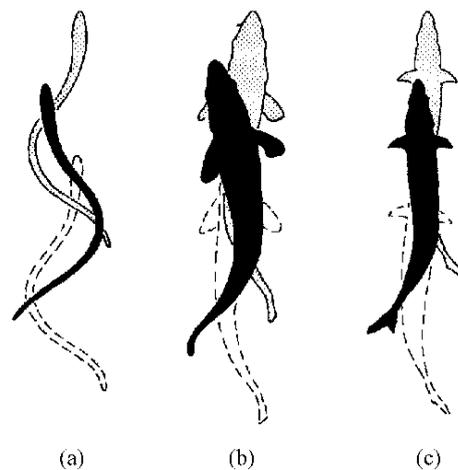
Figure 1.2 Fish swimming in a traveling wave form, (a) *Anguilliform* mode, (b) *Subcarangiform* mode, (c) *Carangiform* mode. Courtesy of Sfakiotakis et al. (1999).

1.1.1.1   Undulation Motion

As shown in Figure 1.2, concerning the body motion of *Anguilliform*, *Subcarangiform* and *Carangiform* modes, the whole body or most of the body participate in large amplitude undulation, which can be simplified as a traveling wave plate. Since the wave is transported backward, the undulation body pushes the surrounding water to

downstream. According to acting and reacting law, the surrounding water also exerts a thrust force on the undulation body. The differences among these modes are the wavelength and the amplitude being different for different modes.

In addition, the traveling wave model is also confirmed to be beneficial for the drag reduction. Taneda and Tomonari (1974) used the hot-wire anemometers to measure the flow field around a wavy wall. They concluded that the wavy plate accelerates its surrounding fluid, and meanwhile supressed the turbulent fluctuation. Recently, with the direct numerical simulation tools, Shen et al. (2003) captured the flow separation above the wavy wall. They further demonstrated that the separation disappeared once the phase velocity was larger than the flow velocity.
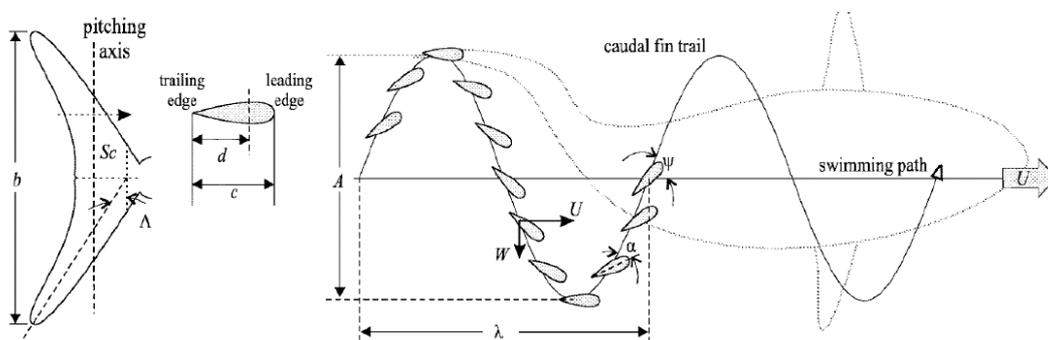
Figure 1.3 Schematic of flapping motion of a caudal fin. Courtesy of Sfakiotakis et al. (1999).

1.1.1.2 Flapping Motion

On the other hand, concerning *Carangiform* and *Thunniform* modes in Figure 1.1, fishes gain the thrust by oscillating their caudal fins, whereas their main body can be considered as a rigid body. Most of the large marine mammals, such as whale and shark, swim in this way, and their caudal fin is in crescent shape. As shown in Figure 1.3, the locomotion of the caudal fin can be decomposed into two parts, i.e. the translational motion along vertical axis and the rotational motion with respect to its peduncle. This kind of motion is normally called *flapping*. Meanwhile, the cross

section of the caudal fin can be simplified as foil geometry. Therefore, from a hydrodynamic point of view, scientist would like to employ the flapping wing or foil model to study the propulsion performance of fish swimming with *Carangiform* or *Thunniform* modes.

It is worthy of mention that the flapping wing/foil model is not only employed by fish swimming, but also applied in the study of bird and insect flying. As shown in Figure 1.4, if we has a close inspection to the wings of a dragonfly, the locomotion can also be decomposed into two parts, i.e. the translational motion and rotational motion, where the flapping wing/foil is also applicable.
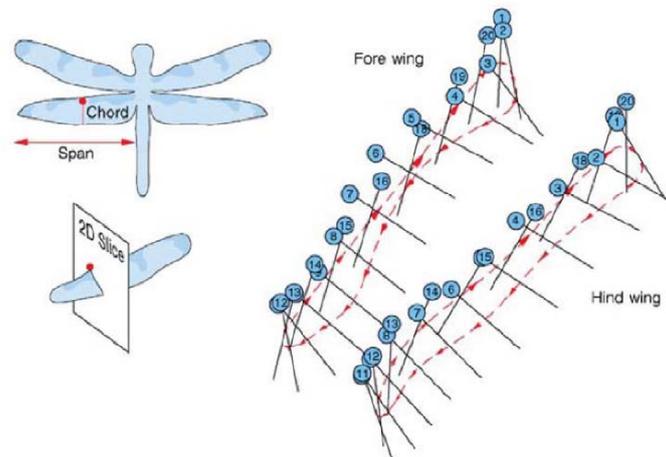
Figure 1.4 Trajectory of a flapping wing of a dragonfly. Courtesy of Wang (2005).

1.1.2 Hydrodynamic Performance of Bio-Inspired Locomotion System

As mentioned in the last section, there are mainly two typical models, i.e. undulating body and flapping foil, which are used in this thesis to study the bio-inspired locomotion. In the last three decades, theoretical, experimental studies as well as numerical simulation have been focused on these subjects. In the following sub-sections, relevant research work will be introduced within two categories, i.e. propulsion bases system and energy harvesting based system. In details, concerning propulsion based locomotion, the body is propelled with a prescribed undulation or

flapping motion. Within a specific range of kinematic parameters, the body can gain a thrust from its surrounding fluid, and move forward. For the energy harvesting based system, the body motion is either prescribed or induced by the incoming flow, connecting with an energy harvesting device or material.

1.1.2.1 Propulsion Based System

In the past few decades, large amount of efforts have been paid into the explorations on aquatic animal propulsion mechanism. The aforementioned two physical models are applied, either in theoretical investigations, or numerical and experimental studies. In this section, we review the available works based on the propulsion mechanism thoroughly.

In 1960s, Sir M. J. Lighthill first developed the slender plate theory (Lighthill, 1960, 1971) to study the hydrodynamic performance of a wavy plate model. In his studies, the motion of undulation body can be described as a traveling wave with increased amplitude from head to tail along the fish body central line. His theory proved that once the traveling wave speed is larger than the flow speed, the wavy body could gain thrust and move forward. After then, T. Y. Wu in California Institute of Technology employed the wavy plate model (Wu, 1961, 1971a, b, c), and systematically investigated the effects of wave frequency and wave number. Recently, with the development of computational fluid dynamics (CFD), large amount of numerical simulation work focus on this topic. Carling et al. (1998) numerically studied a released fish under free motion with self-propelled velocity calculated from the Newton's Second Law to calculate the fish self-propelled velocity. Dong and Lu (2005) studied the effects of phase velocity and wave amplitude on the propulsion performance of the wavy plate, and they found that a large wave amplitude corresponds to a high propulsion efficiency. Deng et al. (2006) conducted a two-dimensional simulation taking the thickness of the wavy plate into account. Leroyer and Visonneau (2005) employed the RANS turbulent model to study fish swimming performance at high Reynolds number. On the other hand, there are also certain studies concerning the group fish swimming. In 1970s, Professor Weihs (1973) first gave a comprehensive analysis of the hydrodynamics of fish schooling. As shown in Figure 1.5, schooling fish normally assemble in a diamond shape formation. Fish B

in Figure 1.5 is in the midline of the wake of Fish A and Fish C, and the shed vortices from Fish A and Fish C can help with the Fish B for better propulsion.
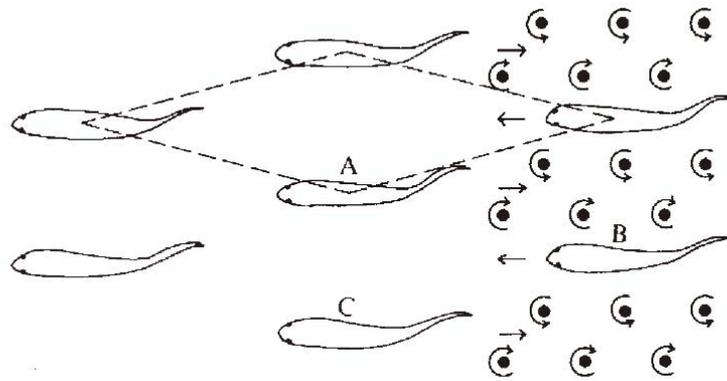
Figure 1.5 Schematic of fish schooling. Courtesy of Weihs (1973).

From 1980s, scientists started to apply the flapping foil/wing model to study biological locomotion of fish tail. The pioneer work is done by Freymuth (1988) that the reverse Kármán vortex street in the wake of a plunging and pitching wing in a wind tunnel was experimentally captured with a narrow strip of liquid titanium tetrachloride deposited from the leading to the trailing edge. From 1990s, the research group of Professor Triantafyllou at Massachusetts Institute of Technology (MIT) conducted several experimental work on the flapping wing. They indicated that a flapping wing obtaining either a thrust force or a drag force depends on the appearance of reverse Kármán vortex street, and was also corresponding to the non-dimensional flapping frequency, i.e. the Strouhal (St) number (Triantafyllou et al., 1991). They reported that when the St number is in the range of 0.25-0.35, the flapping wing obtains thrust and the vortex wake appears as a reverse Kármán vortex street (Triantafyllou et al., 1993). They then systematically studied the propulsion performance of the flapping wing, which includes high efficiency flapping motion mode (Anderson et al., 1998), effects of flapping parameters (Read et al., 2003), attack angle profile (Hover et al., 2004) and asymmetric flapping (Schouveiler et al., 2005).

Concerning the numerical investigation, Wang (2000) first simulated a two-dimensional oscillating foil. Lewin and Haj-Hariri (2003) used the same model and investigated the leading edge vortex structures under different St number and the correlation of St number to propulsion efficiency. Guglielmini and Blondeaux (2004) extended the previous model to a fully flapping foil model with coupled heaving and pitching motions, it showed in their results that the coupled pitching motion can enhance the thrust and propulsion efficiency. Later on, a parametrical simulation was conducted by Pedro et al. (2003), using the Arbitrary Lagrangian-Eulerian method (ALE). Direct numerical simulations of a three dimensional flapping wing were also reported recently. Blondeaux et al. (2005) used a moving reference frame to handle the flapping wing motion, cases with two typical St number were investigated. At relatively lower St number of 0.175, the interactions between vortex rings are weak, whereas at St number of 0.35, the interactions are enhanced and the vortex rings begin to connect with each other. Dong et al. (2006) used immersed boundary/ghost cell method to simulate an elliptical wing, three aspect ratios were investigated. Shao et al. (2010) systematically investigated the effect of aspect ratio on the propulsion performance and vortex structures in the wake.

1.1.2.2 *Energy Harvesting Based System*

In the last two decades, scientists start to focus on the design of energy harvesting devices. Apart from the traditional turbine-like facilities, there are a lot of devices developed from the inspiration of fish motion. Although the traditional devices can be highly efficient, they have certain disadvantages, e.g. it has fast rotating blades which are threats to aquatic animals and it requires high qualities of operation conditions, such as stably high speed flow and deep depth water, etc. Recently, people start to employ the flapping wing model on flow energy harvesting devices, and it is believed that it can be smarter with flexible motion and more efficient in wider sea regions than the traditional devices. In particular, it is easy to be manufactured and it is feasible to be planted in shallow water in groups. Two prototype designs are given in Figure 1.6.

(a)

(b)
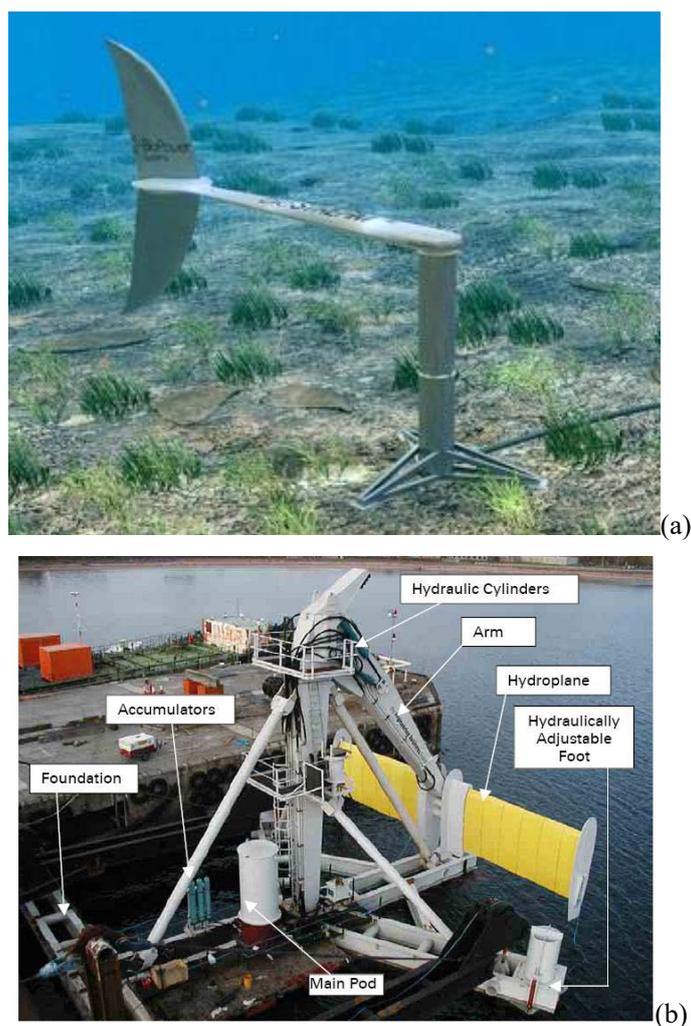
Figure 1.6 (a) Tuna-inspired tidal power system (Stingray tidal stream energy device); (b) Oscillating marine current energy convertor by Pulse Tidal.

McKinney and DeLaurier (1981) first proposed a wingmill device which can extract flow energy through the flapping motion of an aerofoil. According to the degrees of freedom of the system, people normally categorized the flapping based energy harvesting system into three types, i.e. fully-active system, semi-active system and purely passive system (Xiao and Zhu, 2014), the schematics are shown in Figure 1.7. Most of the studies focus on the fully active model. Kinsey and Dumas (2008) investigated the energy harvesting efficiency of a single oscillating aerofoil, which reaches as high as 35%, and it is also confirmed by their experiment (Kinsey et al., 2011). Cho and Zhu (2014) further studied the hydrodynamic performance of a flapping foil energy harvesting system in shear flow, to mimic the real flow condition of energy harvesting device. For three-dimensional simulation, Deng et al. (2014)

proved that the flapping wing with aspect ratio of AR=4 was the most appropriate choice for energy harvesting system under a sinusoidal pitching motion. Xiao et al. (2012a) applied a trapezoidal-like profile of the pitching motion and they found an optimal profile which can dramatically enhance the power output and energy harvesting efficiency.
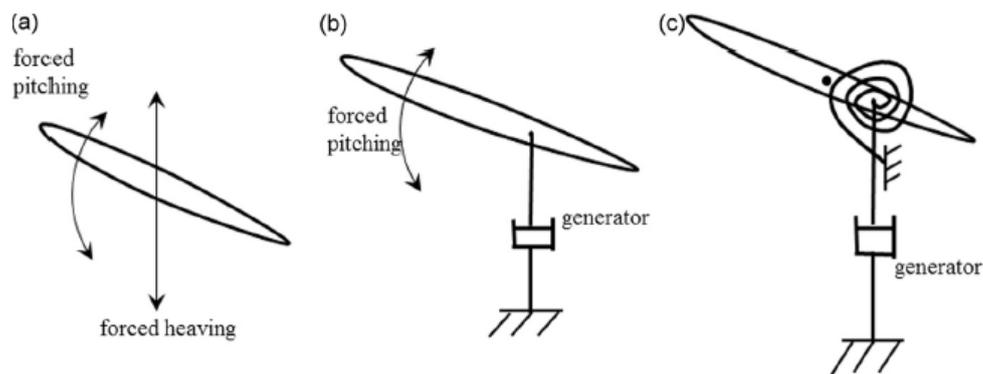
Figure 1.7 Classification of flapping foil energy harvesting system, (a) fully active system, (b) semi-active system and (c) purely passive system. Courtesy of Xiao and Zhu (2014).

In the aspect of control simplicity, the semi-active system or purely passive system is more feasible than the fully active system that requires complicated mechanical system for the coupled rotational and translational motion. Zhu and Peng (2009) first employed the semi-active system, they suggested that the hydrodynamic efficiency of the semi-active system depends on several parameters which include pitching frequency, pitching amplitude, location of pitching axis and the damping constant. Recently, Deng et al. (2015) investigated the inertial effect on the performance of the semi-active system, in their study, the mass ratio varies from 0.125 to 100. Peng and Zhu (2009) also developed a purely passive model, in which the flapping foil is mounted with a damper and a rotational spring. In their numerical simulation, four different responses were captured. They shows that stable energy can be harvested once the periodic pitching and heaving motions are reasonably excited. Furthermore, Zhu (2012) also studied the performance of purely passive system in shear flow.

(a)

(b)

Figure 1.8 (a) Robotuna (Charlie I) and (b) Robotuna II at MIT.

1.1.3   Applications of Bio-Inspired Locomotion System

At the same time of carrying on scientific investigations, various robots are designed with bio-inspired locomotion systems. It is expected that the newly designed locomotion systems can have better performance than the conventional transportation systems. For example, they may cost less energy, make lower noise and be more environmental friendly, despite the fact that it is difficult to fully mimic the locomotion of real animals by the man-made bio-inspired system. At present, most of

the bio-inspired systems are aiming to imitate the kinetic motion of real animal actively. In the future, scientists may move forward to locomotion mechanism from the aspects of both mechanical and biological, such as taking the muscle and other internal body actions into account. Here in this section, we would like to briefly introduce a few typical man-made bio-inspired systems.

The research group of Professor Triantafyllou at MIT is one of the pioneer groups in robotic fish design. In the period from 1993 to 1995, the first generation robotic fishes, RoboTuna (Charlie I) and RoboTuna II, were designed and fabricated in the laboratory (Figure 1.8). Their design focused on the oscillation of caudal fins, and the hydrodynamic mechanism is investigated by the induced local flow structures. There are six servomotors and each of them provides two horsepower.

After then, the MIT research group began to design the second generation of robotic fish, RoboPike, upon the model Pike which is a good example for fast start and manoeuvring. In 2000s, a new generation of robotic fish was born by mimicking a turtle, i.e. RoboTurtle (Licht et al., 2004) in the same laboratory. The RoboTurtle has four fins as shown in Figure 1.9, each of which leads a combined pitching and rolling motion. This kind of locomotion facility provides a possibility that the whole robot can turn around with 180 degrees within a very small radius area. Besides the research group at MIT, there are several groups focusing on the design of robotic fish, such as Japan Maritime Research Institute where the PE-600 and UPF-2001 robotic fish is born, and Beijing University of Aeronautics and Astronautics where the fast swimming robofish is designed and tested.

Recently, the concept of soft robot comes out, and the designs based on this concept become popular. Although the development of rigid robots turns mature, the rigid structure may cause non-negligible performance losses due to limited adaptability in the hardware that cannot be easily compensated by the software, and also partially because of the lack of flexibility in conventional actuation mechanisms. In contrast, a

soft robot structure be deformed to keep balance in uneven ground and be suitable for operating in harsh environments. With smaller stiffness, soft bodies can deform to be more flexible and absorb energy more efficiently than rigid bodies. This makes it extremely attractive in the case of a crash, as well as conformable to unknown objects and conditions. These inherent advantages bring soft robots closer to biological capabilities observed in nature. To this end, in the past few years, various new types of soft robot and AUVs are developed.

(a)

(b)
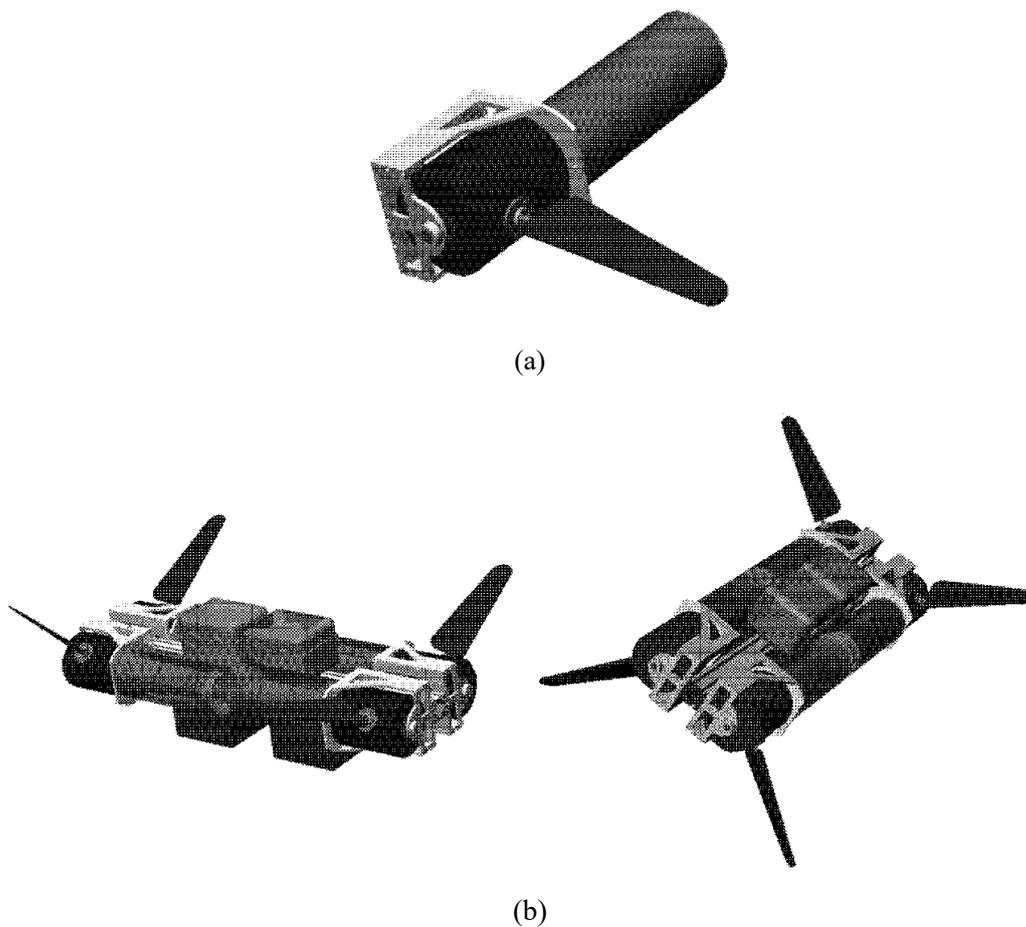
Figure 1.9 (a) Actuator element and (b) general view of RoboTurtle at MIT.

U.S. Naval Undersea Warfare Centre and Office of Naval Research recently funded a multi-university, national-wide $5 million project. The ultimate goal is to install a self-powered, autonomous machine in water for the purposes of surveillance and environment monitoring. Two robotic jellyfish of different sizes, as shown in Figure 1.10, are built by a project team at Virginia Tech, USA. At current stage, the work is focused on reducing power consumption and improving swimming performance so as to better mimic the real morphology of natural jellyfish.

Figure 1.10 Robotic jellyfish of Virginia Tech. USA.
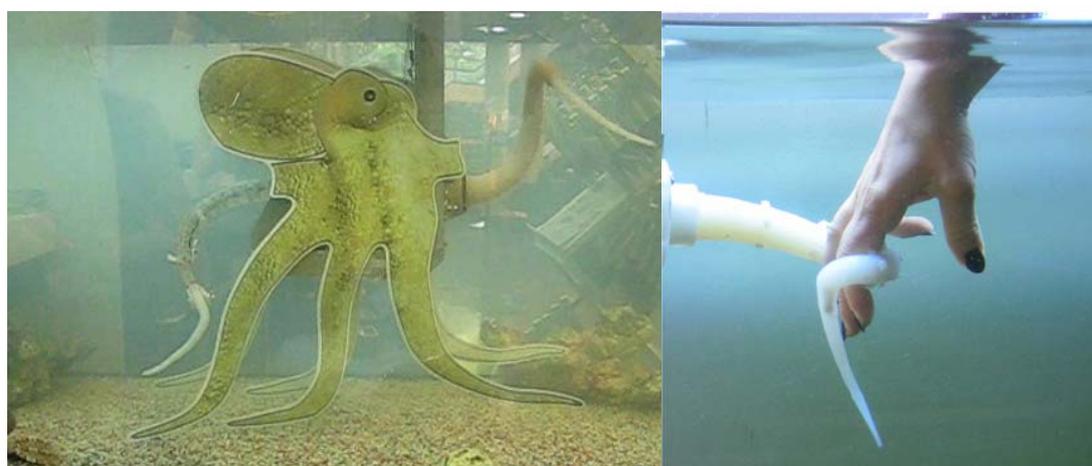
Figure 1.11 Robotic octopus in EP7 project.

Meanwhile, in Europe, OCTOPUS project funded by the European Commission under the 7th Framework Program (FP7), aims at investigating and understanding the key principles of the octopus body and brain. The models are shown in Figure 1.11. It is expected to build a soft 8-arm octopus robot, which is able to move in water, with its arms to elongate and grasp flexibly.

More recently, the first autonomous entirely soft robot was invented by a team at Harvard University, called 'Octobot' to mimic the octopus, which is 3D-printed (Wehner et al., 2016).
(http://news.harvard.edu/gazette/story/2016/08/the-first-autonomous-entirely-soft-robot/) This new conceptual robot is pneumatic-based (Figure 1.12), and it is powered by gas under pressure. A reaction inside the bot transforms a small amount of liquid fuel into a large amount of gas, which flows into the octobot's arms and inflates them like balloons.
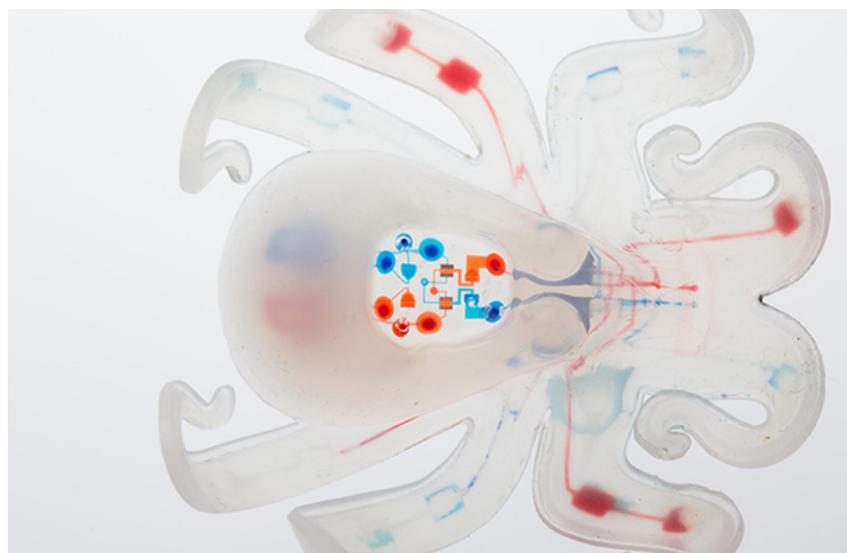
Figure 1.12 First autonomous entirely soft robot invented at Harvard University, called 'Octobot'.

The fish-like soft robot is also invented with the help of development of flexible linked joint under control of actuators and motors. Professor Hu at University of Essex made a stunning fish robot for pollution detection. As shown in Figure 1.13, the robot is fully fish like and swims with undulatory motion. There is a rigid head, inside which the computers, sensors and battery locates, and flexible links concavely

connect together for the body and the tail section, so this can be driven by the electric power to bend the body like a real fish. The other outstanding project is funded by the Envirobot project, lead by the Biorobotics Laboratory in Ecole Polytechnique Federale de Lausanne (EPFL). An amphibious robot is built for outdoor robotics tasks, taking inspiration from snakes and elongate fishes as shown in Figure 1.14. Various types of adaptive controllers based on the concept of central pattern generators are tested for achieving the most proper locomotion controlling nerual network.
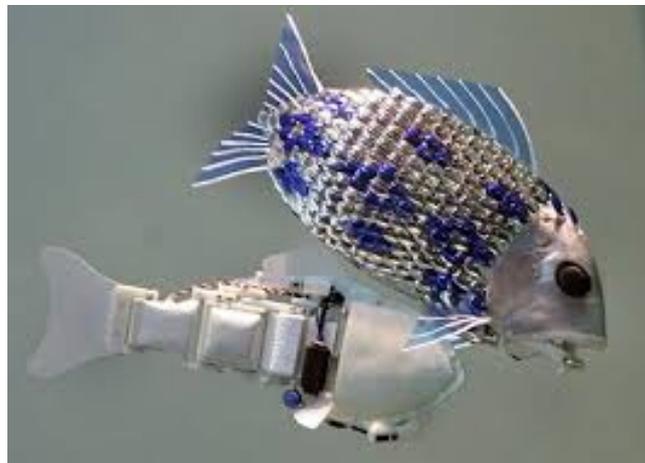
Figure 1.13 Robotic fish designed in University of Essex.

Figure 1.14 An amphibious snake robot, AmphiBot.

1.2 Physical Problems and Study Scope

According to the review of bio-inspired locomotion in previous section, a few models are proposed for further study. With a special emphasis on the hydrodynamic mechanism, the work in this thesis is mainly about two simplified physical models: three-dimensional flapping wing model with flexibilities in lateral and rotational directions, and multi-body system model with rigid components connected by revolute joints. Both of the flapping motion and undulatory motion are the typical bio-inspired locomotion. The former model is inspired from the fish caudle fin's flapping motion as reviewed in the Section 1.1.1.2, and the latter one is applied to mimic the undulatory motion of entire fish body referring back to the Section 1.1.1.1, and the special treatments on the joints can enable the body undulates both passively and actively. The physical problems and study scope is briefly introduced in this section.
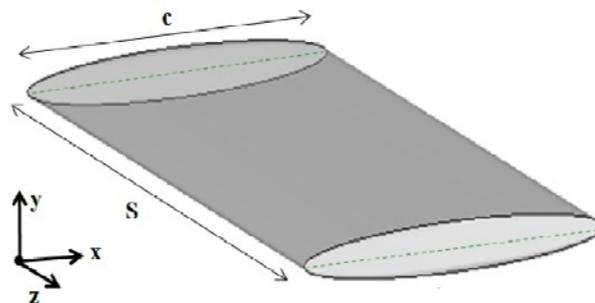
Figure 1.15 Sketch of the simulation model.

The schematic view in Figure 1.15 shows that the flapping wing model is with three-dimensional (3D) geometry of rectangular shape with elliptical cross-section. The wing is allowed to move actively in plunging (y) direction, and it has freedoms in in-line (x) and torsional (around z-axis) directions. The wing starts the plunging motion in a fully quiescent water condition with flow velocity as zero in the entire domain, and the induced motion in lateral and torsional directions are solely determined by the fluid-motion coupling between fluid and wing. A parametric study

is carried out throughout the Chapter 3 and Chapter 4 to explore the hydrodynamic performance of such a model under various combinations of both geometric and kinetic parameters.

The second physical model is a multi-body system, as shown in Figure 1.16, that the undulatory fish body is treated as a series of linked rigid bodies connected by hinges. The undulatory motion can be mimicked by mechanical systems with rigid segments and hinges. Hinge between two adjacent bodies can be modelled as revolute joint, with either passively induced pitch motion or actively prescribed pitch motion. The more distributed segments can achieve more accurate motion. The entire system can move freely in water under the specific propulsive pattern. Special emphasis is put on the development for solving the problems of coupling multi-body dynamics with fluid dynamics by implementing Mobile Multi-body System (MMS) algorithm with CFD solver. Verifications are carried out by repeating the previous work, and innovative cases are tested on a prototype with both active joints and passive joints.

Three arbitrary adjacent bodies
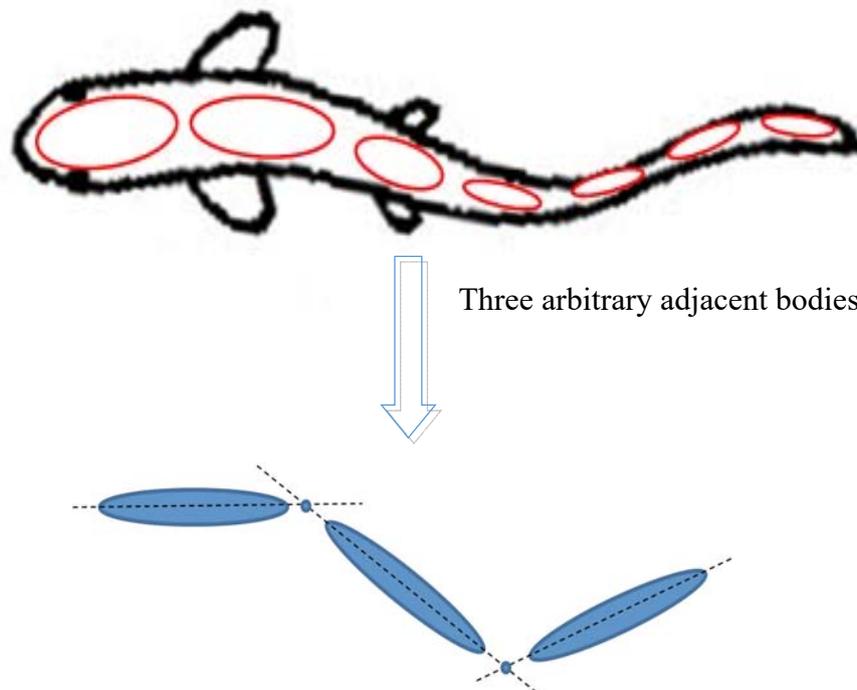
Figure 1.16 A conceptual schematic of multi-body system as substitution of fish body.

1.3 Critical Review

Concerning the two basic physical models, i.e. the 3D flapping/plunging wing model and the multi-body systems, for investigation in this thesis, relevant research work of experiments and numerical simulations in the past a few decades are thoroughly reviewed in this section.

1.3.1 Flapping Wings

The term "*flapping*" is always mentioned and employed in the study of wing motion of various animal species. As aforementioned, in recent decades attentions have been focused on the propulsion mechanism under a coupled interaction between animal locomotion and its surrounding viscous fluid. In this content, the propulsion motion of animal is purely determined by the fluid force and moment generated by its forced locomotion (Alben and Shelley, 2005; Hu et al., 2011; Lu and Liao, 2006; Spagnolie et al., 2010; Vandenberghe et al., 2006; Vandenberghe et al., 2004). In the classic studies, it is simplified to a combined pitching and heaving motion, and propulsion performance can be observed by examining the lateral fluid forces under a prescribed heaving or pitching motion numerically and experimentally (Dong et al., 2006; Heathcote and Gursul, 2007; Lewin and Haj-Hariri, 2003; Triantafyllou et al., 1991; Young and S. Lai, 2004). Investigations are carried out by the wings with simple geometries, covering various system kinematic and structural parameters, such as sectional foil shape, plunging frequency, amplitude, and density ratio. Results from these studies showed that the forced plunging or flapping motion leads foil acquiring a thrust force or moving, in the direction perpendicular to the prescribed motion.

More recently, the study on the flapping wing problem is developed one step further by taking into account of the wing system flexibility (Kang and Shyy, 2013; Mountcastle and Combes, 2013; Spagnolie et al., 2010; Zhang et al., 2010). It is well known that a key feature in flapping wing flight or natural flyers' wings is the

deformable structure that endures either a passively or actively variable shape, owing to their inertial and aerodynamic forces during flight. The aerodynamics and structural dynamics of such flapping wings are strongly coupled, which often leads to a complex fluid-structure interaction (FSI) problem. Therefore, it is of great importance to answer a central question of how the three-dimensional and passive change of wing kinematics due to inherent wing flexibility contributes to the unsteady aerodynamics and energetics during a flexible flapping wing flight (Nakata and Liu, 2012).

To study the flapping wing system flexible impact on its propulsion performance, one common method utilized is to introduce a torsional spring at its flapping pivot point (Spagnolie et al., 2010; Zhang et al., 2010). Previous studies by Combes and Daniel (2003a) and Combes and Daniel (2003b) on the flexure stiffness variation of a hawkmoth and dragonfly observed that the flexibility decays sharply from the wing leading edge to the trailing edge and from the root to the tip. With the observation of high flexibility around the wing root, a simplified structure dynamic model to mimic the flexible role of large wings and appendage in the biologic flapping motion is to use a lumped-sum torsional flexibility model. In a context of free flying, the wing is free to move in the lateral direction, and is also able to pitch clockwise and anti-clockwise. The rotational motion is modelled by elastic torsion spring acting on the pivot point (Ishihara et al., 2009; Nakata and Liu, 2012; Vanella et al., 2009). By introducing these two Degree of Freedoms (2DoF) in both the lateral and pitching directions, the biomimetic model getting close to the nature flapping-based animal propulsive motions, where both the translation and pitching modes are passively induced.

A systematic numerical and experimental study on an elliptic wing with a forced heaving motion but passive pitching about its leading edge was performed by Spagnolie et al. (2010). While the simulation was conducted at a much lower flapping frequency relative to their experiment, many dynamic characteristics of wings are supported by their numerical results. The wing with lateral free movement under

propulsion of prescribed plunging motion is conducted experimentally/ numerically. Under the conditions of two density ratio ($\sigma = 10$ and 1.0) defined as the density of wing over the density of surrounding fluid, non-dimensional flapping amplitude of 0.5, dimensionless spring constant $k = 50000$ (torsional spring constant) and shape aspect ratio (AR) (thickness divided by chord length), by increasing flapping Reynolds number (Re_{fr}), four flow regimes are found: (i) no lateral movement with an almost left/right symmetric flow without a torsional motion; (ii) an improved lateral motion with adding a torsional spring than without it (an increased net force in lateral direction); (iii) a deteriorated lateral performance relative to its rigid counterpart; (iv) a bi-stable status, hysteretic regime in which the flapping wing can move horizontally in either directions. Compared to a 1DoF flapping wing in lateral free movement only, one significant finding is that a wing with 2DoF including free-pitching could activate its lateral motion at a lower flapping frequency, clearly indicating that the system flexibility, represented by a pivot point torsional spring, is beneficial to the lateral thrust generation. In addition, the maximum lateral velocity is observed when the wing flaps at a frequency around system resonance frequency. The examination of the wing shape AR varying from 0.1 to 1.0 also revealed a transition from coherent to chaotic motion and then a return to coherent motion when AR = 1.0, where the wing becomes a circular cylinder.

The study addressing the role of the foil's torsional stiffness of pitching flexibility has also been pursued by Zhang et al. (2010) recently. Using a multi-block Lattice Boltzmann Method (LBM), a so-called flexible plate is modelled by a rigid plate with a torsional spring acting on the pivot point at the leading edge of the plate. They found that the dynamics response of the plate presented a non-periodic status, a periodic forward status and periodic backward status by varying various foil kinematic and structure parameters. The exact boundaries between the above three regimes relied on the flapping amplitude as well as the wing linear density ratio as well as the ratio between the system natural frequency to the forced flapping frequency.

21

Two-dimensional (2D) assumption is usually reasonably valid for the wings with large aspect ratios, which significantly reduces the computational challenge and time. However, in contrast to flying animals, fish tend to have relatively lower aspect ratio wings, such as the aspect ratios of four species of labrid fishes ranging from about 1.5 to 3.5 (Walker and Westneat, 2002), bluegill sunfish and rat fish having pectoral fins with aspect ratios of about 2.4 (Drucker and Lauder, 1999) and 2.2 (Combes and Daniel, 2001). Limited research on 3D tethered flapping wings shows that the wing with low aspect ratio generates high propulsion efficiency and reduced bending moment relative to the large aspect ratio wings, whereas thrust increase monotonically with aspect ratio (Dong et al., 2006; Visbal et al., 2013; Walker and Westneat, 2002). The wake vortex topology also presented a remarkable 3D effect, which is strongly linked to the wing kinematic performance. The wake of thrust-producing flapping foils with finite AR is dominated by two sets of interconnected vortex loops, whilst for the low AR wings, the loops evolve into distinct non-circular vortex rings downstream (Blondeaux et al., 2005; Dong et al., 2006).

Although the interesting physical phenomenon of the self-propelled flapping wing is well documented in the aforementioned two papers (Spagnolie et al., 2010; Zhang et al., 2010), no relevant research has been performed on the three-dimensional wing with relatively low AR, i.e. AR ≤ 4.0 (AR is defined as span/chord length). In this situation, 3D effect must be taken into account. The question of whether the flow phenomena observed from a 2D wing is applicable to a 3D wing under a self-propelled 2DoF condition is still open for investigation, and this thesis provides new findings in this particular area.

1.3.2   Multi-body System

In above, the reviewed work mostly focus on the single rigid flapping foil/wing model with two or three degrees of freedom. However, the single flapping wing can be only

considered to mimic part of the swimming fish (fish tail) or flying insect or bird (wings). Independent study of the part of the swimming fish or flying bird, e.g. fish tail or bird/insect wings, can help us to understand its mechanism of propulsion or lift, while the mutual interaction of the considered part and the other parts is ignored which may also plays an important role in the performance of swimming or flying (Akhtar and Mittal, 2005). Therefore, it is necessary to create a fully resolved model considering both the active parts (fish tail or bird/insect wings) and inactive parts (fish head or bird/insect body), and a comprehensive understanding of the hydrodynamic/aerodynamic performance of the whole fish/bird/insect may help us to better design the biomimetic robots.

Besides the single flapping wing model, the undulation body is also one of typical models of bio-inspired locomotion. In the past, as mentioned above, people employed the travelling wave plate to represent the undulation body. In detail, the whole fish (especially the *Anguilliform* type in Figure 1.1) is considered to be a wavy plate travelling from head to tail, with small oscillation amplitude at the head (inactive part) and large amplitude at the tail (active part). In this model, the motion and the shape (or the outside surface) are prescribed in every instantaneous. However, this model still has few limitations: First, it is only proposed to mimic eel-like fish, and not applicable for bird/insect mimicking; Second, from the viewpoints of biology and robotic fish/bird/insect design, the internal dynamics, i.e. muscle behaviour from biology side and actuators design from the side of robotic design, are also worthy to clarified, which may help us to assess the power consumption and efficiency in a board coverage of measurement.

Therefore, the motivation for the multi-body system study can be concentrated into two aspects: the benefits from using a flexible body and the convenience of developing numerical and experimental models. The first aspect mainly relates to the improved hydrodynamic performance caused by structural flexibility - such as passively induced or actively controlled relative motion between different parts of the

entire body. The second aspect is the development and assessment of numerical algorithms and the modelling of a multi-body system with rigid linked elements compared to a fully elastic, deformable model. Relevant research work is reviewed in the following paragraphs.

Firstly, people realized that the body flexibility might play an important role in fish swimming and bird/insect flying, whenever it is actively or passively bended. The attentions have been paid into the enhanced performance of drag reduction and propulsion efficiency increase. The force and power measurement results from an experiment work (Barrett et al., 1999) demonstrated that the power required by an actively undulatory fish-like body is much smaller than the power needed to tow the rigid ones at the same speed. It is also observed that some fish have elastic caudal tails, and the softness of such tails have influence on the efficiency (Bergmann et al., 2013). Meanwhile, Beal et al. (2006) put a 'dead' fish in the wake of a D-section cylinder. It was observed that the fish is propelled upstream when its flexible body resonates with incoming vortices. Different ways of treatment on the hinge control make the multi-body system performs as a flexible body, which may have wide applications in both experiment and numerical studies.

In the study of flexible body, concerning the physical basis, scientists have developed several different models to investigate the phenomenon induced by body flexibility. Argentina and Mahadevan (2005) employed the linearized flag model and derived the pressure loading based on thin aerofoil theory. They concluded that the instability occurs when the frequency of the lowest mode of elastic bending vibrations coincides with the frequency of aerodynamic oscillation of the hinged rigid plate. Alben and Shelley (2008) applied the inextensible flexible sheet model and solved the fully nonlinear dynamics numerically in an inviscid 2D flow with a free vortex sheet. The transition from stable periodic flapping to chaotic flapping with decreasing bending rigidity was reported, and both bi-stability and hysteresis were found with this nonlinear dynamical model. Using the similar model, Michelin and Smith (2009)

imposed a forced heave motion at the head of a flexibly deformable wing, and solved the dynamical equations Chebyshev spectral methods. The peaks in mean thrust were found to correspond to maximum values in the trailing-edge amplitude, which were the results of the resonance between the frequency of heaving motion and the natural frequencies of the system. Furthermore, considering the fluid viscous effect, Connell and Yue (2007) developed a fluid-structure direct simulation solver coupling a numerical simulation of the Navier–Stokes equations with the aforementioned full nonlinear model. In addition, the neo-Hookean solid model was also used (van Loon et al., 2006; Yu, 2005).

In the field of multi-body system representing flexible body, Farnell et al. (2004b) assumed a filament which was composed of several elements, and each element was fixed to one another at the hinge with a spring. It was shown in their work that the filament oscillation can be suppressed with short length. Meanwhile, the coupled states of two flapping filaments were also studied by the same group (Farnell et al., 2004a). Later on, a series of work is done by Eldredge's group (Eldredge, 2008; Eldredge et al., 2010; Toomey and Eldredge, 2008; Wang and Eldredge, 2015) and Kajtar and Monaghan (2010) on an articulated multi-segment system for exploring the self-propulsion behaviour. Both passive and active control on the hinges is feasible in these studies with an algorithm based on an elimination work of a set of variables. The global self-induced motion was investigated when the fish swims with the imposed undulatory posture in flow field with various fluid viscosities. The results also illustrated the flexibility impact on the force production with a model consisting two rigid bodies connected by linear elastic spring under prescribed motion, that the lift force and wing deflection were both found to be primarily controlled by the nature of wing rotation, and rotation phase lead shifted the instant of peak deflection and notably increased the mean lift. These successful works indicated that the treatment on the fish body as multi-segment system is a smart way of exploring the flexibility behaviours numerically as the algorithm is simplified when mimicking the body deformation through solving relative motions between each pairs of adjacent rigid

bodies instead of solving the complex finite element equation.

Secondly, from a biological point of view, along with the external hydrodynamic behaviours, there are also investigations on the internal dynamics by looking into the interactions between internal forces, body stiffness and muscle activations etc. Taking fish for an example, the muscle functions may vary significantly in species, but most of power is generated by bending body, extending and contracting muscles, and transmitted from front towards the tail. The multi-body system can be considered as a simple model, in which the hinge properties are used to mimic muscle functions. Meanwhile, concerning the design of robotic fish or insect/bird, the structures of the main body are mostly designed as multi-body systems for the convenience of control (Ostrowski and Burdick, 1998; Porez et al., 2014c).

In the study of muscle functions, the posterior muscle plays a role together with passive structures on power transmission (Altringham and Ellerby, 1999). Taking body stiffness, muscle activation, and fluid environment into account, a computational model of a lamprey was developed by Tytell et al. (2010), and the authors showed that there is optimal body stiffness for maximum acceleration and maximum velocity respectively. Though the agreement is achieved that the fish could benefit from the elastic body structure, there are still difficulties to quantify the effect of flexural stiffness on the complex internal and external coupled behaviours. Therefore a simplified model for prototyping the fish motion is needed to improve the fundamental understanding of how the fish react with different body stiffness.

In the design of robotic fishes, to the knowledge of the author, the best way could be using Mobile Multi-body System (MMS) structure. The dynamic behaviour of interconnected rigid or flexible bodies is also an important subject. The multi-body dynamics algorithms aim to solve the relative motions between each pair of adjacent hinge linked components and predict the global movement driven by internal and external forces, torques and constrains. Distinguished by the ways of motion actuation,

there are fundamentally two types of hinges – passive and active hinges. The algorithm for the latter is to calculate the relative hinge motion from available internal forces/torques, known as forward dynamics; and the latter is to reconstruct the internal forces/torques from the prescribed movements and external forces, known as inverse dynamics (Otten, 2003). Recently, Porez et al. (2014c) in Professor Boyer's group has sucessfully developed a "hybrid algorithm" based on a Newton-Euler based algorithm with forward manipulator dynamics (Featherstone, 1983) to resolve the problem with both forward and inverse dynamics. Comparing with Eldredge's method (Eldredge, 2008), the algorithm developed by Boyer's group (Khalil et al., 2007; Porez et al., 2014b; Porez et al., 2014c) is more efficient and compatible for various types of joints.

1.4 Objectives of Present Study

Based on the background and motivation of current research, the main objective of this research work is to develop a fully resolved computational model of bio-mimetic locomotion system, investigate the hydrodynamic performance of simplified bio-inspired models, and aim to understand the fundamental fluid mechanism utilized by flapping and undulatory motion for thrust/lift generation and propulsion. In order to perform this task, minor objectives are targeted:

- Implementing computational techniques on simulations that require moving boundary condition, and developing coupled method between CFD solver and kinetic equations for solving self-propelled motion of fluid-structure interaction models.

- Examining hydrodynamic performance of flapping motion with the simplified model of three-dimensional rigid wing, and clarifying the effects of different geometric and kinematic parameters on propulsion production, especially in

the conditions of low aspect ratio with one or two degrees of freedom released.

- Developing a method to solve the coupling problems with multi-body dynamics and fluid dynamics through implementing Mobile Multi-body System (MMS) algorithm with CFD solver, which is capable of simplifying the numerical simulations on the models with undulatory motion.

1.5 Outline of Thesis

The remainder of this thesis is presented in five chapters.

The computational framework is introduced in Chapter 2. Details are given of the general ways of implementing the discretization and numerical schemes to solve the governing equations. Typical numerical test cases are performed as pre-validation results of the method.

In the third part, a model of 3D flapping wing is generated with one degree of freedom in translational direction. The phenomenon of the up-down plunging motion of inducing an inline motion of the wing with left-right symmetric geometry is documented. The propulsion mechanisms along with the other relevant hydrodynamic performance are well indicated by the fully resolved CFD solution results.

This model is extended to include one more degree of freedom in the rotational direction in Chapter 4. A parametric study is carried out for exploring the effect of the rotational stiffness on the inline motion propulsion. The results are systematically analysed through various combinations of both geometric and kinetic parameters.

Following with the fourth part, a separate study is carried out with the multi-body systems for validating the coupled method between CFD solver and Mobile

Multi-body System algorithm and also investigating the effect of the passive joint on the propulsion.

Finally conclusion and summary are drawn in Chapter 6, and suggestions are made for future work.

Chapter 2 Mathematical Method

2.1 Introduction

To study the Fluid-Structure Interaction (FSI) problems, a major work is to solve the fluid motion and momentum around the immersed structure, which falls into the subject of fluid mechanics. The basic properties of fluid include density, viscosity, pressure and turbulent intensity etc. Approaches of studies on fluid mechanics can be classified into three category, theoretical study, experimental study and numerical study.

In the manner of theoretical study, by the conservation laws of mass, momentum and energy, the simplified governing equations of fluid motion and energy can be created, and the velocity field, pressure field, density distribution and temperature distribution of the fluid can be analytically solved. However, when the governing equations turn to be non-linear which is usually in the case, it is difficult to obtain the exact solutions of the governing equations. In the past, for simplification, certain additional assumptions were made. For example, in the field of hydrodynamics, the fluid was usually considered as inviscid, and hence, the potential function of the fluid motion can be derived (Lamb, 1930). On the other hand, concerning low Reynolds number (Re) flow, the non-linear part was normally neglected, and the fully governing equations turn to be Stokes equations (Kim and Karrila, 1991), which were widely used for the models with low speed or low Re number.

In the manner of experimental study, the fluid visualization is the major task. In early days, the smoke wire method and relevant techniques were employed to capture the flow pattern. The pressure sensors and three or six components balances are used to measure the pressure or fluid force acting on certain objects. Nowadays, new generation techniques are developed, such as Particle Image Velocimetry (PIV) and Laser Doppler Velocimetry (LDV), and helping to capture more detailed flow structures. However, the cost of experimental studies are usually high, and meanwhile,

it is difficult to handle several problems such as scale effects of model study, etc.

From the middle of twentieth century, computer techniques are developed very fast. Scientists began to solve the complicated Partial Differential Equations (PDEs) numerically. Normally, the governing equations are discretized into a set of algebra equations with acceptable truncation errors. The discretization method can be usually classified as Finite Difference Method (FDM), Finite Element Method (FEM) and Finite Volume Method (FVM) (Ferziger and Peric, 1996). The FDM follows the transformation of the Taylor series expansion of the terms in PDEs, and the physical grid is usually locally structured, and the coordinate axes coincide with the grid lines. Unlike FDM, FEM adopts unstructured grid and curved cells, which helps to handle complex geometries. The solution is assumed to be within a prescribed form, and it has to belong to a function space. On the other hand, FVM uses the integral form of the governing equation by inducing the divergence theorem, and volume integrals of certain terms can be converted to surface integrals. Meanwhile, FVM adopts unstructured grid, which benefits users for complex geometry simulation.

In this thesis, the FVM of the numerical method is applied for dealing with the complex structure geometries. In addition, in order to model the interaction between fluid and the moving structure, special treatment and technics are employed to handle the moving body or moving boundary. In the following sections, we will firstly introduce the governing equations for solving fluid motion, followed by an introduction of FVM. Numerical techniques for FSI are briefly presented along with the typical numerical tests.

2.2 Governing Equations

Water is the most common liquid medium, which is considered as a Newtonian, incompressible and viscous fluid. Based on the conservation of mass and momentum, the well-known Navier-Stokes equations are employed as the governing equations.

$$\nabla \cdot \mathbf{u} = 0,$$

$$\frac{\partial \mathbf{u}}{\partial t} + \mathbf{u} \cdot \nabla \mathbf{u} = -\frac{1}{\rho}\nabla p + \frac{\mu}{\rho}\nabla^2 \mathbf{u}, \qquad (2.1)$$

where $\mathbf{u} = (u, v, w)$ is the fluid velocity vector, p is the fluid pressure, μ is the fluid viscosity and ρ is the fluid density. Here, with the assumption of incompressible fluid, the mass conservation equation turns to the divergent-free of velocity field. Meanwhile, the fluid density is considered as a constant that can be taken out from the left hand side of the momentum conservation equation. Furthermore, the governing equations can be non-dimensionized as

$$\nabla \cdot \mathbf{u}' = 0,$$
$$\frac{\partial \mathbf{u}'}{\partial t} + (\mathbf{u}' \cdot \nabla)\mathbf{u}' = -\nabla p + \frac{1}{\mathrm{Re}}\nabla^2\mathbf{u}'. \tag{2.2}$$

Here, Re represents the non-dimensional Reynolds number, with the definition of

$$\mathrm{Re} = U_0 L / \nu, \tag{2.3}$$

where U_0 and L are the characteristic velocity and length, respectively, and υ is the dynamics viscosity of the fluid.

2.3 Finite Volume Method (FVM)

2.3.1 General Introduction

The finite volume method is employed and a brief introduction of FVM is presented in this section. The FVM uses the integral form of the governing equations, and the computational domain is divided into a series of control volume (cell). The integral governing equations are applied in each cell. The physical computational node usually lies at cell centre. With the help of divergence theorem, the volume integrals of certain terms can be converted to surface integrals. Meanwhile, the surface and volume integrals are approximated using suitable quadrature formulae. As a result of this, an algebraic equation for each control volume can be obtained, in which a number of neighbour nodal values appear.

For simplification, the steady transport equation, Eq. (2.4), is taken as an example to explain the process of FVM.

$$\mathrm{div}(\rho\phi\mathbf{u}) = \mathrm{div}(\Gamma\,\mathrm{grad}\,\phi) + q_\phi. \tag{2.4}$$

Here, ϕ presents a set of conserved intensive properties, for example, ϕ presents mass

conservation and momentum conservation when $\phi=1$ and $\phi=v$ respectively. q_ϕ is the corresponding source term. With the volume integral in each control volume and the divergence theorem, the transport equation can be converted as

$$\int_S \rho\phi\mathbf{u}\cdot\mathbf{n}\mathrm{d}S = \int_S \Gamma\operatorname{grad}\phi\cdot\mathbf{n}\mathrm{d}S + \int_\Omega q_\phi\mathrm{d}\Omega$$

(2.5)

Here, S is the surfaces of the control volume and Ω is the control volume, and the surface integrals can be discretized as

$$\int_S f\,\mathrm{d}S = \sum_k \int_{S_k} f\,\mathrm{d}S \approx \sum_k f_k S_k.$$

(2.6)

Here, f is the component of the convective or diffusive flux vector in the direction normal to the control volume face. Taking a two-dimensional case for example, with the grid schematic as shown in Figure 2.1, S_k runs all the four adjacent faces as the directions of k represents n (north), e (east), s (south), and w (west) respectively.
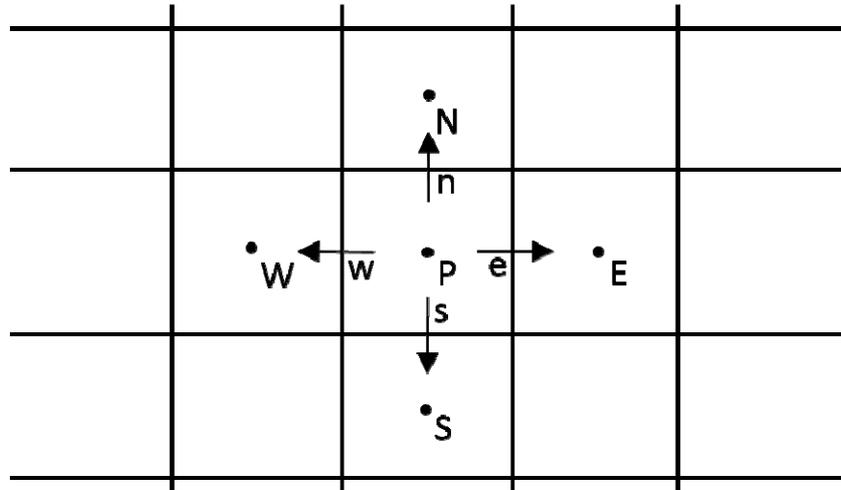
Figure 2.1 Schematic of grid system and control volume.

Meanwhile, the volume integral can be discretized as

$$Q_P = \int_\Omega q\,\mathrm{d}\Omega = \overline{q}\Delta\Omega \approx q_P\Delta\Omega.$$

(2.7)

Here, q_P is the value of q at the control volume centre. Normally, this value is available at the centre. It is the second-order accuracy if the integral volume is discretized in this way.

2.3.2 Numerical Schemes

After the scheme of surface and volume integrals is determined, the variables' value at the surface will be interpolated with certain schemes with different accuracy. Here, we will introduce some typical schemes, taking the value at surface e, ϕ_e, as an example.

(1) Upwind or backwind scheme

The simplest approximation is the upwind or backwind scheme, which is approximated from the first order derivative, hence the upwind scheme is (referring Figure 2.1)

$$\phi_e = \begin{cases} \phi_P & v_e \cdot n_e > 0 \\ \phi_E & v_e \cdot n_e < 0 \end{cases}.$$

Relevant to the upwind scheme, the backwind scheme is also straightforward, and it can be written as

$$\phi_e = \begin{cases} \phi_E & v_e \cdot n_e > 0 \\ \phi_P & v_e \cdot n_e < 0 \end{cases}.$$

(2) Linear scheme

The linear scheme means that the linear interpolation is applied between the neighbour nodes. Considering the non-uniform nodes, the form of linear scheme can be written as

$$\phi_e = \phi_E \lambda_e + \phi_P (1 - \lambda_e),$$

where λ_e is the linear interpolation factor, and it can be determined by

$$\lambda_e = \frac{x_e - x_P}{x_E - x_P}.$$

Specifically, if the grid is uniform, this linear scheme becomes to the cantering differential scheme.

(3) Quadratic Upwind scheme

Another popular scheme is the Quadratic Upwind scheme (QUICK) scheme. The QUICK scheme uses a parabolic profile to approximate the interpolation, and it is with higher order accuracy. The specified form of QUICK can be written as

$$\phi_e = \phi_U + g_1(\phi_D - \phi_U) + g_2(\phi_U - \phi_{UU}),$$

where subscript index *D*, *U* and *UU* represent the downstream, upstream and second upstream node. Meanwhile, the coefficients g_1 and g_2 can be calculated as

$$g_1 = \frac{(x_e - x_U)(x_e - x_{UU})}{(x_D - x_U)(x_D - x_{UU})}, \qquad g_2 = \frac{(x_e - x_U)(x_D - x_e)}{(x_U - x_{UU})(x_D - x_{UU})}.$$

where *x* is the coordinate of the grid. There are also higher order schemes, however, in current studies, the second order accuracy can fulfil the requirement. The readers are recommended to refer the book of Ferziger and Peric (1996) for further information of the high order schemes.

2.3.3   Brief Introduction to Linear Equation System

After the discretization of governing equations, the discretized equations turn to be an algebraic linear equation system, which can be written as

$$\mathbf{A}\phi = \mathbf{Q}. \tag{2.8}$$

Here, the matrix $\mathbf{A}$ is normally sparse, in the other words, most of the elements in matrix $\mathbf{A}$ are zero. In fact, with the structured mesh, the matrix turns to be a banded matrix. It is worthy to mention that the size of $\mathbf{A}$ is proportional to the cell number. Some typical algorithms for solving the linear equation system will be briefly introduced as below.

(1) Gauss elimination

Gauss elimination algorithm is the simplest and most basic method for solving algebra equation system. The idea of Gauss elimination is straightforward, after a systematical row transformation, i.e. multiple one row with certain factor and then subtract it from another row, the original matrix becomes to an upper or lower triangular matrix. This process is called forward elimination. Once the forward elimination is processed, the value of variable ϕ can be derived with a backward substitution.

Although Gauss elimination method is simple and straightforward, it is rarely used in CFD simulation, for the reasons of being difficult on the application to the problems with complex geometry and unstructured mesh. Besides, there are some other direct

methods (in contrast to the iterative method), such as Lower Upper (LU) decomposition and Tri-diagonal Matrix Algorithm (TDMA) method for solving the tri-diagonal matrix. However, the feasibilities of these methods rely on the complication of the problem, and they are also normally of little interest for CFD simulation.

(2) Iterative methods and definition of residual and error

As mentioned above, although the traditional Gauss elimination method can obtain an exact solution of the algebra equation system, it has the drawbacks of time consuming and low robustness. Alternatively, the iterative methods provide a simple and fast path to approach the solution, with a little sacrifice of the accuracy.

Generally, in the iterative method, we firstly guess a solution and then substitute it into the equations. With the certain algorithm, the solution can be improved from the guessed solution after a number of iterations. The process will be repeated until the error meets the criteria requirement. Assuming ϕ^n is the approximated solution after n iterations, and the equation in Eq. (2.8) turns to

$$\mathbf{A}\phi^n = \mathbf{Q} - \rho^n. \tag{2.9}$$

Here, ρ^n is the residual of the equation, which is the error lead by the approximated solution. If ϕ is the converged solution, then the iteration error is calculated as

$$\varepsilon^n = \phi - \phi^n. \tag{2.10}$$

Combining Eqs. (2.8)-(2.10), it shows

$$\mathbf{A}\varepsilon^n = \rho^n.$$

The purpose of repeating the iteration is to make the residual turns as small as possible, ideally zero. Normally, the iterative scheme for linear system can be written in a form as

$$M\phi^{n+1} = N\phi^n + B,$$

Meanwhile, by the definition, it should fullfil $\phi^{n+1} = \phi^n = \phi$ when the solution is fully converged. Thus, we have

$$\mathbf{A} = M - N \text{ and } \mathbf{Q} = B.$$

Or more generally,

$$PA = M - N \quad \text{and} \quad PQ = B.$$

Here, P is a non-singular pre-conditioning matrix.

There are more methods with iterations, e.g. Gauss-Seidel method, Conjugate gradient method, etc. The textbook of Ferziger and Peric (1996) provides more details for the reference of the readers.

2.3.4 Solutions for Navier-Stokes Equations

A brief introduction to general ideas of FVM has been given in the sections above, and here in this section, the typical solution for Navier-Stokes equations based on FVM is introduced. As we know, the Navier-Stokes equations contain two sets of equations corresponding to the mass conservation and momentum conservation. The solutions solved from the momentum equation may not satisfy the mass conservation, i.e. the velocity field is not divergence free under the incompressible fluid assumption. Therefore, the velocity solution should be corrected by the pressure field. The most popular algorithm of the pressure correction process is the SIMPLE method, which is the abbreviated form for Semi-Implicit Method for Pressure Linked Equations method. It is firstly developed by Patankar and Spalding (1972), and with further improvement and modifications, the updated method are developed, such as SIMPLER, SIMPLEC and PISO. For simplification, only the algorithm of SIMPLE method is introduced here.

In SIMPLE, the implicit method is used to calculate the momentum equation, which means an out iteration process within every time step is needed to approach exact solution. Here, for simplification, the out iteration form can be written as

$$A_P^{u_i} u_{i,P}^{m*} + \sum_l A_l^{u_i} u_{i,l}^{m*} = Q_{u_i}^{m-1} - \left(\frac{\delta p^{m-1}}{\delta x_i} \right)_P. \tag{2.11}$$

Here, l represents the index of the neighbour points of node P, m is the outer iteration counter and u_i^m is the current estimation of the solution of u_i^{n+1}. For simplification, Eq. (2.11) can be expressed as

Start

Initial guess: p^{m-1}

Solve Eq. (2.12) and

obtain u^{m*}

Solve Eq. (2.15) and
obtain pressure
correction

Update pressure guess
p^{m-1}

Update velocity
correction with Eq.
(2.14)

Update time level
$t^{n} = t^{n-1} + \Delta t$

Correct velocity and
pressure with Eq. (2.13)

NO

Converged or
not?

YES

End
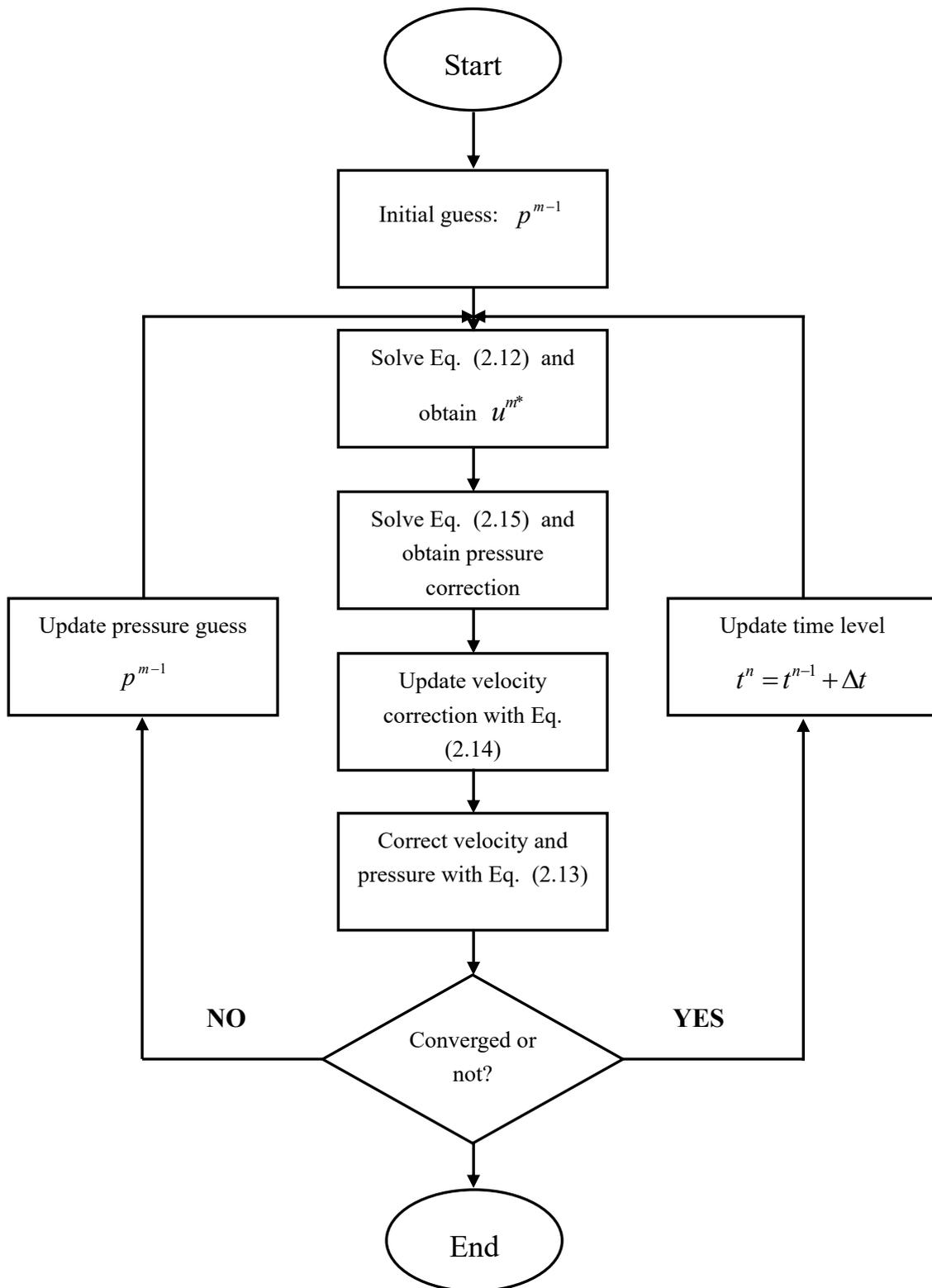
Figure 2.2 Program flow chart of the procedure of SIMPLE algorithm.

$$u_{i,P}^{m*} = \tilde{u}_{i,P}^{m*} - \frac{1}{A_P^{u_i}} \left(\frac{\delta p^{m-1}}{\delta x_i} \right)_P . \tag{2.12}$$

Here, the value of $u_{i,P}^{m*}$ dose not satisfy the continuity equation. In order to correct the velocity field, we assume the final velocity and pressure can be corrected as

$$u_{i,P}^m = u_{i,P}^{m*} + u' \quad \text{and} \quad p^m = p^{m-1} + p'. \tag{2.13}$$

If Eq. (2.13) is substituted into Eq. (2.11) and subtract Eq. (2.12), we can have the following simple form

$$u_{i,P}' = \tilde{u}_{i,P}' - \frac{1}{A_P^{u_i}} \left(\frac{\delta p'}{\delta x_i} \right)_P , \tag{2.14}$$

and it can be substituted into the continuity equation as

$$\frac{\delta}{\delta x_i} \left[\frac{\rho}{A_P^{u_i}} \left(\frac{\delta p'}{\delta x_i} \right) \right]_P = \left[\frac{\delta(\rho u_i^{m*})}{\delta x_i} \right]_P + \left[\frac{\delta(\rho \tilde{u}_i')}{\delta x_i} \right]_P . \tag{2.15}$$

Finally, the correction pressure can be derived from Eq. (2.15) and subsequently the correction velocity can be obtained from Eq. (2.14). Normally, the last term in Eq. (2.15) is neglected during the iteration process, since the exact value of $\tilde{u}'$ is expected to be zero once the iteration process is finalized. The procedure of SIMPLE algorithm can be summarized as the following flow chart as shown in Figure 2.2.

2.4 Numerical Techniques for Fluid-structure Interaction

The physical models, which will be studied in this thesis, that moving solid boundaries are normally included in the computational domain, are a common feature in Fluid-Structure Interaction (FSI) problems. In the past two decades, there are several numerical techniques developed to handle this kind of problems. The most traditional way is to include re-meshing process in every time step, which may cost a lot of computational time. It is worthy to mention that there are also some other novel methods which are quite computationally efficient, such as the immersed boundary method (Mittal and Iaccarino, 2005) and fictitious domain method (Glowinski et al., 1999). However, for these novel methods, the computational efficiency is achieved by

scarifying the computational accuracy. In such a situation, the dynamic mesh method turns to be an applicable approach, which can handle complicated moving boundary and meanwhile retain the requirement of computational accuracy. Therefore, the dynamic mesh method is applied in the simulation work of this thesis, and it will be briefly introduced here in this section.

The concept of dynamic mesh method is straightforward. The fully immersed solid boundary is moving in every time step, inducing the control volumes moving accordingly, assuming the moving velocity is $\mathbf{U}_b$, the momentum equation can be re-formulated in integral form as

$$\frac{d}{dt}\int_V \rho\mathbf{U}\,dV + \oint_S d\mathbf{s}\cdot\rho(\mathbf{U}-\mathbf{U}_b)\mathbf{U} = \oint_S d\mathbf{s}\cdot(-p\mathbf{I}+\rho\nu\nabla\mathbf{U}), \qquad (2.16)$$

which is called the Arbitrary Lagrangian Eulerian (ALE) formulation (Ferziger and Peric, 1996).

Normally, there are two situations when the dynamic mesh method is applied in the moving boundary problems. Firstly, if the moving boundary is rigid, e.g. flapping wing, the control volumes in the whole domain can move with the rigid body with the same velocity. Secondly, if the moving boundary is flexible, e.g. an undulation fish (foil), the method becomes complicated and control volumes at different locations may move with different velocity. In the other word, the meshes will be compressed or stretched. In the latter situation, special algorithm is required to control the mesh deformation. The whole mesh system would be re-meshed according to the quality of the mesh. In this thesis, both situations will be applied.

2.5 Typical Numerical Tests

Three typical numerical tests are simulated in this section with the models of two-dimensional foil under prescribed plunging and hovering motions. The foil is with sinusoidal plunging motion in the first model, and a combination of sinusoidal plunging and pitching in the second one. The third model is an innovative test directing to fill in the gap of dynamic response of foil to a non-sinusoidal plunging

motion. All of them aim to repeat the classic work, and the way of generating numerical cases and analysing results can be applied as the baseline knowledge of all the simulation work in this thesis. It is noticed that more verification cases are presented together with the specific physical models in the individual chapters in the following part of this thesis for better describing algorithm and problems.

The computational approach including the solver and definitions of both general input and output parametric properties are firstly indicated, and then the results of three test cases are described briefly in the following sub-sections.

2.5.1   Computational Approach

2.5.1.1   Solver

The unsteady flow field around the foil is solved using the commercial CFD package FLUENT versions 12.1, 13.0 and 14.0, with an unsteady incompressible solver and second-order upwind spatial discretization method. The flow field is discretized by fully structured mesh and assumed to be laminar due to the flow separation on the surface of foil boundaries is in an acceptable range for hydrodynamic force prediction. The plunging motion of the foil is modelled using the 'dynamic mesh' feature, and the whole grid and foil is moved as a rigid body.

2.5.1.2   General parameter definitions

The sinusoidal plunging motion of foil is described as

$$y(t) = hc\sin(\omega t),\qquad(2.17)$$

where h is non-dimensional flapping amplitude normalized by foil chord length c, and ω is the flapping angular frequency, and $\omega=2\pi f$, with f of the flapping frequency. The time period, T, can be obtained by $1/f$.

The sinusoidal pitch motion is defined as

$$\theta(t) = \alpha_0 \sin(\omega t + \psi),\qquad(2.18)$$

where ψ is phase between pitching and plunging motion, and α_0 is the pitching amplitude.

The Reynolds number and Strouhal number are defined in Eq. (2.19) and Eq. (2.20), respectively, where ρ is fluid density, μ is fluid kinematic viscosity, A is the foil trailing edge net vertical motion, and U_0 is uniform inflow velocity.

$$\text{Re} = \frac{\rho c U_0}{\mu}, \tag{2.19}$$

$$St = \frac{fA}{U_0}. \tag{2.20}$$

The output for the flapping foil under prescribed plunging motion can be presented by thrust force coefficient, C_T, and input power coefficient, $\hat{P}$, determined as Eq. (2.21) and Eq. (2.22).

$$C_T = \frac{F_T(t)}{\frac{1}{2}\rho U_0^2 c}, \tag{2.21}$$

$$\hat{P} = \frac{F_L(t)\dot{y}(t)}{\frac{1}{2}\rho U_0^3 c}. \tag{2.22}$$

The propulsion efficiency can be obtained from the ratio of output power upon input power in one cyclic revolution. As shown in Eq. (2.23) or Eq. (2.24), the efficiency of η_1 and η_2 are for cases with purely plunging motion and combination motion of plunging and pitching respectively. The numerators are the output power given by the multiplication of inflow velocity and thrust force, $F_T(t)$, and denominators are the input power calculated by vertical velocity, $\dot{y}(t)$ and lift force, $F_L(t)$ or angular velocity, $\dot{\theta}(t)$ and toque, $M(t)$.

$$\eta_1 = \frac{U_0 \int_t^{t+T} F_T(t)dt}{\sum_t^{t+T} F_L(t)\dot{y}(t)}, \tag{2.23}$$

$$\eta_2 = \frac{U_0 \int_t^{t+T} F_T(t)dt}{\sum_t^{t+T} (F_L(t)\dot{y}(t) + M(t)\dot{\theta}(t))} \, . \tag{2.24}$$
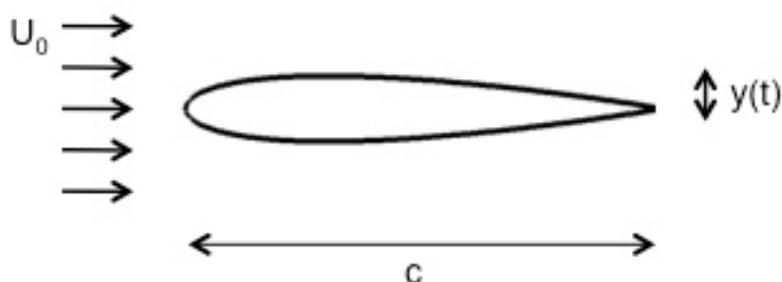
Figure 2.3 Sketch of foil under purely plunging motion.
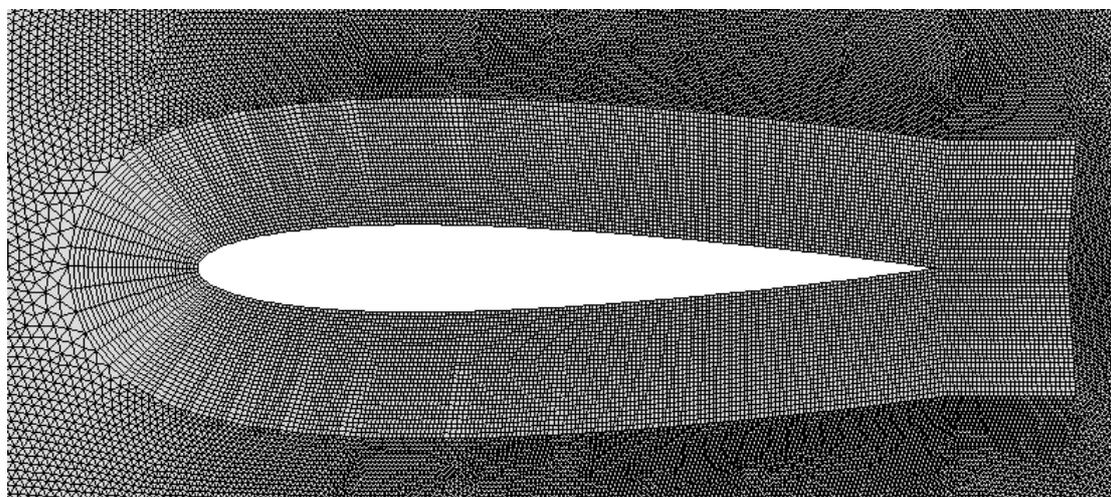
Figure 2.4 Mesh around the foil surface in the test case of medium grid.

2.5.2 Foil with Sinusoidal Plunging Motion

The model with NACA0012 foil section (with chord length c) is shown in Figure 2.3, with sinusoidal plunging motion defined in Eq. (2.17) within a uniform inflow environment. The Dynamic Mesh Feature is activated for enabling the foil's prescribed plunging motion. The computational domain is 20 and 10 times of foil

chord length in stream-wise and perpendicular directions. The grid independence test is conducted for a coarse grid (300 intervals on the foil surface, 164905 cells in total), a medium grid (400 intervals on the foil surface, 225351 cells in total) and a fine grid (500 intervals in the foil body, 297134 cells in total), composed by structured mesh near the foil and unstructured mesh in outer domain as in Figure 2.4. Thrust coefficients are shown in Figure 2.5, indicating differences due to grid size for a time-step size of $T/400$ (T is flapping period). The time-step size range is selected according to the results based on a few preliminary test cases and the common settings for the fluid solver in ANSYS FLUENT package. Figure 2.5 shows that the medium grid case is able to achieve the accuracy as the fine grid case. Therefore the medium grid is used for all computations to ensure the accuracy and minimize the time and memory consumption.
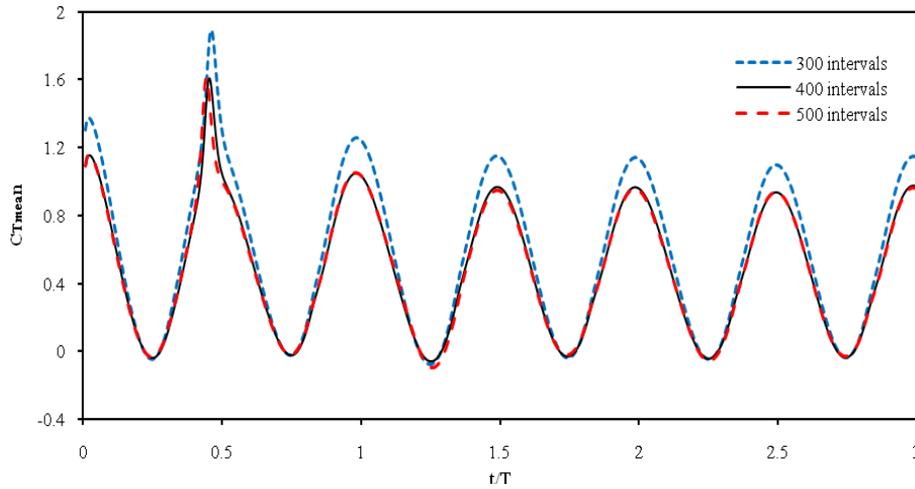
Figure 2.5 Grid independence test for purely plunging foil (St=0.32, Re=20000 and h=0.175).

The time averaged thrust coefficient ($\overline{C}_T$) and propulsive efficiency (η_1) are plotted against Strouhal (St) number in Figure 2.6, and it shows the present results are in good agreement with the previous results (Heathcote et al., 2008). As St increases, there is a larger difference in thrust force between the experimental results and those of previous simulations due to uncertainties in the limitations of laminar model and numerical deviation; flow separation may appear for a plunging foil at faster flapping

frequency and high Re. The results show that the thrust force is proportional to the St number [representing plunging frequency (f) when inflow velocity and plunging amplitude are constant], while the propulsion efficiency drops down apart from the peak point at St number of 0.15. It also confirms that an efficiency peak naturally emerges somewhere in the range of $0.1<St<0.4$.
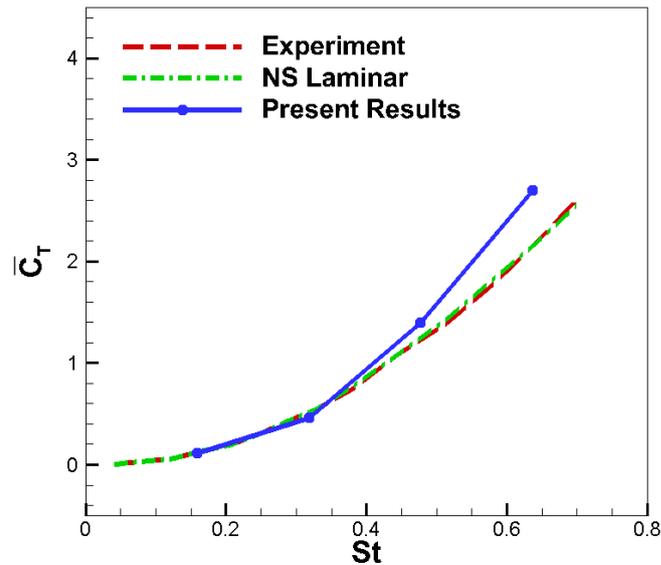
(a)
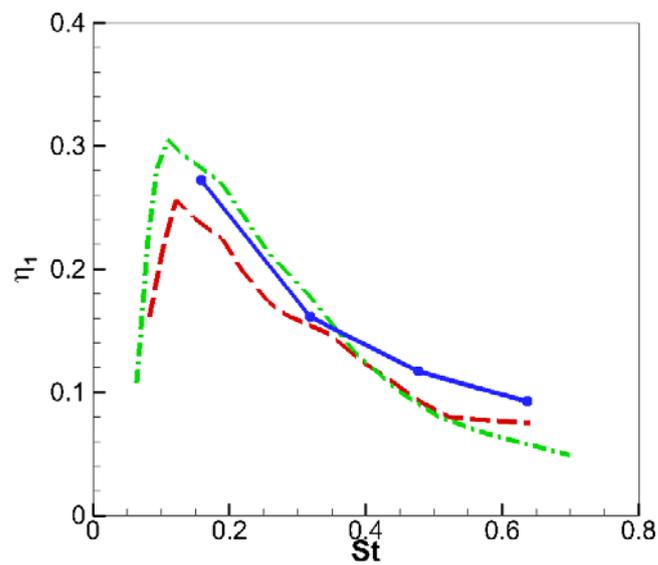
(b)

Figure 2.6 Comparison with Heathcote et al. (2008) of (a) averaged thrust coefficient and (b) propulsive efficiency against St number of the case with purely pitching motion (Re=20000 and h=0.175).
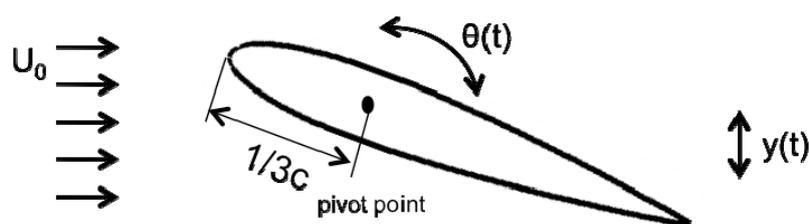
Figure 2.7 Sketch of foil under plunging and pitching motion.

2.5.3   Foil with Plunging and Pitching Motion

The NACA0012 foil is also simulated under hovering motion with both plunging and pitching motion following the previous work (Anderson et al., 1998; Garrick, 1937; Young and S. Lai, 2007), and as the sketch shown in Figure 2.7, the pivot point is located on the centreline of foil and at the distance of $1/3c$ away from the leading edge. The mesh resolution, domain size and time-step size is same as the case in Section 2.5.2. Results with acceptable deviation are obtained and plotted in Figure 2.8. Experiments along with simulations of theoretical and CFD methods reveal the occurrence of a peak in propulsive efficiency of such a hovering foil. Young and S. Lai (2007) further indicate in their paper that the magnitudes of the peak efficiencies are influenced by a number of physical mechanisms, a flow separation and leading-edge shedding effects appear to be controlled by the reduced frequency by limiting the time available both for vortex formation and convection of the vortex over the foil surface. The trend of thrust force coefficient and efficiency with *St* number is similar to the results of other researchers. The thrust coefficient is under estimated due to the uncertainties possibly brought by the big flapping amplitude. Along with the verification results in Figure 2.6, in which the thrust is over estimated, the test cases indicate that the method is feasible of predicting general trends for foil models with kinematic motion, however the accuracy of variable quantification is subject to individual case. It is necessary to carry out relevant validation tests for all

the new built models, and more verification cases are presented together with the specific physical models in the individual chapters.
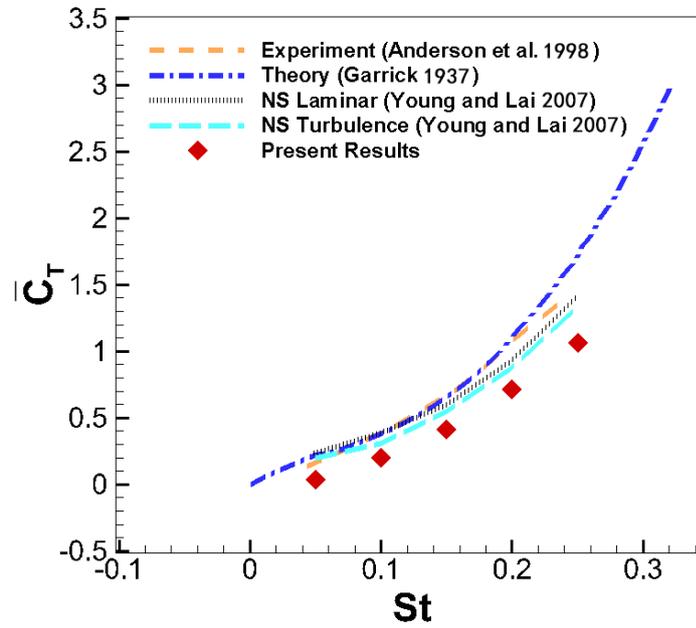
(a)
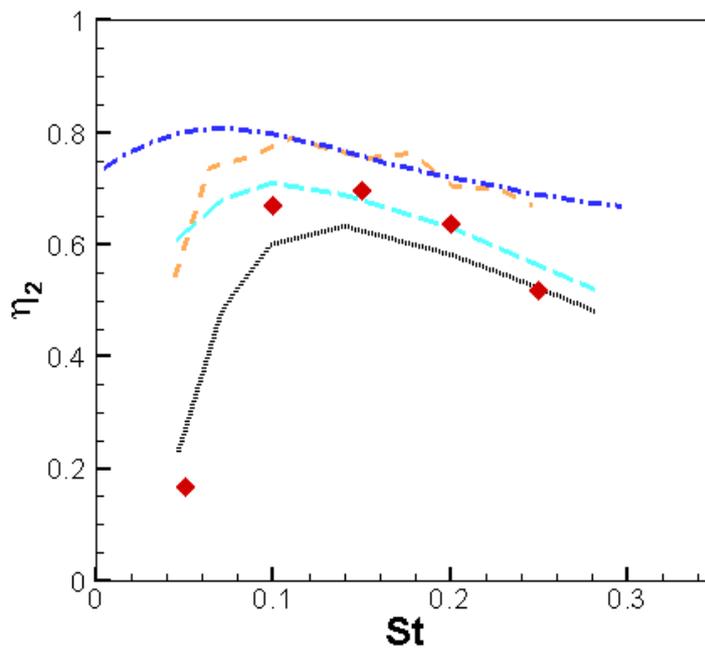
(b)

Figure 2.8 Comparison with previous results of (a) averaged thrust coefficient and (b) propulsive efficiency against St number of the case with plunging and pitching motion. (Re=40000, h=0.75, ψ=90°, α_0=15°).

2.5.4   Foil with Non-sinusoidal Plunging Motion

Following with the first two cases, investigations on the purely flapping NACA 0012 foil are conducted under non-sinusoidal motion. The mesh resolution and time-step size is same as the case in Section 2.5.2. With an adjustable parameter β, the non-sinusoidal trajectory profile is achieved with Eq. (2.25) (Xiao et al., 2010) , and the trajectory within one revolution under different β is shown in Figure 2.9. The plunging profile becomes more non-sinusoidal with bigger β.
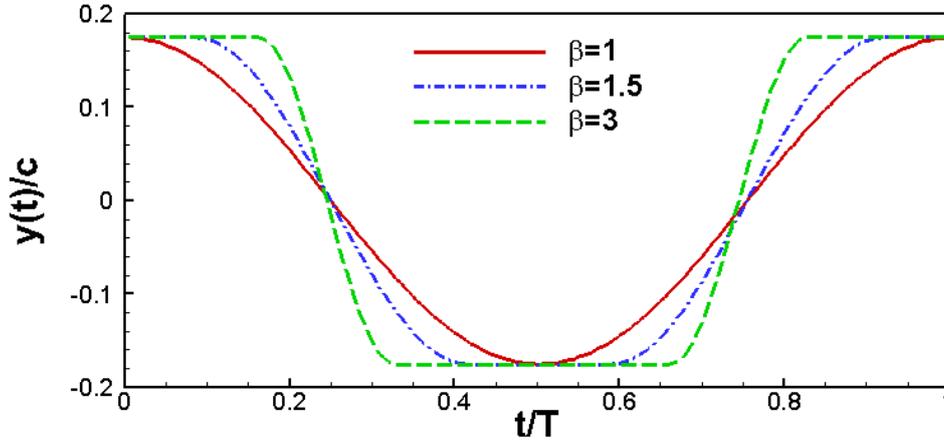
Figure 2.9 Variation of instantaneous plunging profile in one period with h=0.175.

$$y(t) = \begin{cases} hc, & 0 < t \le \dfrac{\pi}{2\omega}(1-\dfrac{1}{\beta}) \\[2mm] hc\sin\left(\beta\omega t + \pi(1-\dfrac{\beta}{2})\right), & \dfrac{\pi}{2\omega}(1-\dfrac{1}{\beta}) < t \le \dfrac{\pi}{2\omega}(1+\dfrac{1}{\beta}) \\[2mm] -hc, & \dfrac{\pi}{2\omega}(1+\dfrac{1}{\beta}) < t \le \dfrac{\pi}{2\omega}(3-\dfrac{1}{\beta}) \\[2mm] hc\sin\left(\beta\omega t + \pi(2-\dfrac{3\beta}{2})\right), & \dfrac{\pi}{2\omega}(3-\dfrac{1}{\beta}) < t \le \dfrac{\pi}{2\omega}(3+\dfrac{1}{\beta}) \\[2mm] hc, & \dfrac{\pi}{2\omega}(3+\dfrac{1}{\beta}) < t \le \dfrac{2\pi}{\omega} \end{cases} \qquad (2.25)$$

It is clearly seen from Figure 2.10 that the thrust forces always increase with a higher St number while the efficiency has the opposite trend, which are same as the last two

cases. The non-sinusoidal squared plunging profile can dramatically enhance the thrust force but lead to an inefficient way in general situations. However the efficiency achieves the peak value at St=0.32 and β=1.5, which exhibits the propulsion efficiency can be improved under the certain parameters. Both instantaneous thrust coefficient and input power in Figure 2.11 rise impulsively when the foil changes rapidly from upmost to lowest position and vice versa under non-sinusoidal profiles.
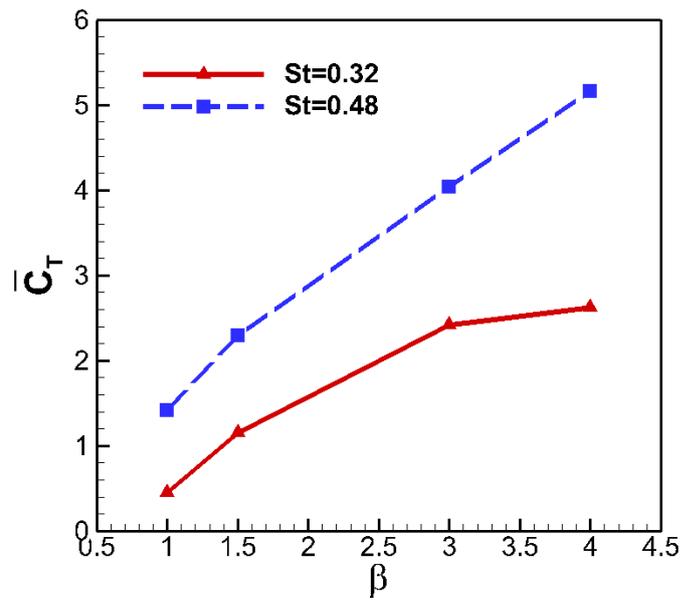
(a)
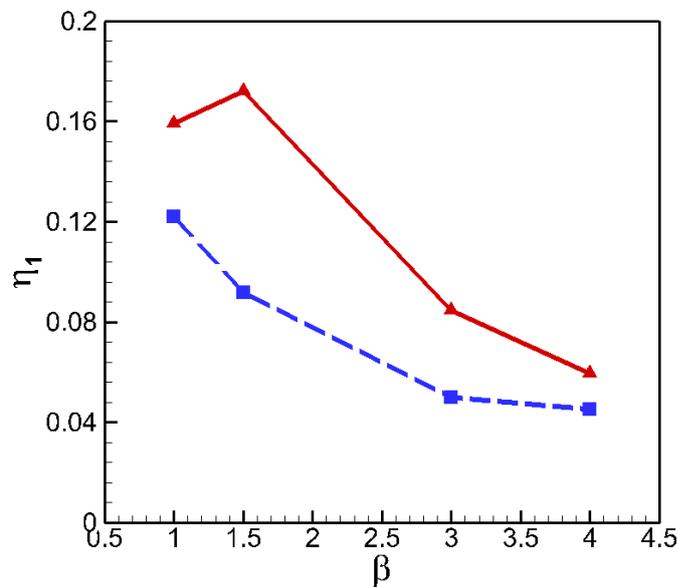
(b)

Figure 2.10 (a) Thrust coefficient and (b) propulsion efficiency of 2D foil under the non-sinusoidal motion. (h=0.175, St=0.32 & 0.48, Re=20000).
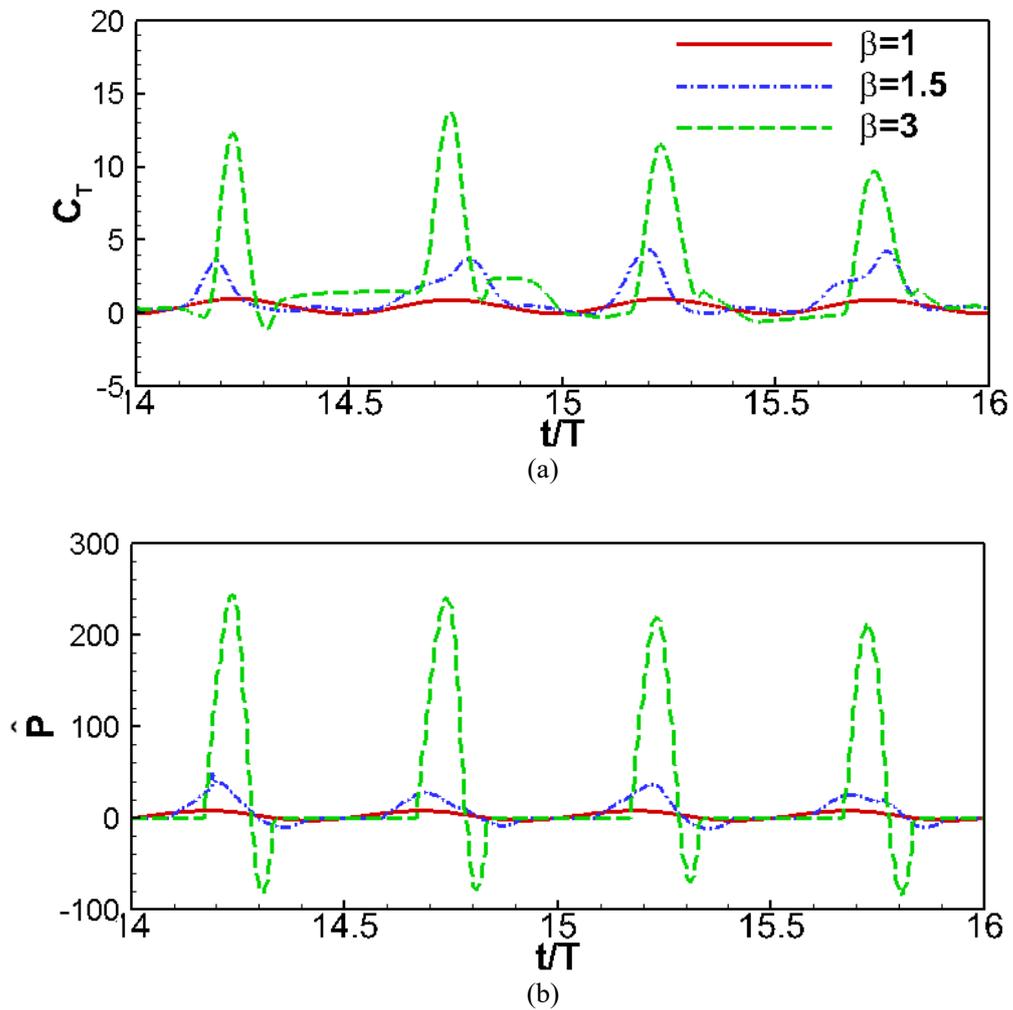
Figure 2.11 (a) Instantaneous thrust force coefficient and (b) input power coefficient for the foil under non-sinusoidal motion. (h=0.175, St=0.32, Re=20000).

Chapter 3 Flapping Wing with Translational Freedom

3.1 Introduction

The aim of the study in this chapter is to extend the work for a flapping foil with one degree of freedom (1DoF) in translational direction, to a 3D wing under low aspect ratio condition.

3.2 Mathematical Model

3.2.1 One Degree-of-freedom Flapping Wing Model

Figure 3.1 illustrates the wing under current investigation, i.e. a 3D rectangular wing with an elliptical cross-section. The ratio of thickness to chord length is 0.1, and the aspect ratio is defined as AR=S/c, where S is the wing span (wing tip to tip distance) and c is the chord length. Besides a tethered plunging motion, the wing is allowed to move in lateral direction. It has a freedom in in-line (x) direction, which is solely determined by the fluid-motion coupling between fluid and wing under the propulsion of a prescribed plunging motion in transverse direction. In this chapter, only the in-line freedom of wing is released, while the rotational freedom in pitch direction is not allowed.

Referring to Figure 3.1, the wing motions $\mathbf{u}_b = (u_b, v_b, 0)$ can be explained as follows:

a) Specified sinusoidal plunging motion v_b is prescribed as

$$v_b(t) = hc\omega \sin(\omega t)$$

.   (3.1)

b)   An induced velocity u_b is solely determined by the unsteady fluid forces through Newton's Second Law

$$m_b \frac{du_b}{dt} = F_x ,$$

(3.2)

where m_b is the mass of wing, F_x is the hydrodynamic force in x direction including both pressure force and viscosity force. The density ratio σ is defined as the ratio between the density of wing and fluid, and $m_b = \sigma \rho V$, where V is the volume of the wing.
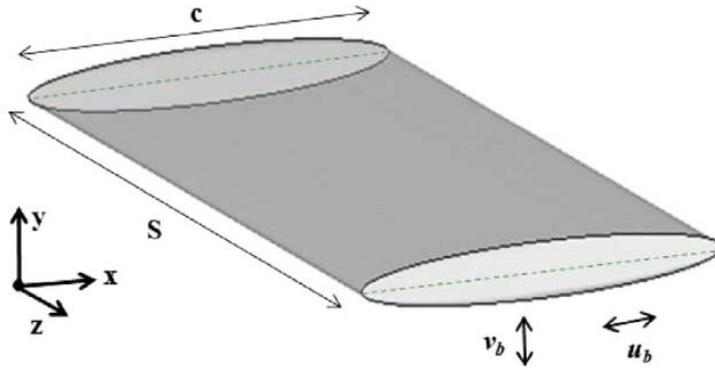
Figure 3.1 Sketch of wing with an elliptical cross-section.

The instantaneous propulsion velocity u_b is obtained by integrating Eq. (3.2) with a first-order explicit scheme

$$u_b^t = \frac{F_x^{t-\Delta t}}{m_b} \Delta t + u_b^{t-\Delta t} ,$$

(3.3)

where u_b^t and $u_b^{t-\Delta t}$ are x direction velocities at time instants t and $t - \Delta t$.

3.2.2   Fluid Solver

The hydrodynamic force in Eq. (3.2) is integrated from Navier-Stokes equation. The flow field is simulated using the commercial CFD package FLUENT version 12.1.4. The body's plunging motion (v_b) is imposed on the domain using Dynamic Mesh Function in FLUENT.

The computational domain is 21, 11 and 18 times of wing chord length in in-line (x), transverse (y) and span-wise (z) directions, respectively, which is shown in Figure 3.2. Computational boundary conditions are set with fluid velocity and pressure disturbance to be zero, and no-slip wall boundary condition is used on the wing surface. Initial fluid velocity is set to be zero everywhere in the domain. The flow field is assumed to be laminar as the induced translational Reynolds number (Re_u) is relatively small. The parallel processing setup is established through High Performance Computer, which significantly reduces the computing time for unsteady problem, especially for three-dimensional cases.
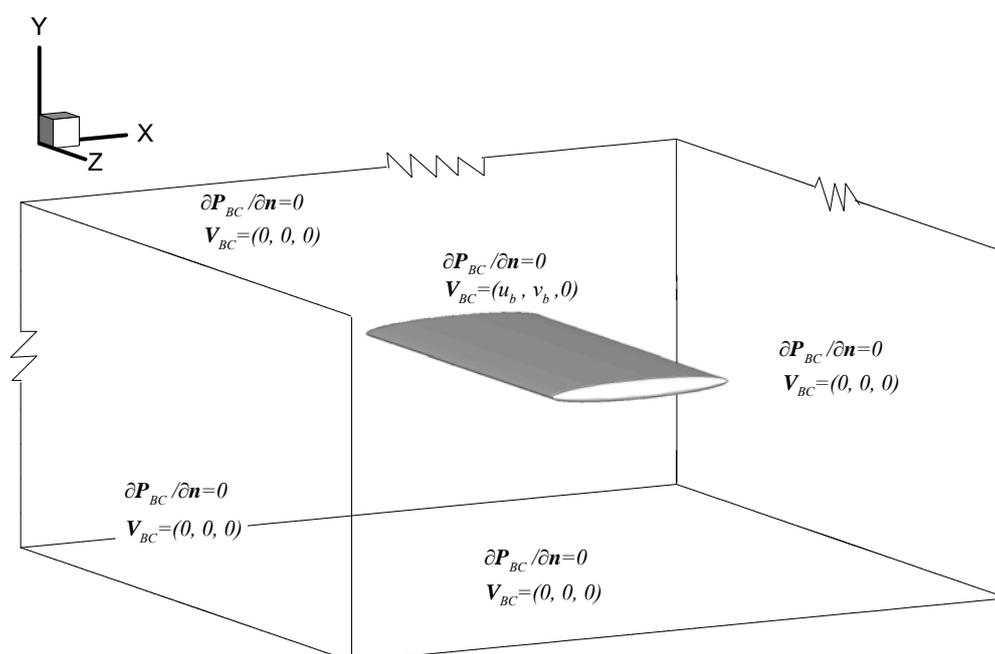
Figure 3.2 Computational domain and boundary conditions.

The mesh over the wing is shown in Figure 3.3. Structured mesh is used near the wing surface. Both rectangular and triangular grids are distributed over the section of $z = 0$, and hexahedral and wedge mesh elements are generated along z direction. A non-symmetric mesh is distributed over the wing surface along z direction and x direction. In particular, near the wing tip area, the mesh is specially refined, ensuring the grid numbers are sufficient enough to precisely capture the unsteady wing tip vortex.

Z=0 section
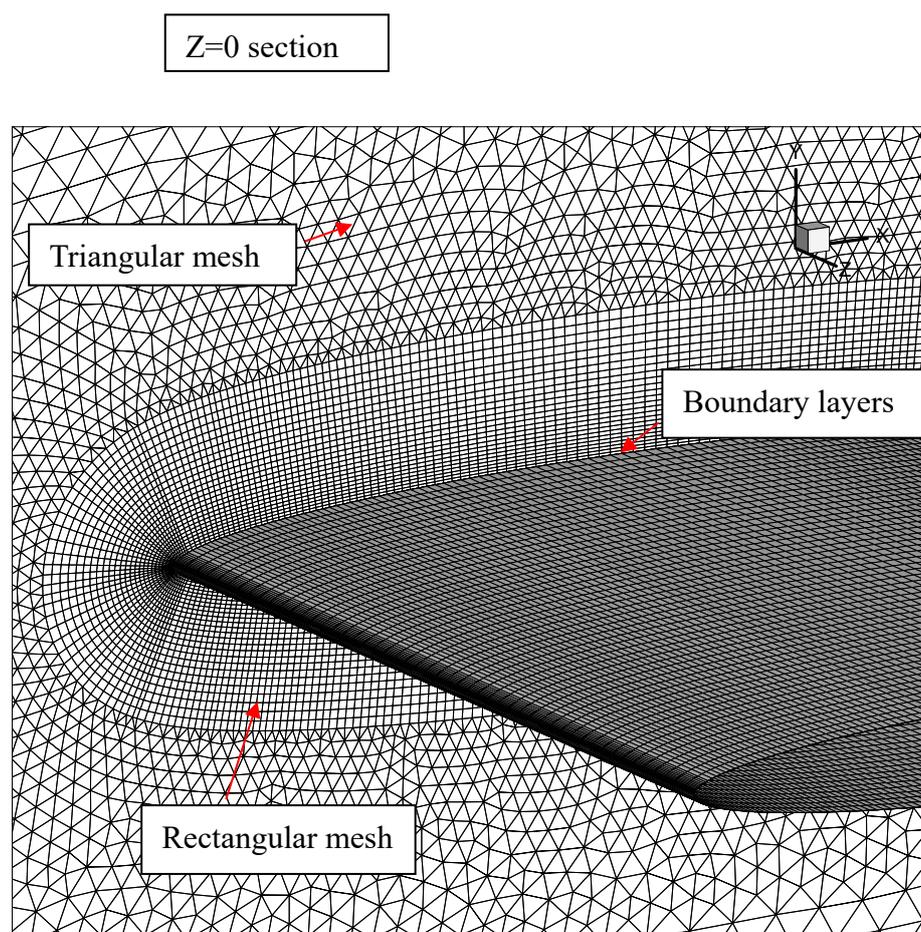
Figure 3.3 Grid distribution over wing surface.

3.2.3 Fluid – Structure Coupling Algorithm

The schematic diagram for fluid and wing body motion coupling is shown in Figure 3.4. Generally, fluid forces and updated positions exchange between fluid solver and UDF solver. At each time step, the simulation starts from updating the body position with the help of Dynamic Mesh Function. Then the fluid solver updates the flow field accordingly by solving Eq. (2.1) with second-order upwind spatial discretization accuracy, and first-order implicit discretization accuracy which is limited by the dynamic mesh approach adopted in ANSYS-FLUENT. An updated fluid force is obtained from the fluid solver, which can be used as an input variable in UDF code. The UDF code is written with an algorithm based on Eq. (3.3) for producing an updated body velocity and position. The iteration close with imposing the updated body position into the fluid solver, and a new time step begins.
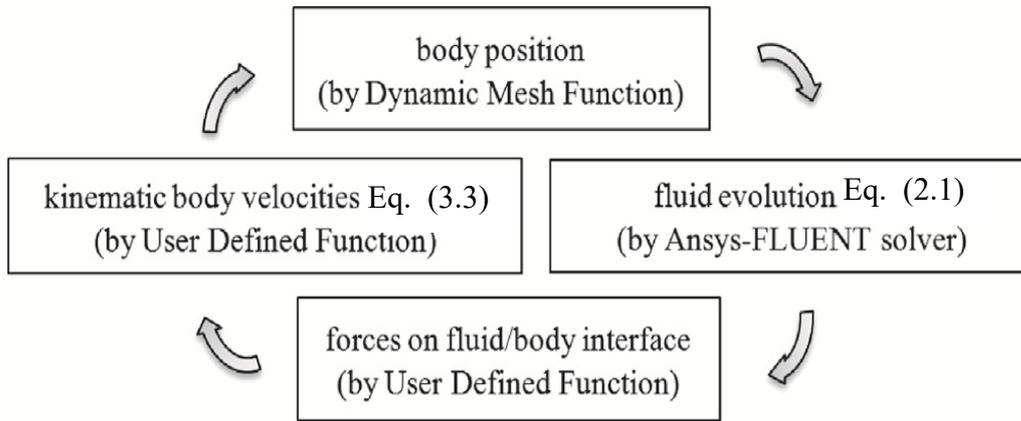
Figure 3.4 Schematic diagram for fluid and wing body motion coupling.

The non-dimensional x direction force coefficient C_{Fx} is defined as

$$C_{F_x} = \frac{F_x(t)}{\frac{1}{2}\rho\left(f(hc)\right)^2 c\bar{l}},$$ (3.4)

where F_x is the hydrodynamic force in translational direction, $\bar{l}$ is the characteristic length assuming one unit herein.

Cycle-averaged input power P input and input power coefficient C_p are calculated by the following equation:

$$C_p = \frac{P}{\frac{1}{2}\rho\left(fhc\right)^3 c\bar{l}}$$
$$= \frac{v_b(t)F_y(t)}{\frac{1}{2}\rho\left(fhc\right)^3 c\bar{l}},$$ (3.5)

where F_y is the hydro-force in transverse direction.

Two Reynolds numbers are defined here, depending on the various velocities:
(a) Frequency Reynolds number Re_{fr}:

$$Re_{fr} = \frac{\rho f(hc)c}{\mu}.$$ (3.6)

(b) Translational Reynolds number Re_u:

$$\text{Re}_u = \frac{\rho c |\bar{u}_b|}{\mu},$$ (3.7)

where $|\bar{u}_b|$ is the absolute value of mean horizontal speed in the quasi-steady status. In addition, the corresponding instantaneous Reynolds number is represented as $\tilde{\text{Re}}_u$, based on the instantaneous velocity u_b.

Instantaneous non-dimensional translational velocity U is

$$U = \frac{u_b(t)}{f(hc)}.$$ (3.8)

Moreover, apart from the classic definition as Eq. (2.20), Strouhal number can be obtained from the Reynolds number as in Eq. (3.9).

$$St = \frac{2\text{Re}_{fr}}{\text{Re}_u}.$$ (3.9)

3.3 Numerical Validation

3.3.1 Grid Independence Study

A grid and time-step size independence test is conducted with a fine grid and a medium grid, and two time-step sizes, $T/200$ and $T/400$ (T is the prescribed flapping cycling period), as the following three cases:

- Case 1 (AR1.5-F): 180 intervals over the elliptical edge and 120 intervals along the span-wise edge, totally 4 535 550 mesh elements, time-step size $T/200$.

- Case 2 (AR1.5-M): 130 intervals over the elliptical edge and 80 intervals

along the span-wise edge, totally 1 281 140 mesh elements, time-step size *T*/200.

- Case 3 (AR1.5-MT): 130 intervals over the elliptical edge and 80 intervals along the span-wise edge, totally 1 281 140 mesh elements, time-step size *T*/400.

Computational results of the instantaneous drag force C_{Fx} are shown in Figure 3.5, indicating a close result between the medium mesh and the fine mesh and these two time steps. Therefore the medium grid and the *T*/200 time-step size are used for all computations to ensure accuracy and meanwhile minimize the time and memory consumptions.
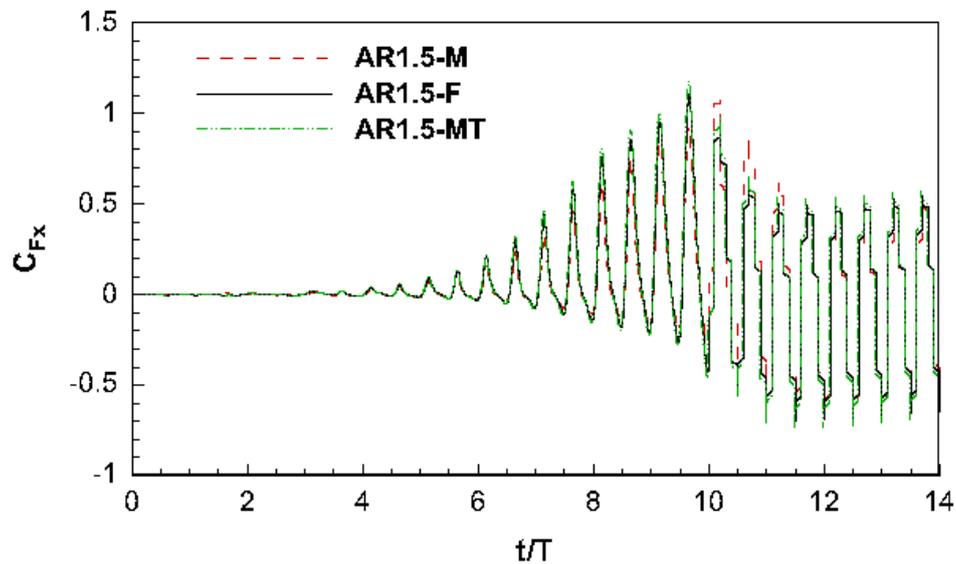
Figure 3.5 Mesh and time-step sensitivity study for three-dimensional wing (*h*=0.5, AR=1.5, Re$_{fi}$=60, σ=4.0).

Due to an explicit time-marching scheme adopted in in-line *x* direction [Eq. (3.3)], the maximum time step is restricted under scheme stability constrains. To ensure numerical convergence, we monitor the iterations at each physical time step. The

iteration continues until the momentum equation residual is reduced by three orders of magnitude.
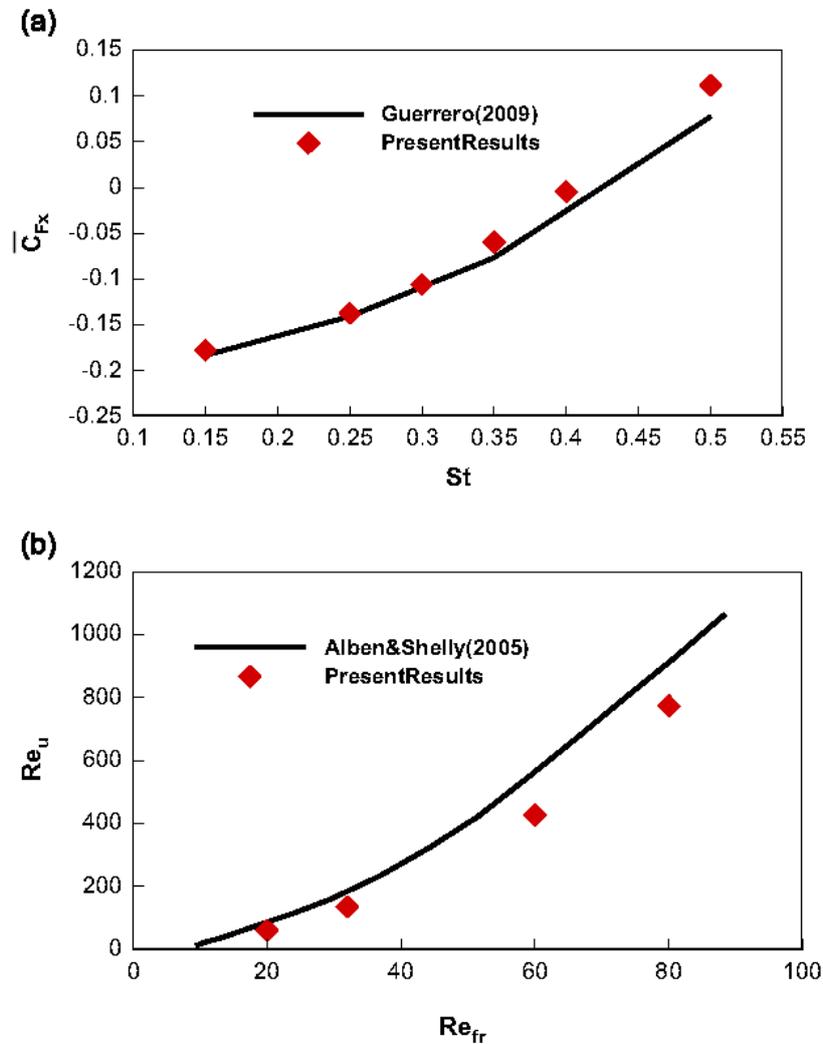
Figure 3.6 Validation of results comparison with Guerrero (2009) and Alben and Shelley (2005).

3.3.2   Validation with Previous Results

To validate our developed numerical strategies, two test cases are performed. The first one is for a forced 3D plunging wing studied previously by Guerrero (2009). The results are shown in Figure 3.6 (a) indicating a consistency with the results of Guerrero (2009). The second validation test is carried out on a 2D self-propelled (1DoF) foil with a prescribed heave motion with free movement in in-line x direction

(Alben and Shelley, 2005). This problem is adopted for verifying the capability of our in-house developed UDF code based on Eq. (3.2) and (3.3) to deal with a coupled fluid-structure-interaction problem. In Figure 3.6 (b), the in-line induced velocity (Re_u) is compared with Alben and Shelley's data. The range of Re_{fr} varies from 20 to 80, and the present results show a good agreement at low Re_{fr}, but with the under-estimated Re_u at large Re_{fr}. This is probably due to the different numerical methods used in the two studies. Unfortunately, no other relevant simulation or experimental data are available for our comparison.

In the following, investigation is first carried out on comparing the evolution process of left-right symmetric wing with large and medium aspect ratios, which are treated by 2D and 3D respectively. After then, we further discuss the self-propelled phenomenon in the aspects of 3D effect, density ratio effect and perturbation effect on the induced in-line (x) direction locomotion ability. Wake structures of wings are presented with different aspect ratios, and the dynamic behaviours and propulsive properties of passive plunging wing is analysed in terms of typical kinematic quantities, such as the mean horizontal speed and the St number.

3.4 Results and Discussion

In this section, effects of amplitude h, aspect ratio AR, frequency Reynolds number Re_{fr} and mass ratio σ are investigated systematically. The parameter ranges are summarized in Table 3.1. Here, the non-dimensional flapping amplitude h is simplified as 0.5, Re_{fr} ranges in 20-80 and σ is between 4 and 32, which are consistent with other previous work (Lu and Liao, 2006; Miller and Peskin, 2004; Spagnolie et al., 2010; Zhang et al., 2010), where these parameters are motivated by the real animal locomotion. Aspect ratios (0.5-∞) are varied to explore the 3D effect, and the infinite large aspect ratio wing represents a 2D wing.

Table 3.1 Parameters list of self-propelled flapping wing.

Parameters	Values
h	0.5
Re_{fr}	20, 32, 45, 60, 80
AR	∞, 0.5, 1.0. 1.5, 2.0, 4.0, 6.0
σ	4, 6, 7, 8,10, 20, 32
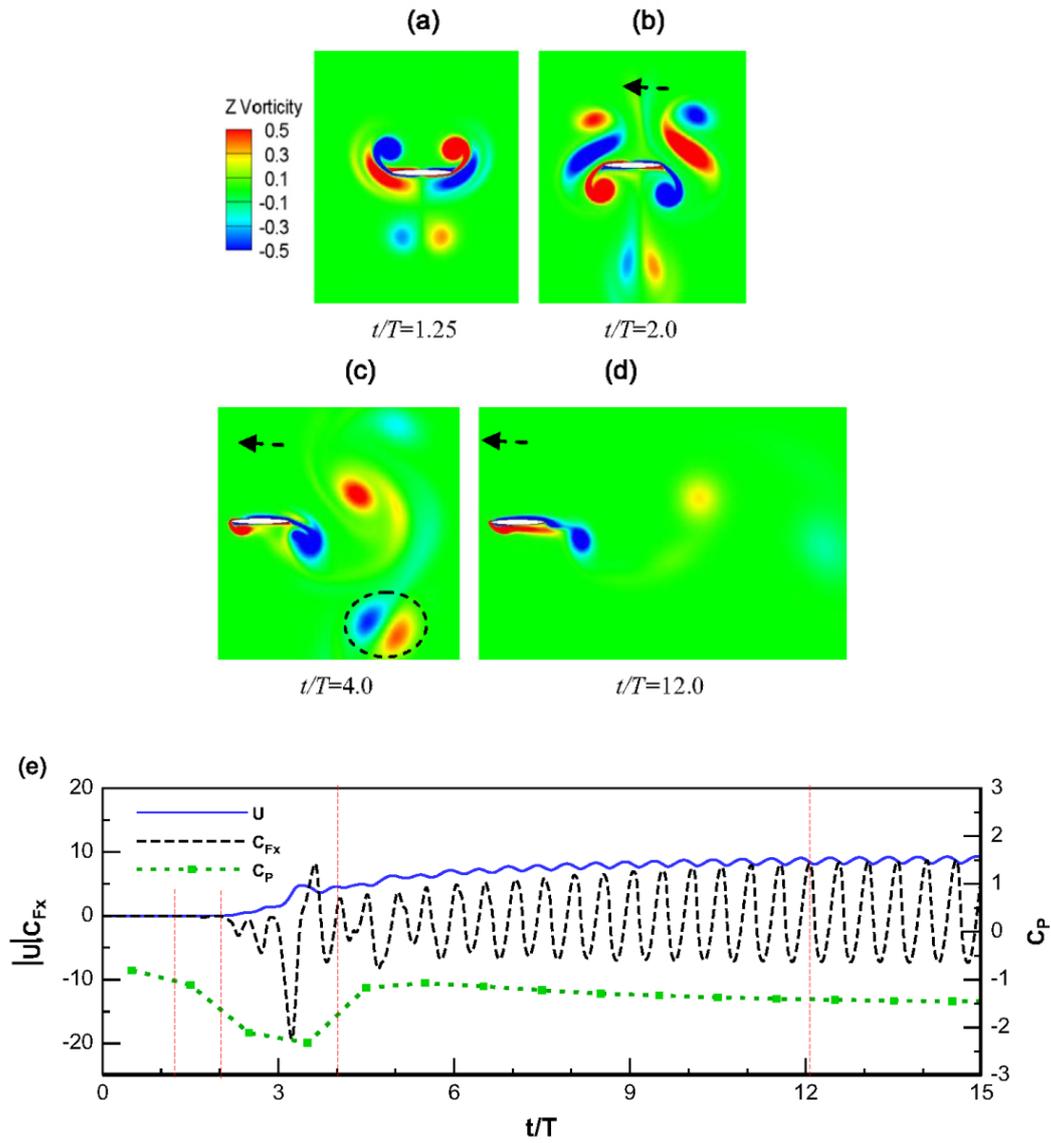
Figure 3.7 Evolution process for a symmetric foil with AR=∞ (2D), Re_{fr}=80, σ=4.0. (a) (b) (c) (d) vortex topology at four instants; (e) instantaneous horizontal velocity, fluid force and the cycle-averaged-input power coefficient.

3.4.1   Evolution Process

With a two-dimensional symmetric foil model, the propulsion mechanisms of how locomotion transduces from the oscillation into translational motion in stationary water have been well studied in the past. In particular, the interesting phenomenon of symmetry breakdown is well documented in previous studies (Alben and Shelley, 2005; Lewin and Haj-Hariri, 2003; Lu and Liao, 2006; Vandenberghe et al., 2006; Vandenberghe et al., 2004). However, the phenomenon may turn to be different when the model is changed to a three-dimensional wing. Here, the evolution process of a three-dimensional wing (AR=4.0) in comparison with a two-dimensional foil (AR=∞) is first studied. Vortical contours at four instants, fluid forces, lateral velocities and cycle-averaged-input powers are plotted in Figure 3.7 and Figure 3.8, where dashed arrows present traveling direction and dashed circle presents vortex dipole, and solid arrows present velocities of tip vortex. The result of a 3D wing are quantified same as that of a 2D foil under same Re_{fr} and σ. Since the direction of induced lateral motion is randomly selected, the moduli of velocity are used for presenting the evolution process and ensuring that a positive Re_u is always obtained. In the case of negative in-line movement, a reflection plot of the vortex topology is presented.

It can be seen that the evolution mechanisms of a wing (AR=4.0, in 3D) is pretty similar as those of a foil (AR=∞, in 2D). In particular, at early stage, both the foil and the wing plunge with a flow structure being left-right symmetric. Typical flow structures are shown in Figure 3.7 (a) and Figure 3.8 (a). The net force along the in-line direction is nearly zero at this moment. As there is no constraint in translational direction, any small flow disturbance near the wing will cause the asymmetric flow structure and eventually leads to the foil/wing moving to one side [Figure 3.7 (b) and Figure 3.8 (b)]. Once the wing starts to move, a transit period is needed before it finally reaches to a stable state, within which the vortex collides with others, resulting in a vortex dipole [as the dashed circle in Figure 3.7 (c) and Figure 3.8 (c)] which carries asymmetric suction forces at left and right edges. Consequently, horizontal forces vibrate with amplified amplitudes, leading to increased accelerations, and further rapidly increasing of horizontal velocities is caused. Finally, a stable translational locomotion is achieved as the wake being a reversed von Kármán structure [Figure 3.7 (d)] or elongated ring loops [Figure 3.8 (d)]. Both the velocity

and force vary periodically, with net forces around zero. The developing time and translational directions is sensitive to the initial conditions, as we will show later. Meanwhile, the magnitude of cycle-averaged-input power increases dramatically upon the flow symmetry eliminates. After then it returns to a constant at the stable state. The negative values indicate an input power on foil and wing.
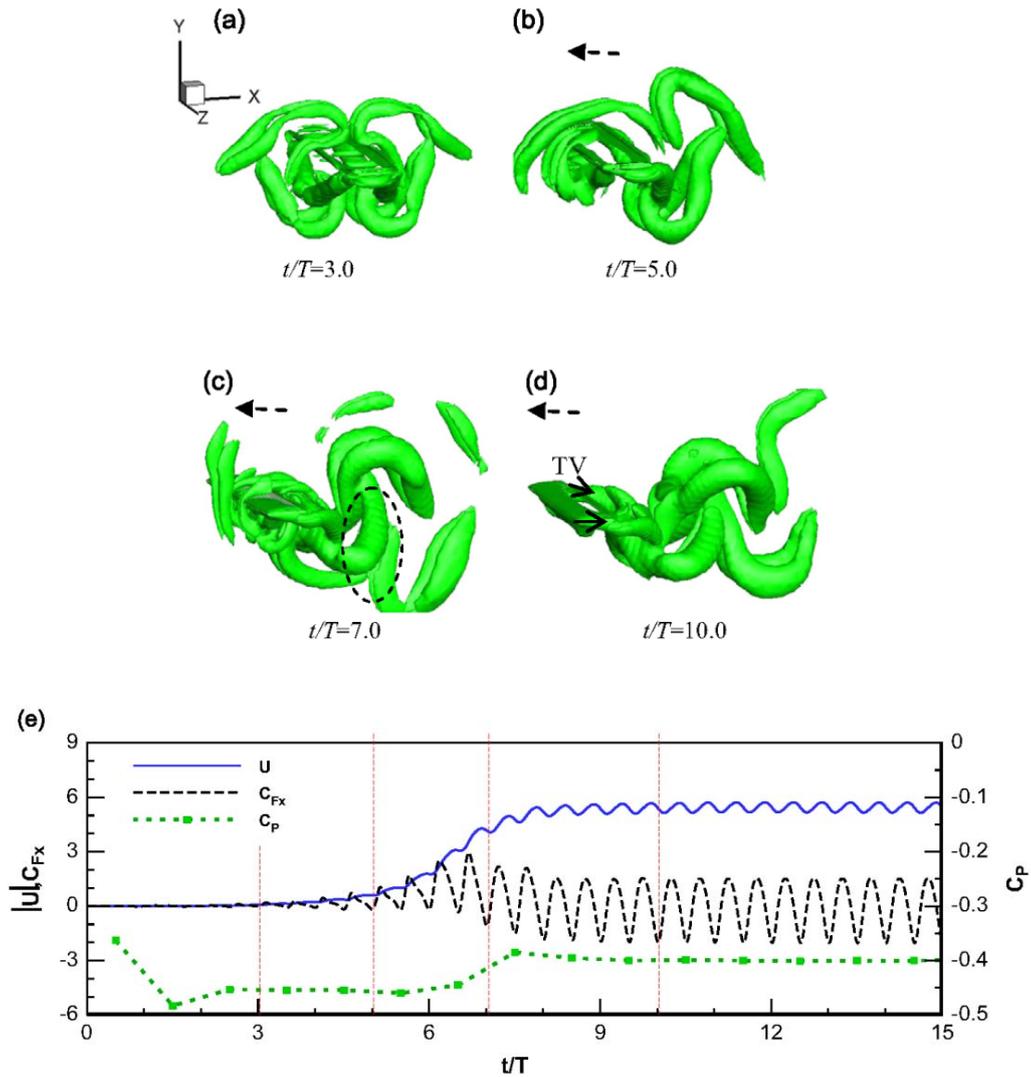
Figure 3.8 Evolution process for a symmetric wing with AR=4.0, Re$_{fi}$=80, σ=4.0. (a) (b) (c) (d) vortex topology at four instants; (e) instantaneous horizontal velocity, fluid force and the cycle-averaged-input power coefficient.

The evolution process develops similarly but the quantities of final velocity, forces vary under different aspect ratios. Therefore, it is necessary to carry out a parametric study on understanding the three-dimensional mechanisms.

3.4.2　Aspect Ratio Effect

In this section, we further present the effect of aspect ratio on the translational locomotion ability. Horizontal velocity variation of wings with different aspect ratio (AR) is plotted in Figure 3.9, where evolution has reached a steady status. It indicates that wings with bigger aspect ratios can induce faster velocities. The investigation by variation of horizontal fluid force coefficient (Figure 3.10) tells that there is a significant increase in the amplitude of thrust coefficient for wings with bigger aspect ratios. A similar phenomenon observed on U and C_{Fx} curves is that they both oscillate at the same frequency as the prescribed plunging motion. Referred to Eq. (3.2), translational velocity u_b is a function of translational force. Therefore stronger forces can lead to faster velocities, which is consistent with the trend of velocity and force curves in Figure 3.9 and Figure 3.10.
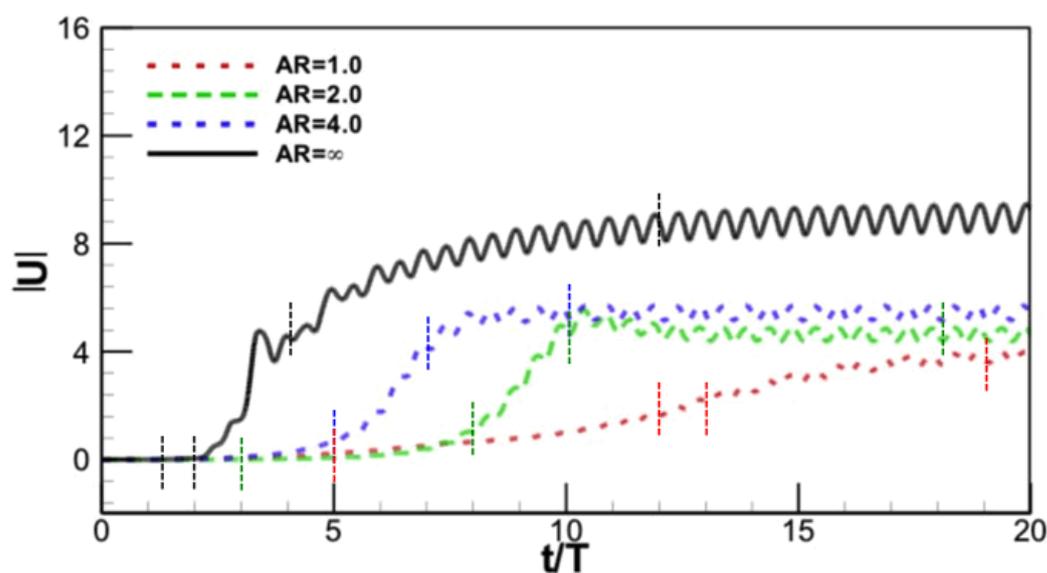
Figure 3.9 Time variation of instantaneous horizontal velocity for wings with AR=1.0, 2.0, 4.0 and ∞, Re_{fr}=80, σ=4.0 (Dashed lines present time instants selected for vortex toplotogy plots correlating to different evolution stage in Figure 3.7, 3.8, 3.11 and 3.12).

Instant wake topology of wings with AR=2.0 and 1.0 is presented in Figure 3.11 and Figure 3.12, along with Figure 3.7 and Figure 3.8 with AR=∞ and 4.0, indicating a flow structure variation under different aspect ratios. During the evolution, there occurs similar phenomenon, that all wake patterns go through four stages, left-right

symmetry pattern, symmetry breakdown process, forming vortex dipoles (as dashed circle lines), and achieving quasi-steady locomotion status. In the figures, the wake topology plot at each time instant presents a specific evolution stage, and different time instants are selected for wings with different AR due to the diverse evolution duration. As they are all under the same flapping motion ($Re_{fr}=80$ and $A/c=0.5$), the rings in each set have the same direction of rotation and the oblique angles are similar. However, wings exhibit qualitative differences under different AR. The three-dimensional rings are formed by tip-vortices (TV, as solid arrow marked in the figures) released from the span-wise tips. Wings with short aspect ratios of AR=1.0 and 2.0 produce circular vortex rings, as the TV are close to each other along a short aspect distance. The tip-vortices of wings with AR=4.0 merge with each other with a longer distance, and result in the vortex shape being stretched thinner, forming elongated loops. The elongated loops are beneficial to facilitating a faster traveling speed and generating stronger jet flow than circular vortex rings due to a less power loss at the mid-span region. The different aspect ratios of wings lead various vortex structures and thus affect thrust force and induced velocity.
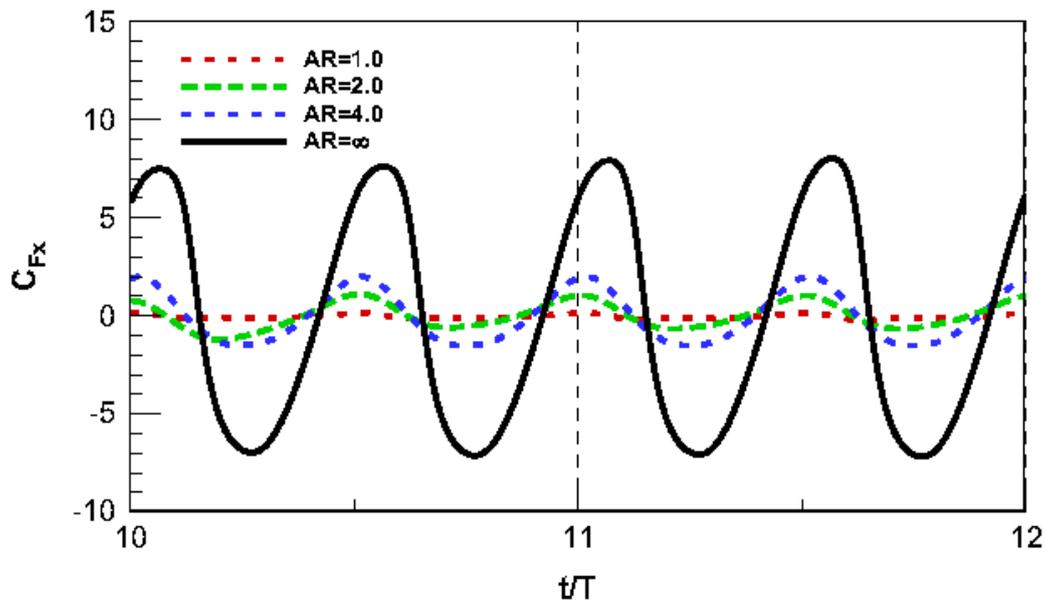
Figure 3.10 Time variation of instantaneous horizontal fluid force coefficient for wings with AR=1.0, 2.0, 4.0 and ∞, $Re_{fr}=80$, $\sigma=4.0$
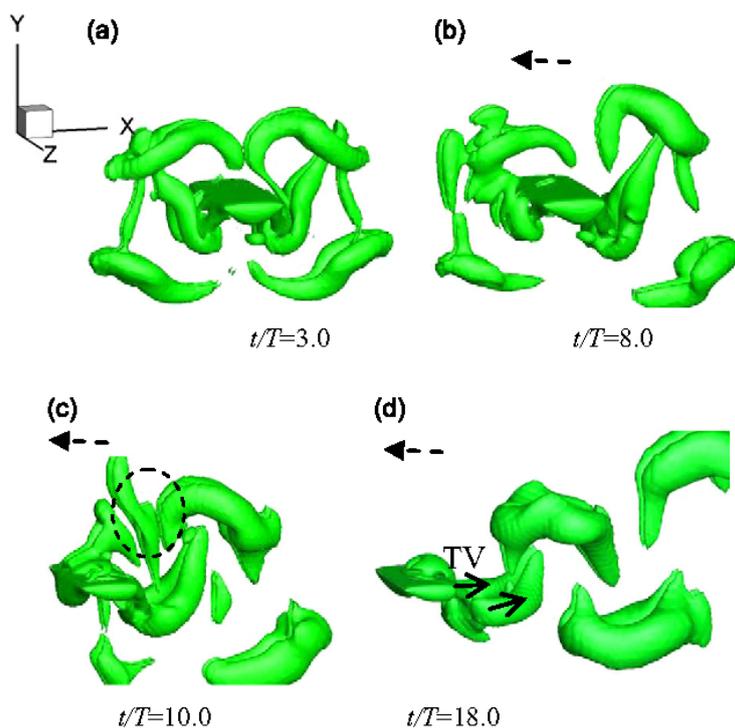
Figure 3.11 Vortex topology at four instants for the wing with AR=2.0, Re$_{fi}$=80, σ=4.0.
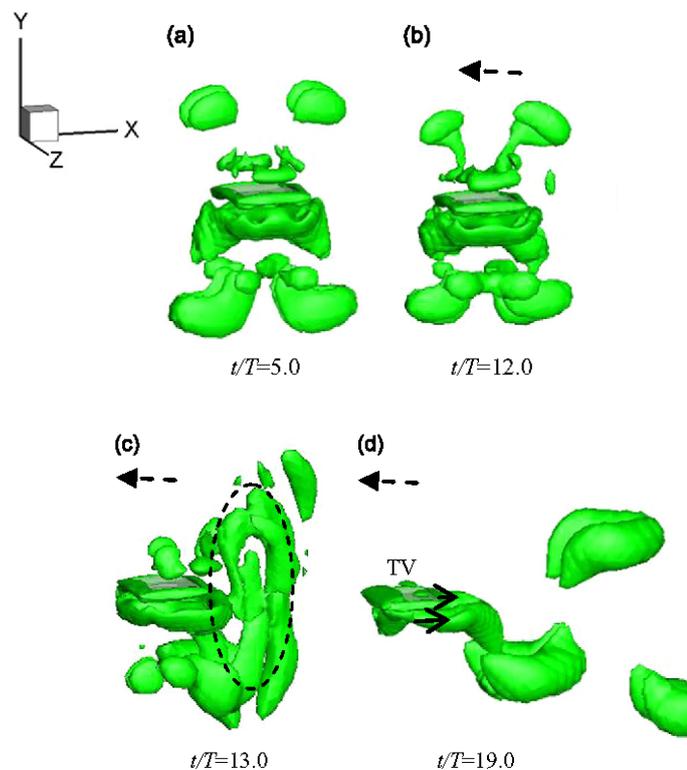
Figure 3.12 Vortex topology at four instants for the wing with AR=1.0, Re$_{fi}$=80, σ=4.0.

The relationship between the averaged translational Reynolds number (Re_u) (corresponding to frequency Reynolds number (Re_{fr})) and aspect ratio (AR) is presented in Figure 3.13 for a fixed σ=4.0. Firstly, for all cases, the Re_u increases monotonically with Re_{fr}. Such behavior is well documented in the previous studies for two-dimensional self-propelled flapping foils (Alben and Shelley, 2005; Benkherouf et al., 2011; Dong et al., 2006; Lu and Liao, 2006). Secondly, Re_u turns into a linear function of Re_{fr} when Re_{fr} is over a critical value, ranging from 40-60 in the current study, which agrees well with the study of Vandenberghe et al. (2004). Furthermore, induced velocity becomes larger as the aspect ratio increases at fixed Re_{fr}. Wing with small aspect ratio (AR=0.5) wanders very slowly, but the speed rises dramatically when aspect ratio is bigger than 1.0.

The present simulations also indicate that low-aspect-ratio wings lead to the same *St* number as large-aspect-ratio ones under stronger flapping frequencies. Besides, the *St* number mostly appears within the interval 0.2-0.5. This is an interval within which flying and swimming animal, driven by wing or tail, are likely to achieve and maintain high propulsive efficiency. Faster speeds can be achieved, considering the hydrodynamic performances alone, by wings with larger aspect ratio. However, if applied to animals, penalties can be incurred by the wings for large aspect ratios, for example, the need to hold bending moments from stronger and heavier body structures. Dong et al. (2006) show that most fish pectoral fins are found to have an aspect ratio somewhere between 2.0 and 3.0, within which the wings usually travel faster under a potentially high propulsive efficiency.

3.4.3   Density Ratio Effect

According to the previous study on two-dimensional foils, self-propelled foil evolution motion and velocity magnitude are dependent on mass ratio σ. There is a critical density ratio, over which foil achieves a steady net movement in one direction rather than undergoes a spontaneous forward and backward motion (Alben and Shelley, 2005; Lu and Liao, 2006). In the present study, the focus is on the induced translational velocity eventually in steady status, thus relatively large mass ratios are selected as 4, 20 and 32.
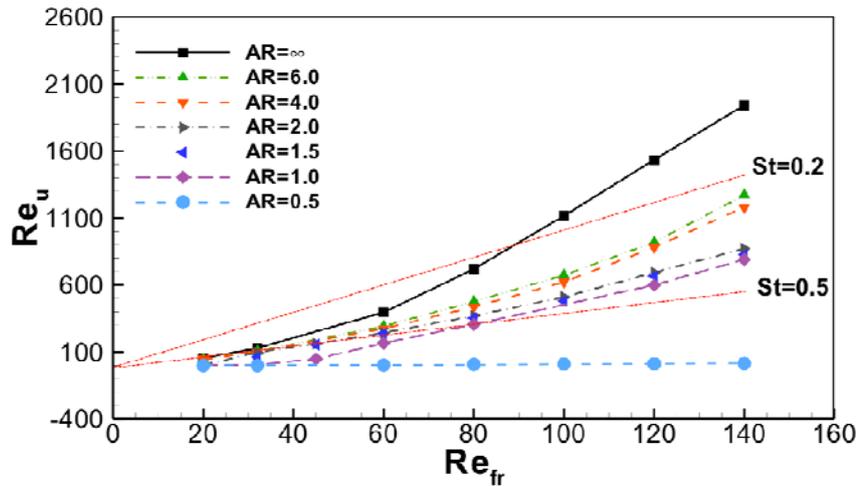
Figure 3.13 Averaged translational Reynolds number (Re_u) against frequency Reynolds number (Re_{fr}) under various AR with dashed red lines marking with St number range.

The evolution of the instantaneous Re_u is shown in Figure 3.14 (a) with Re_{fr}=60. As seen, wings reach a similar final average velocity after initial evolution cycles. The ones with large mass ratio take more cycles to achieve the quasi-steady velocity, and have smaller fluctuations. This shows that the heavy wings are not as sensitive to the surrounding instantaneous fluid as light wings. In the stability aspect, the heavy ones are more stable. However they are less flexible in terms of their manoeuvrability.

More tests were carried out on wings with various density ratio and aspect ratios. Results in Figure 3.14 show that the horizontal speed stays constant within little deviation, and similar observation hold for those wings with either big or small aspect ratios. The dynamics of aquatic animals involves a complicated interaction of their bodies with the surrounding fluid flow. Usually, the flapping mode can naturally stay in the regime of a steady movement state to generate a forward flapping locomotion.
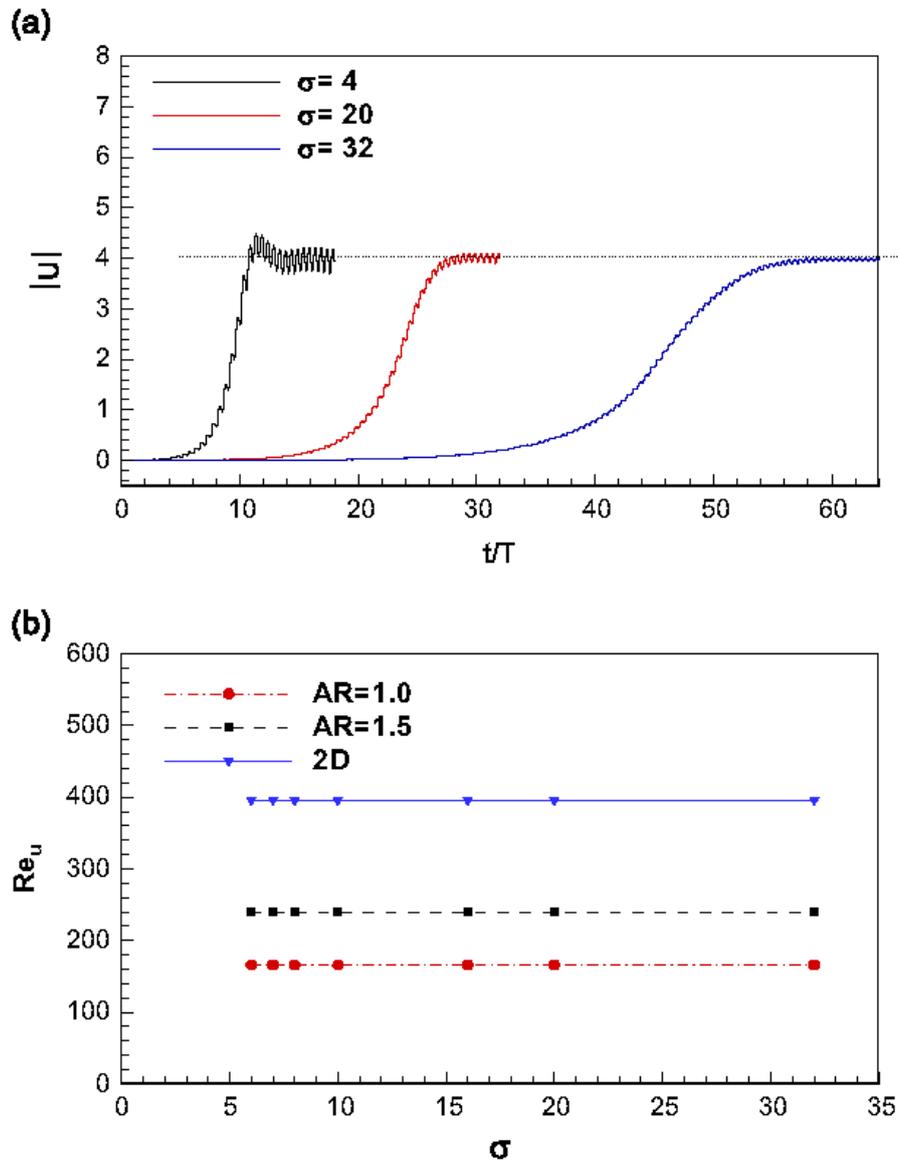
Figure 3.14 (a) Variation of the instantaneous translational velocity U, AR=1.5; (b)Translational Reynolds number Re_u with different density ratio σ. (Re_{fr}=60)

3.4.4 Perturbation Effect

As described in Sec. 3.4.1, the symmetric foil and wing can travel horizontally with unidirectional locomotion, in either left or right with equal probability. During the evolution process, the initial perturbation plays an essential role on determining the way in the transition period. It is interesting to examine how the self-propelled

phenomenon is influenced by initial flow conditions. In the present study, the effects of mesh symmetry and imposed perturbation velocities are examined respectively.

The induced moving directions of selected wings under different AR and Re_{fr} are summarized in Table 3.2. It indicates that the wings with same aspect ratio are likely to be moving in the same direction, regardless of Re_{fr}, except the wing with AR of 1.5. Even though the grid asymmetry is carefully avoided when we generate meshes, there are still slight differences between wings left and right over the whole computational domain and it may lead to a small perturbation and stimulate symmetric breakdown. The results shown in Table 3.2 could be attributed to the fact that the mesh is the same with an identical aspect ratio that results in the same direction. A special case is the wing with AR of 1.5 for which the induced travelling direction changes with increasing Re_{fr}, indicating that perturbation can also be induced by the asymmetric vortex shedding coming along with dynamic motion effect and aspect length effect. It indicates that there are factors inducing initial perturbation, such as asymmetric mesh, dynamic motion effect and leading/trailing edges and wing end effect. A guess is made that there should exists a criterion condition about the dominating term among the factors that induce most initial perturbation, but we are not able to make a further investigation due to the limited results obtained in the present study.

Table 3.2 Directions of induced velocities. <+> represents wing travels in positive *x* direction, and <-> represents wing travels in negative *x* direction.

Re_{fr}/AR	∞	0.5	1	1.5	2	4	6
80	-	-	+	+	-	+	+
60	-	-	+	+	-	+	+
45			+	-	-		
32	-	-	+	-	-	+	+
20	-	+	+	-	-	+	+
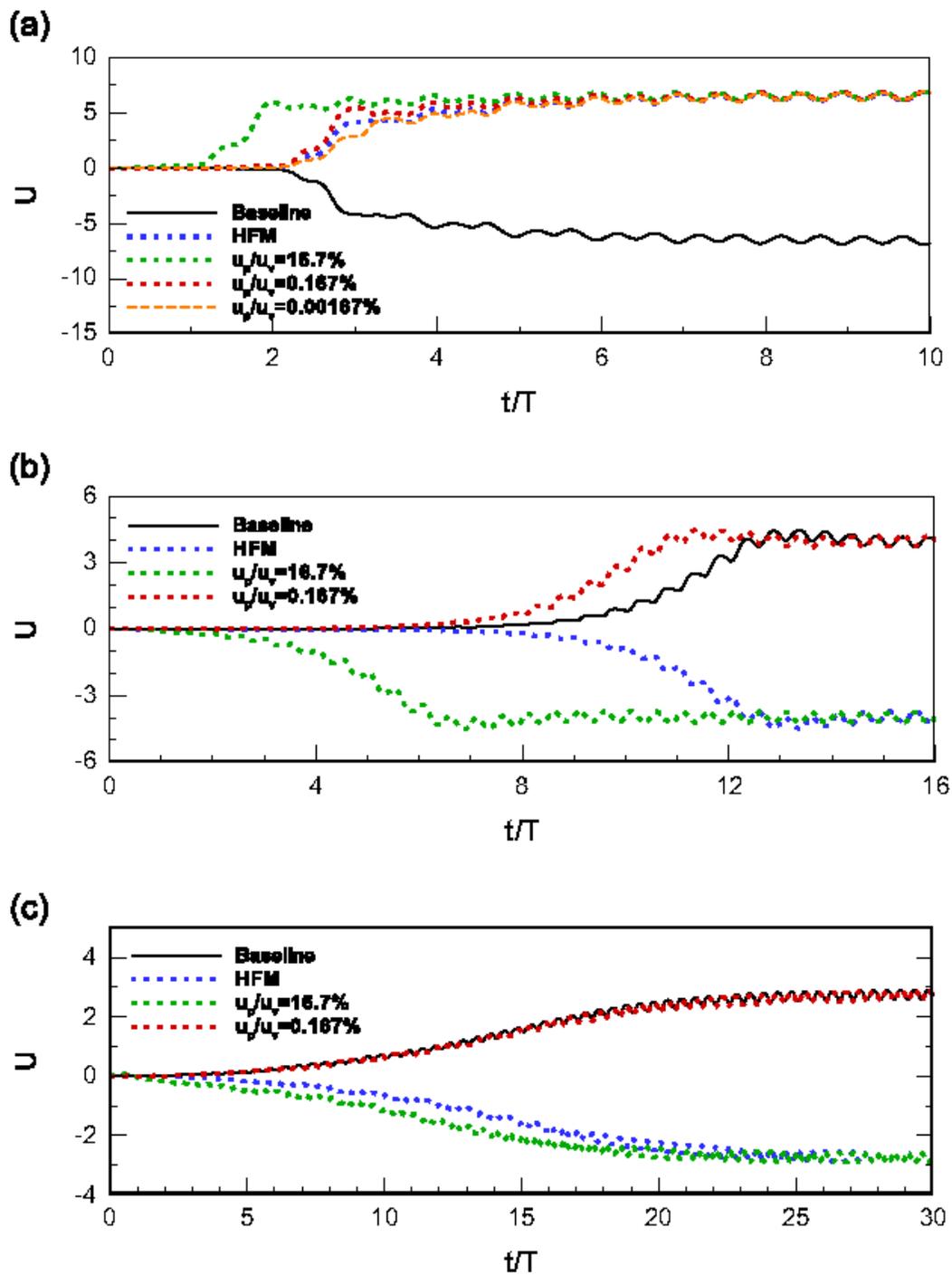
Figure 3.15 Initial pertubation effect on movement directions of flapping wings, by testing horizontally flipped mesh (HFM) and various perturbation velocities (u_p) with (a)AR= ∞; (b)AR= 1.5; (c)AR=1.0, (Re_{fr}=60).

Three cases with AR = ∞, 1.5 and 1.0 are selected by simply swapping the left and right mesh domain, and the time evolutions of wing velocity are shown in Figure 3.15. Obviously, the translational velocities are just opposite with the horizontally flipped mesh line (HFM) compared to the baseline, showing that the moving direction is sensitive to the initial mesh conditions.

Motivated by the methodology on the symmetry breaking of circular cylinder's wake vortices (Tang and Aubry, 1997), and dynamic stability analysis of flying animal (Gao et al., 2011), the induced motion is studied by the imposition of an initial perturbation. In order to do this, small specified perturbation velocities (u_p) are imposed on the selected wings as an initial condition of velocity. The u_p is specified with an opposite direction as those without perturbation velocity cases (baseline cases), and various velocity magnitudes, with u_p= 0.00167%, 0.167% and 16.7% of the vertical angular velocity ($u_v=2\pi hc/\omega$) respectively. The results of the instantaneous velocity evolution process are shown in Figure 3.15. It can be seen that the effect of u_p on wings with different AR shows a non-linear stability. There exists smaller u_p (u_p/u_v=0.167%) which is not strong enough to alter the horizontally moving direction as for cases with AR=1.0 and 1.5, and the bigger one (u_p/u_v=16.7%) which is able to change the travelling direction for all these three cases. The imposed perturbation affects the wing moving direction as well as the initial development time to reach the final quasi-steady status.

Generally, it can be seen that the perturbation has no effect on final quasi-steady velocity amplitude, but clearly has some effect on travelling direction and evolution process. To explain this phenomenon, it is deemed that the perturbation effects are mainly valid at the beginning of the transition period. Since the initial fluid flow is quiescent, and there is no horizontal constraint, the symmetric foil/wing is highly sensitive to the surrounding environment. Thus, small perturbation is able to lead to locomotion [as the status in Figure 3.7 (b) and Figure 3.8 (b)]. The small perturbation is caused by leading/trailing edge vortex shedding as well as wing end-effect related to span-wise length. However, after vortex collision [status in Figure 3.7 (c) and Figure 3.8 (c)], relatively stronger hydrodynamic forces are produced, hence those very small perturbations can be negligible, and would not change the velocity in the final quasi-steady status. This perturbation phenomenon influence may also be

explained by a passive mechanism Flapping Counter Torque (FCT) (Faruque and Humbert, 2010a, b; Hedrick et al., 2009), and Flapping Counter Force (FCF) (Cheng et al., 2010). They suggested that symmetric flapping wings produced restoring torque and force making swimmers respond to perturbation by decreasing body rotation, and could maintain flight stability by a passive damping coefficient. Therefore, the periodic plunging motion in the current study is able to maintain a stable locomotion status after slightly initial perturbation.

Chapter 4 Flapping Wing with Translational and Rotational Motion

4.1 Introduction

In the present numerical study, we perform a comprehensive investigation on the dynamic response of a 3D flapping wing with 2DoF in lateral and rotational directions under a zero-initial-velocity condition. The parametric study is made by considering the effects from various parameters, including not only those mentioned in the last chapter, i.e. wing AR, flapping frequency (Re_{fr}), density ratio (σ), but also those induced from the passive pitching motion of system, e.g. torsional stiffness, frequency ratio and pitch bias. The hydrodynamic performance of the 3D flapping wing is illustrated from the development of system symmetry breakdown, self-propelled velocity and efficiency, and related wake structure etc.

4.2 Mathematical Model

4.2.1 Two Degree-of-Freedom Flapping Wing Model

The numerical model is shown in Figure 4.1. Comparing with the model of last chapter, an additional rotational degree of freedom is taken into account. In particular, a specified sinusoidal plunging motion is imposed on the wing, which is defined as Eq. (3.1).
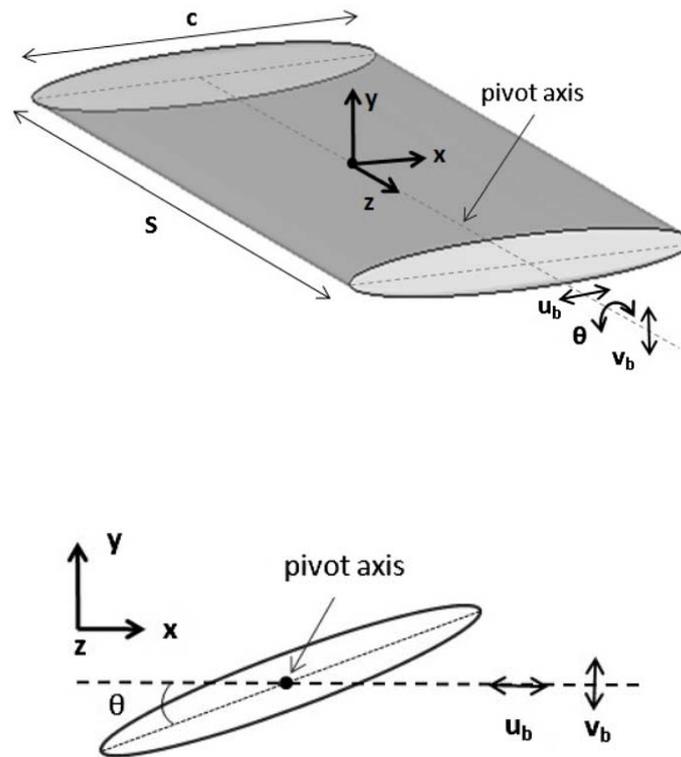
Figure 4.1 Sketch of the simulation model.

Beside the lateral hydrodynamics force acting on the foil, the hydrodynamics momentum accounting for the rotational motion of the wing, is also monitor in this study. The lateral motion of the wing is govened by the same equations show in last chapter, while the rotional motion is governed by a rotional momentum euqaiton as based on a tosional spring assumption:

$$I \frac{d^2\theta}{dt^2} + k\theta = M_z \qquad (4.1)$$

Where M_z is the fluid moment imposed on the wing, θ is the pitching angle, k is the spring stiffness, and I is the inertia moment of wing. The Runge-Kutta method is employed to solve the rotational equation as

$$\dot{\theta}_{t_{n+1}} = \dot{\theta}_{t_n} + \frac{\Delta t}{6} \cdot (K_1 + K_2 + 2K_3 + K_4) \qquad (4.2)$$

$$K_1 = \frac{M_z}{I} - \frac{k}{I} \cdot \theta_{t_n}$$

$$K_2 = \frac{M_z}{I} - \frac{k}{I} \cdot (\theta_{t_n} + \frac{\Delta t}{2} \cdot \dot{\theta}_{t_n})$$

$$K_3 = \frac{M_z}{I} - \frac{k}{I} \cdot (\theta_{t_n} + \frac{\Delta t}{2} \cdot \dot{\theta}_{t_n} + \frac{(\Delta t)^2}{2} \cdot K_1)$$

$$K_4 = \frac{M_z}{I} - \frac{k}{I} \cdot (\theta_{t_n} + \Delta t \cdot \dot{\theta}_{t_n} + \frac{(\Delta t)^2}{2} \cdot K_2),$$

(4.3)

where n represents the nth time step and $\theta_{t_{n+1}}$ and θ_{t_n} are the pitching angles at the instantaneous time of $(n+1)\Delta t$ and $n\Delta t$.

4.2.2 Fluid Solver

The flow filed around the flapping wing is simulated using the commercial CFD package FLUENT version 13.0 with and unsteady incompressible solver. A second-order upwind spatial discretization and first-order time discretization is used. In addition, to reduce the inaccuracy generated by the mesh deforming and re-meshing process, the entire domain is handled as a rigid moving body without relative motion between the body and its surrounding mesh. The body's plunging motion (v_b) is imposed on the domain using Dynamic Mesh Function in FLUENT. The parallel processing setup is established through High Performance Computer

In our studies, the characteristic Reynolds number is calculated by the velocity between the wing and the fluid. It ranges from 0 to 1000, and hence, the flow field is assumed to be laminar. At each time step, the simulation starts with attaining the flow field around wing by solving unsteady continuity and momentum equations associated with the Dirichlet and Neumann boundary conditions of velocity and pressure. By obtaining the flow data, the integrated wing surface forces and moment acting on the wing body are available. The dynamic response of wing is therefore obtained by solving Eqs. (4.1) and (4.2) where the system structural parameters, such as the wing mass, stiffness are taken into account.

4.2.3　Parameter Selection

The dynamic and non-dimensional parameters used in this chapter are similar to those in the last chapter. Additional parameter employed in this chapter is the frequency ratio, which is defined as

$$F = \frac{f_n}{f},$$

(4.4)

where f_n is the wing natural frequency, and defined as

$$f_n = \frac{1}{2\pi}\sqrt{\frac{k}{I}},$$

(4.5)

where k and I are the stiffness of system and moment of inertia of the wing, respectively. The non-dimensional density ratio (σ) indicates the wing system inertia, and the frequency ratio (F) represents the rotational stiffness.

Meanwhile, the computed data are summarized with the induced lateral non-dimensional velocity (Re_u) and the pitching angle (θ_{rms}) based on its Root Mean Square value (rms), which is defined as

$$\theta_{rms} = \sqrt{\frac{\sum_{r=1}^{i}(\theta^{t_r} - \theta_{avg})^2}{i}}.$$

(4.6)

The i in Eq. (4.6) represents the iteration time step, θ^{t_r} is the pitching angle at the r^{st} instantaneous time, θ_{avg} is the averaged pitching angle.

The vertical overall force coefficient:

$$C_{F_y} = \frac{F_y(t)}{\frac{1}{2}\rho\left(f(hc)\right)^2 cL}.$$

(4.7)

The pressure force coefficient:

$$C_{F_{Px}} = \frac{F_{Px}(t)}{\frac{1}{2}\rho\left(f(hc)\right)^2 cL}.$$

(4.8)

The propulsion efficiency η is defined as:

$$\eta = \frac{\int_t^{t+T} u_b(t) F_{P_x}(t)\, dt}{\int_t^{t+T} v_b(t) F_y(t)\, dt},$$

(4.9)

where F_y are the force components in vertical direction, F_{P_x} is pressure force in the lateral direction.

The parameter ranges studied in this chapter are summarized in Table 4.1. Both the two-dimensional foil (AR = ∞) and the three-dimensional wing with low aspect ratio (AR ≤ 4.0) are investigated. The frequency ratio (F) is mainly selected between 1.5 to 10.0 to control the wing dynamic response in rotational direction. Obviously, wing with F equal to infinity is the indication of one DoF in lateral (x) direction. The density ratio examined here is in-between 4.0 to 32, which is usually applied in marine models in previous studies (Alben and Shelley, 2005; Lu and Liao, 2006) and also the focus of present study. As compared to the relevant mass ratios for live flying birds or insects, such as the wings of hawkmoths, bumble bees and frutiflies, which are reported to be of 2.0×10^3, 2.1×10^3 and 1.1×10^3, respectively (Buchwald and Dudley, 2010; Combes and Daniel, 2003a, b; Willmott and Ellington, 1997a, b), the mass ratios for aquatic animals are relatively small.

Table 4.1 Various parameters investigated in the present study.

Density ratio σ	Plunging amplitude (h)	Flapping Re (Re$_{fr}$)	Frequency ratio (F)	Aspect ratio (AR)	Pitching axis position (x/c)
4-10, 16	0.5	80	1.5-10	1.0, 1.5, 2.0, 3.0, 4.0	0
4-10, 16	0.5	80	1.5-10	∞	0, 0.1, 0.2, 0.3, 0.4, 0.5
4, 20, 32	0.5	20, 32, 45, 60, 80	∞	1.0, 1.5, 2.0, 4.0, 6.0, ∞	-

In addition, the flapping Reynolds number Re_{fr} for the 3D wing in the present study, is fixed at 80, which is comparatively small as compared to the normal flapping wing cases in biological flights. However, since the main objective of the present study aims at unveiling the three-dimensional mechanisms in free-moving 3D wings with a specific focus on the phenomenon "symmetry breakdown" and its subsequent development into stable states, the parameters selected are consistent with last chapter as well as those in relevant papers on a free-moving 2D foils by Alben and Shelley (2005) and a flat plate by Zhang et al. (2010) with Re_{fr}=0-50 and Re_{fr}=0-80, respectively.

Pitching axis of the wing is initially set at the center of chord (x/c=0 in Figure 4.1) to hold the wing left/right and clockwise/counter clockwise symmetry before the bifurcation starts. This is different from the real flyers, where the rotational axis are normally at the leading edge (Sane and Dickinson, 2002). As we will show later, the stiffness of wing, represented by frequency ratio F, on the induced lateral speed (Re_u) is remarkably affected by the pivot point. Thus, in the following sections, a systematic study is also performed on the pitching axis effect by varying the pivot point from leading edge (x/c=0.5) to center-chord (x/c=0).

Table 4.2 Summary on mesh size, time-step size and computing time.

Mesh	Overall cells	Nodes (wing surface)	Nodes (span-wise)	Time-step size	Simulation time (8 processors)	u_b/fc
AR1.5-C	1853675	200	80	T/200	59 hours	4.37
AR1.5-M	2782250	300	80	T/200	75 hours	3.95
AR1.5-F	6327830	400	120	T/200	153 hours	3.91
AR1.5-MST	2782250	300	80	T/150	62 hours	4.24
AR1.5-MBT	2782250	300	80	T/400	140 hours	3.96

(C- course mesh; M- medium mesh; F- fine mesh; MST- medium mesh & smaller time-step size;

MBT- medium mesh & bigger time-step size)

4.3 Numerical Validation

Based on the validation studies in last chapter, we conduct addition validation work in this chapter with special emphasize on the sensitivities of grid size and time-step size. Here, it is conducted for a 3D wing with AR of 1.5 under Re_{fi}=60, $F=\infty$ and h/c=0.5 conditions. The computational domain size is exactly same as shown in Figure 3.2, which is big enough to capture the flow development around and downstream of the flapping wing model. Details of overall volume and surface mesh numbers and time step are listed in Table 4.2, along with the computed averaged force coefficient C_{Fx}. Comparing the cases for mesh density test by AR1.5-C, AR1.5-M and AR1.5-F, the force coefficient from medium mesh is close to the one from fine mesh under a medium time-step size. And the cases for different time-step sizes test by AR1.5-M, AR1.5-MST, AR1.5-MBT present that time-step size of T/200 behaves similar as time-step size of T/400. The instantaneous C_{Fx} on the medium and fine grids (not shown here) indicate that the results on the medium grid with a time-step size of $dt=T$/200 almost coincide with those on the fine grid and $dt=T$/400. Considering an increased computing time as listed in Table 4.2, the time-step size $dt=T$/200 and medium mesh is used in the present simulation.

The numerical methodology developed for solving the problems with unsteady forced undulating swimming fish or two-dimensional flapping foil has been extensively validated in our previous publication (Hu et al., 2011; Xiao et al., 2011). To further validate the strategy utilized to handle the system dynamic response (fluid-structure-interaction) associated with the self-propelled feature, a validation on a self-propelled flat plate investigated by Zhang et al. (2010) is performed. Given the pre-specified plunging motion with a flapping Re_{fi}=40, amplitude A/c=0.5 and mass ratio σ_I=2.0, the computed propulsion velocity (u_b/fc) and pitching angle (θ) variation with frequency ratio are compared in Figure 4.2 with data from Zhang et al. (2010). The domain size for this 2D model is 21 and 11 times of chord length in in-line and transverse directions. There are 300 mesh cell numbers around the plate, and time-step size is selected as T/200. Our results present a general good agreement with theirs by capturing the peak u_b/fc and sharp varying of u_b/fc and θ versus F. The comparision on the time-dependent induced pitching angle at F=1.05 presents an excellent agreement between two results in terms of the amplitude and phase angle.

Apart from this test case, we also simulated a two-dimensional flapping elliptic foil that is studied previously by Alben and Shelley (2005). The comparison between our results and theirs are presented in the previous chapter in Figure 3.6 (a).

(a)

(b)

(c)
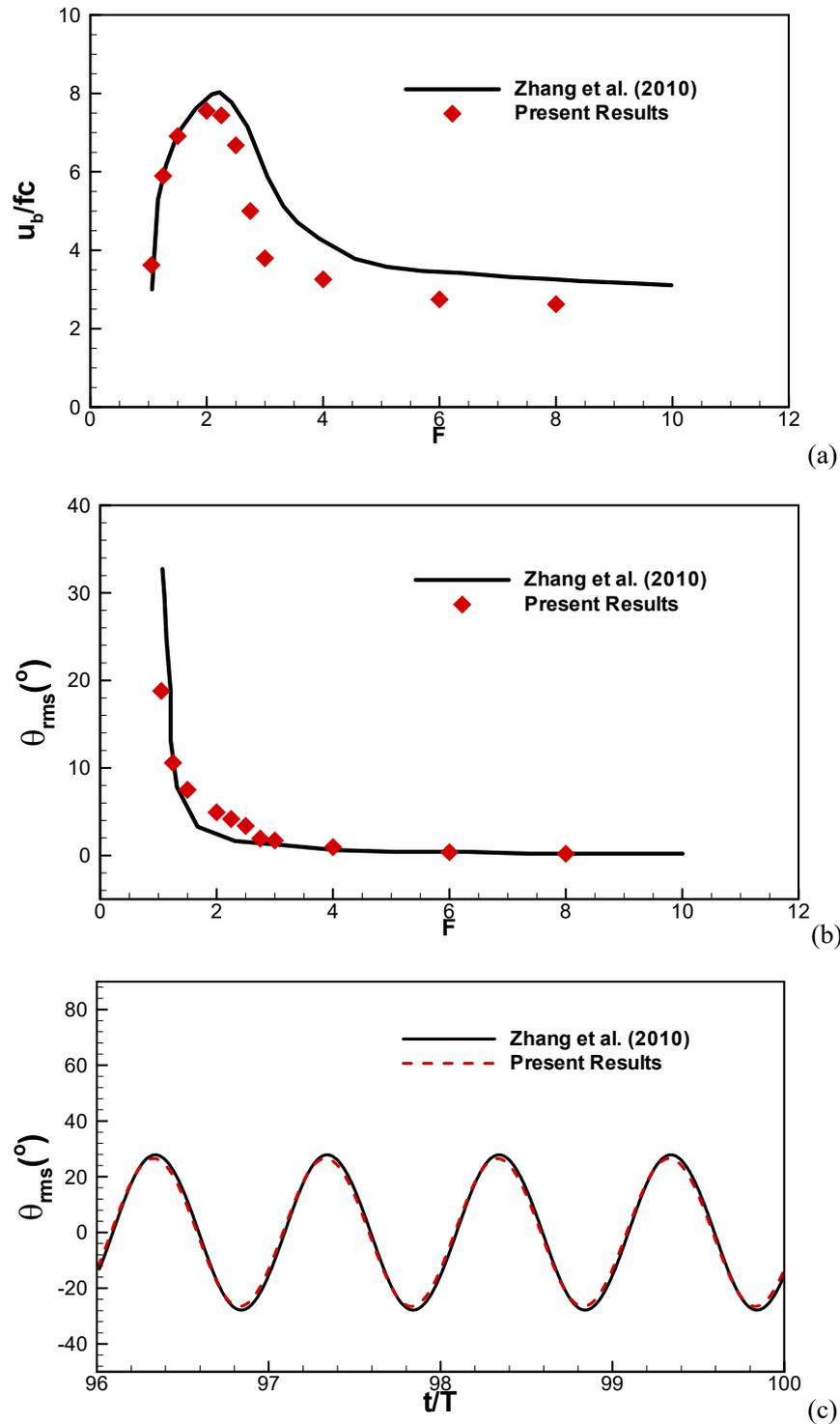
Figure 4.2 Comparison with Zhang et al. (2010) with 2DoF flat plate. (a) Induced non-dimensional lateral velocity. (b) Induced pitching angle. (c) Variation of induced instantaneous pitching angle at F=1.05.

4.4 Results and Discussion

In this section, our numerical results will be present and discussed in detail. Our attention will be firstly focused on the symmetric broken phenomenon of this system, which is slightly different as the wings with 1DoF in translational direction. As the plunging velocity increases, the system symmetric is broken, inducing a translational motion of the wing. As following, the flow status will be classified when the system reaches a steady state. After then, the effects of various parameters, which include aspect ratio, frequency ratio, pivot-point and density ratio, will be discussed in the last two sub-sections.

4.4.1   Phenomenon of Symmetry Breakdown

The observations on the evolution of wing heaving motion show that, given the forced Re_{fr} of 80, the wing under various grouping of aspect ratios, density ratios, frequency ratios and pitching bias distance could eventually reach a stable motion, a combination of an either forward or backward motion with a periodic pitching motion. The evolution of instantaneous $\tilde{Re}_u$ and θ are shown in Figure 4.3 and Figure 4.4, for two-dimensional foil (AR = ∞) and three-dimensional wing (AR = 2). It is clear that the wing starts its lateral movement almost at the same time when it rotational motion starts, indicating that once the pitching motion is activated, left/right symmetry breaks down and thus causes the lateral motion. Meanwhile, the three-dimensional wing takes longer developing time than a two-dimensional foil to reach its stable state.

To better understand the wing dynamic and the phenomenon of system symmetry breakdown, the vorticity contours at three typical time instants, i.e. symmetry, asymmetry development and fully developed state (denoted as t_1, t_2 and t_3, respectively) are shown in Figure 4.3 (a) and Figure 4.4 (a). The identification of three stages is from the observation of the induced lateral velocity evolution curves, as the velocity curves of wings roughly go through static zero velocity region, dramatically increasing region and quasi-steady region. The vorticity contour plots are

captured all the way along the fluid development, and the three time instants (t_1, t_2 and t_3) in Figure 4.3 and 4.4 are selected at the time instants when the most typical vortex structure can be captured. It can be clearly seen from the plots that, at time t_1, the flow field sustain a left/right symmetry structure, thus no movement of wing in lateral and rotational direction [Figure 4.3 (b-i) and Figure 4.4 (b-i) and (d-i)]. When the wing flaps more cycles and reaches time t_2, the pitching motion is activated as shown in Figure 4.3 (b-j) and Figure 4.4 (b-d-j) with an asymmetry vortex structure around the wing. At the fully developed state (t_3), a thrust-generating vortex wake is observed from Figure 4.3 (b-k) and Figure 4.4 (b-k) and (d-k). Comparison of Figure 4.4 (i) with Figure 4.4 (j) and Figure 4.4 (k) on the vortex structure around the wing at different span (z), reveals that the flow has a profound three-dimensional feature due to the low aspect ratio of wing (AR=2). A comparison between 3D wing symmetry plane vorticity contour plot with 2D wing in Figure 4.3 and Figure 4.4 also indicates a relatively weak vortex strength associated with 3D wing, implying a weaker propulsion feature wake structure. This is the key reason leading to a smaller Re_u and θ as compared to their 2D counterparts, and it will be shown in the follow sections in this chapter.

(a) Instantaneous $\tilde{Re}_u$ and θ.

(b-i) t_1=0.9T.   (b-j) t_2=2.3T.   (b-k) t_3=8.8T.
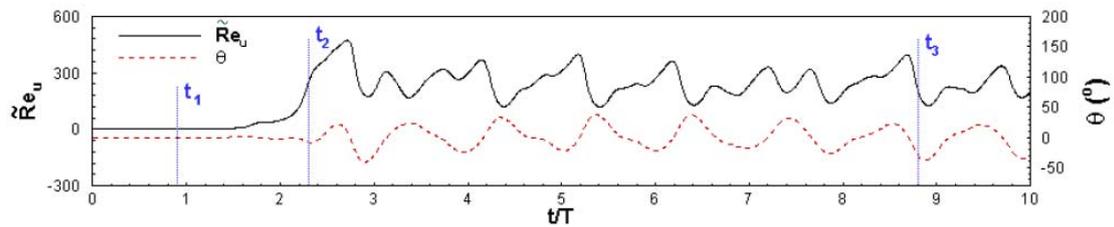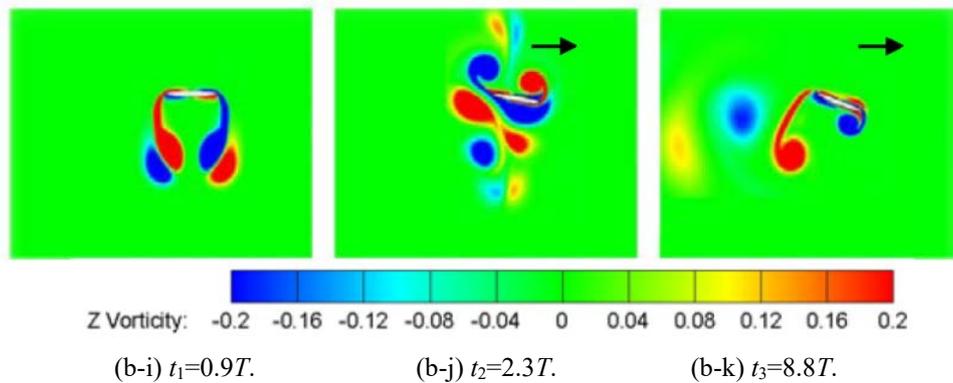
Figure 4.3 Evolution of symmetry breakdown (σ=8.0, Re_{fr}=80, F=2.0, AR=∞).

(a) Instantaneous $\tilde{\mathrm{Re}}_u$ and θ.

| z/S=0 | (b-i) t_1=0.9T | (b-j) t_2=4.9T | (b-k) t_3=9.9T |

| z/S=0.25 | (c-i) t_1=0.9T | (c-j) t_2=4.9T | (c-k) t_3=9.9T |

| z/S=0.5 | (d-i) t_1=0.9T | (d-j) t_2=4.9T | (d-k) t_3=9.9T |
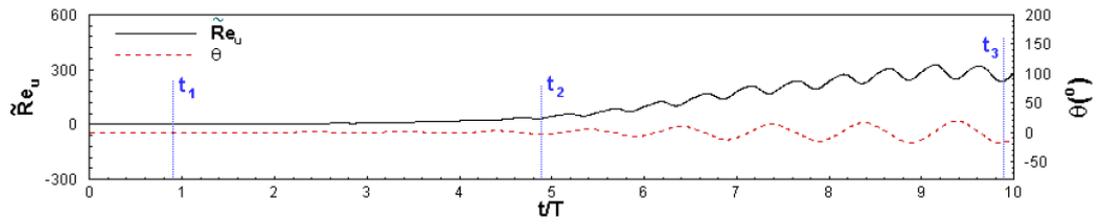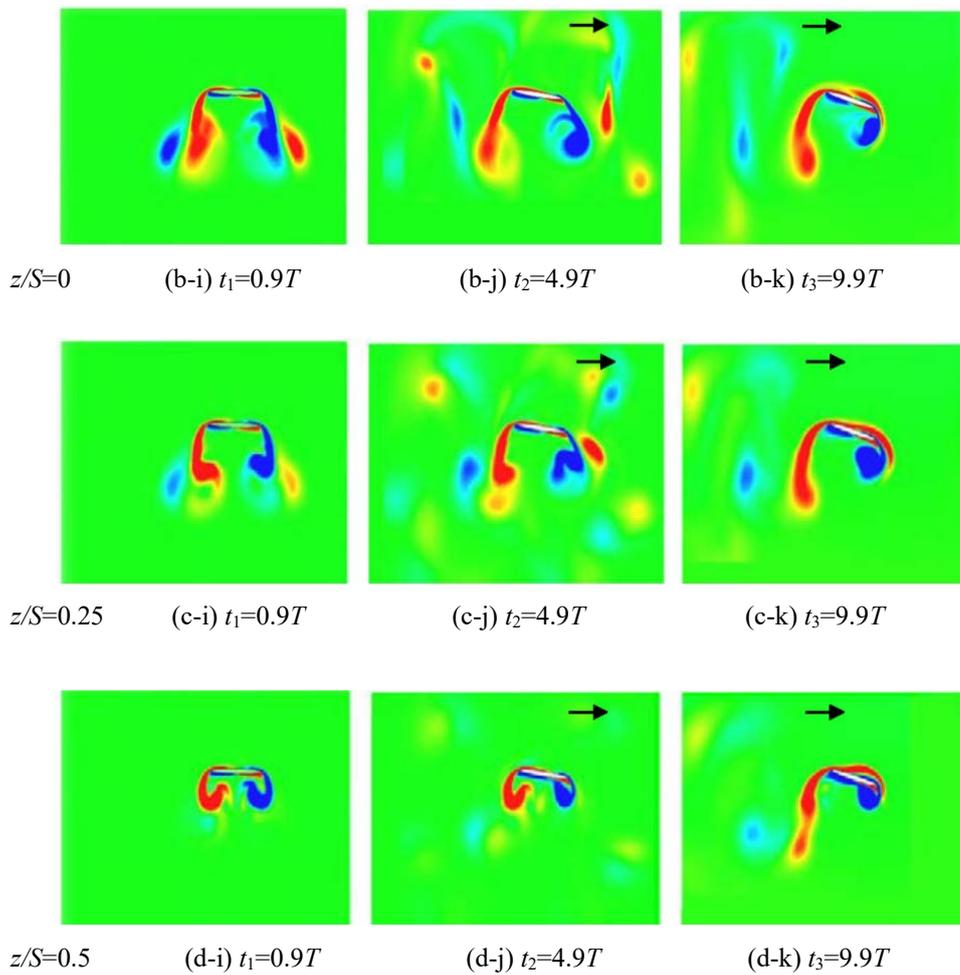
Figure 4.4 Evolution of symmetry breakdown (σ=8.0, Re_{fr}=80, F=2.0, AR=2.0). (The contour legend is same as in Figure 4.3)

4.4.2 Classification of Flow Status

Different flow status is classified in this parameter space of σ, F and $\tilde{Re}_u$. The results are summarized in Figure 4.5, obtained for the 2D wing and 3D wing (AR = 2.0) responses respectively. Each point in these plots represents a simulation data, which is collected after a periodic stable state, and different modes (Mode A, B-1, B-2) are classified by the frequencies of induced lateral velocity. Typical cases in different modes are selected for further investigation, under a range of frequency ratios varying from $F = 3.0$ to $F = 8.0$ with the same density ratio for both 2D wing and 3D wing. The corresponding time history on the instantaneous Re_u and θ, their Power Spectral Density (PSD) distribution, and vorticity topology contour are shown in Figure 4.6 and Figure 4.7.
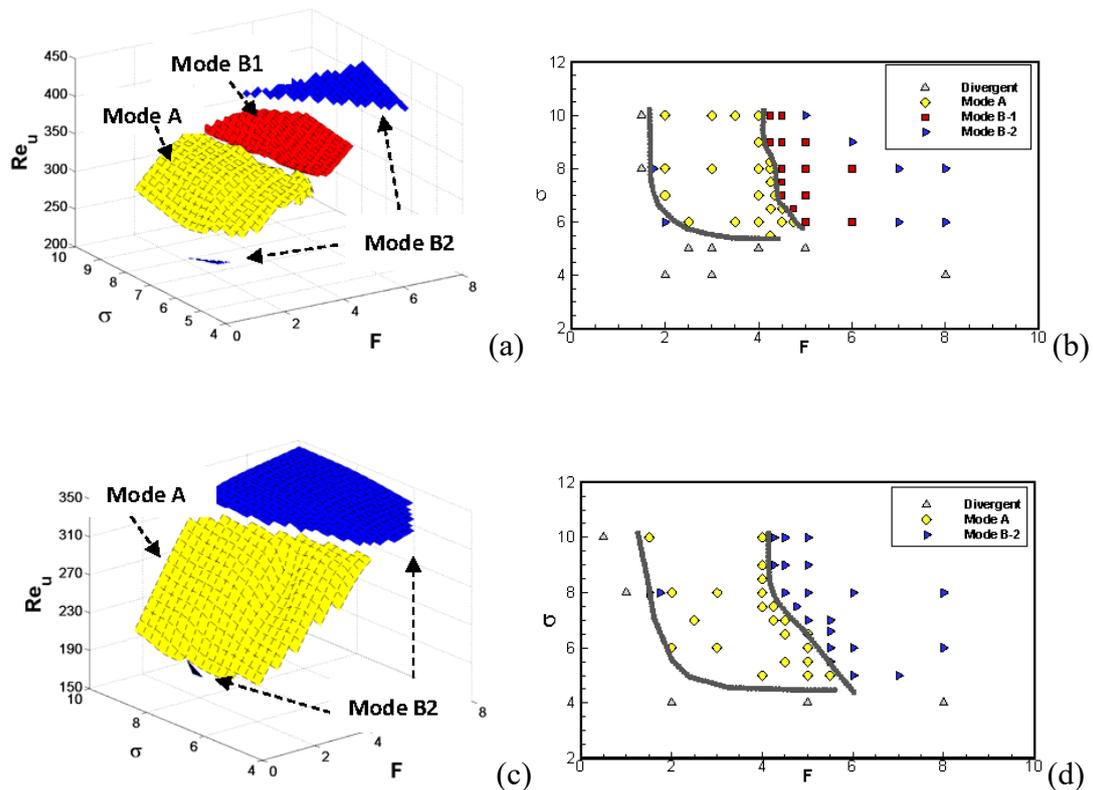
Figure 4.5 Boundary of various flow status (h/c=0.5, Re_{fr}=80). (a) Density-frequency ratio-Re_u 3D view (AR=∞). (b) Density-frequency ratio plane view (AR=∞). (c) Density-frequency ratio-Re_u 3D view (AR=2.0). (d) Density-frequency ratio plane view (AR=2.0).

(a-i) (a-j) (a-k)

(b-i) (b-j) (b-k)

(c-i) (c-j) (c-k)

(d)
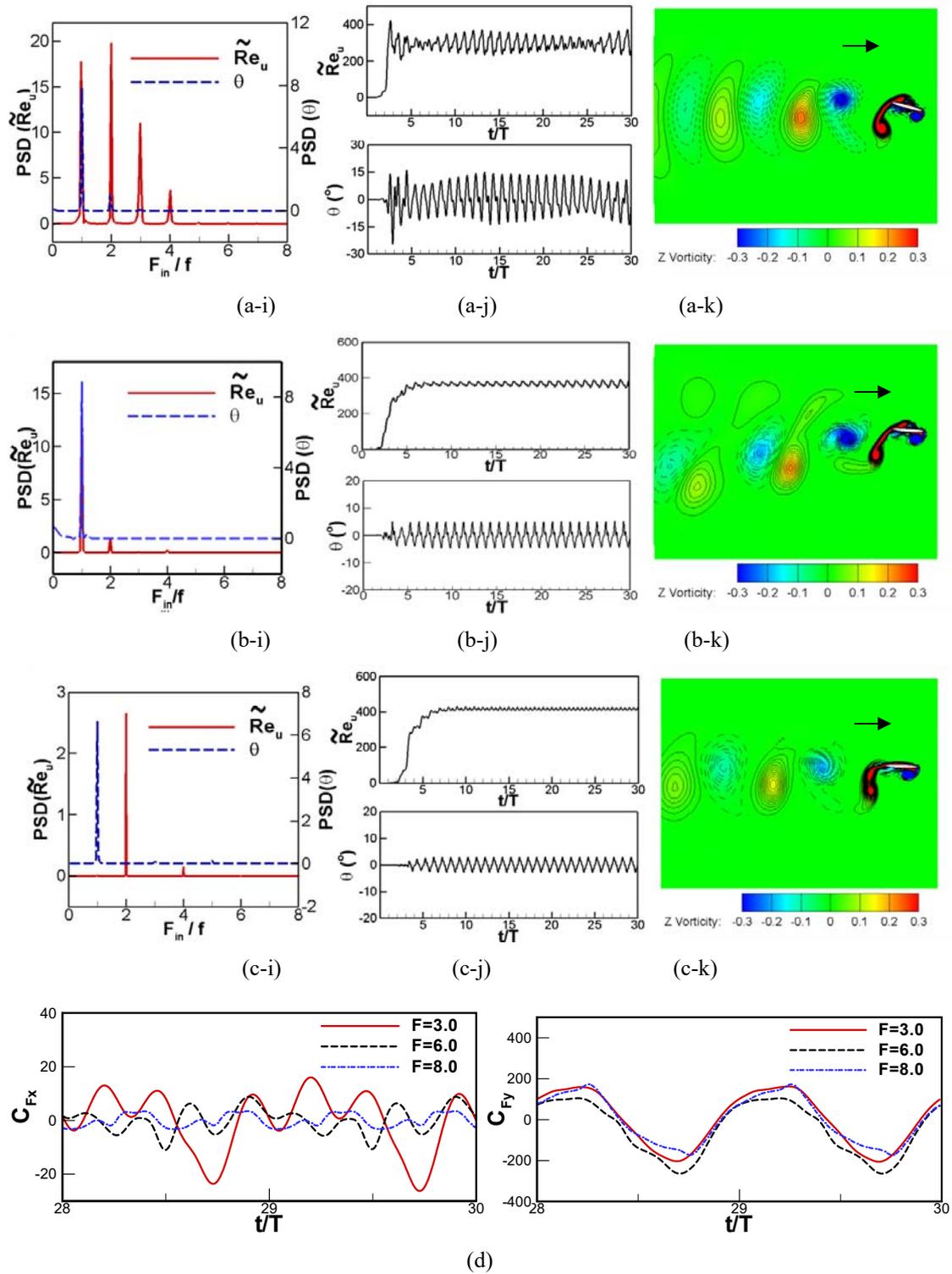
Figure 4.6 Evolution of instantaneous Re_{fr} and θ, their Power Spectral Density distribution (PSD), vorticity contour, and forces ($\sigma=8.0$, $h/c=0.5$, $Re_{fr}=80$ and $AR=\infty$). For vorticity contour, solid lines are positive values and dashed lines is negative value. (a) Mode A ($F=3.0$). (b) Mode B-1 ($F=6.0$). (c) Mode B-2 ($F=8.0$). (d) Instantaneous thrust and lift forces.

(a-i)　　　　　　　　(a-j)　　　　　　　　(a-k)

(b-i)　　　　　　　　(b-j)　　　　　　　　(b-k)

(c)
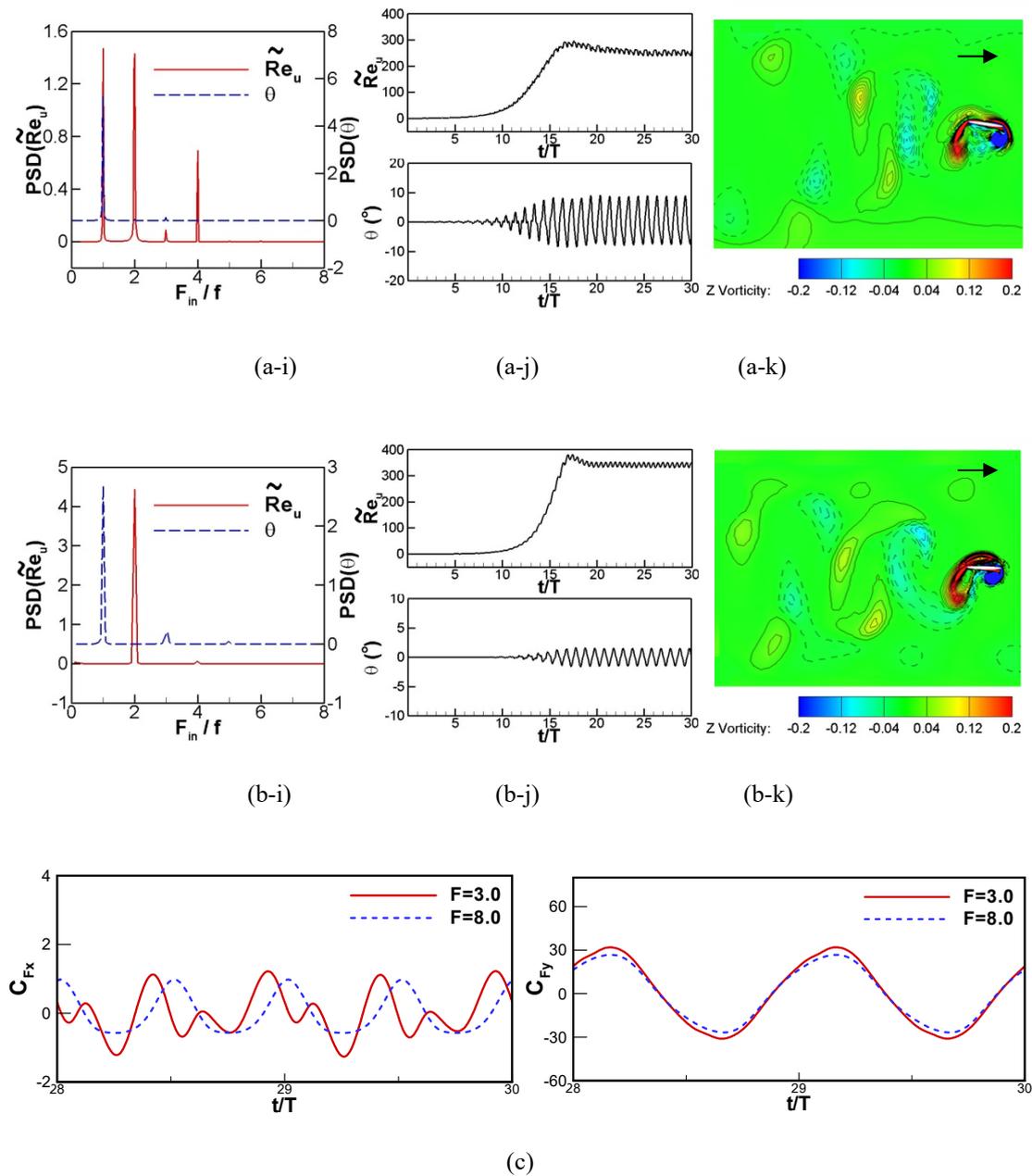
Figure 4.7 Evolution of instantaneous Re_{fr} and θ, their Power Spectral Density distribution, and vorticity contour ($\sigma=8.0$, $h=0.5$, $Re_{fi}=80$ and AR$=2.0$). For vorticity contour, solid lines are positive values and dashed lines is negative value. (a) Mode A ($F=3.0$). (b) Mode B-2 ($F=8$). (c) Instantaneous thrust and lift forces.

It is shown in these figures that the wing response in rotational direction (θ) to the forced flapping motion is generally more regular than the response in lateral direction. The Fast Fourier Transformation (FFT) analysis on the instantaneous θ plot, shown in

Figure 4.6 and Figure 4.7, dictate that one dominant frequency, i.e. a single spike is always observed for all cases studied, which is identical to the flapping frequency (F_{in}/f=1, where F_{in} is the induced lateral motion frequency and f is the prescribed plunging frequency). The FFT is calculated from 10th period to 30th period. For some 2D wing at a low frequency ratio where F is less than 4.5, a second spike or more is observable. This is consistent with our system dynamic feature where the stiffness is imposed merely in the rotational direction to manipulate the periodic pitching motion, as shown in Eq. (4.1). In contrast, the FFT on $\tilde{\mathrm{Re}}_u$ history, which represents the dynamic response in lateral direction, reveal a multiple-spike-frequency spectral distribution, where the dominant spike does not always correspond to the forced flapping frequency. Instead, it depends on a wide range of AR, density and frequency ratio investigated. The present results are only capable of providing evidences on the induction of multiple-spike-frequencies of lateral velocity, which is probably lead by the complicated vortex shedding procedure, but not quantifying the induction of these frequencies. In the following, we classify such complicated flow status based on the FFT analysis on $\tilde{\mathrm{Re}}_u$ into three-fold:

- **Frequency ratio**: with an increase in frequency ratio (F) or wing stiffness, the PSD for $\tilde{\mathrm{Re}}_u$ shows a gradual transition from a multiple-spike (2-3 modes) state to the single spike frequency state (1 mode). We denote the state exhibiting multiple-spike frequency as Mode A, and the state with single spike frequency as Mode B. Two subdivisions as Mode B-1 and B-2 are further defined corresponding to the F_n/f is equal to 1.0 or 2.0, respectively. It is found that the boundary between Mode A and B is affected by the system dynamics parameters, i.e. density and frequency ratio. Given a fixed density ratio, the wing with large F presents a more harmonic distribution in terms of $\tilde{\mathrm{Re}}_u$ vs. time plot, indicating the existence of one dominant frequency. This is also well reinforced by the instantaneous thrust and lift forces (C_{Fx} and C_{Fy}) plots in Figure 4.6 (d) and Figure 4.6 (c). Obviously, the lift force presents a rather regular one dominant frequency, which is irrelevant to the stiffness (F).

However, thrust force displays an increased multiple mode with small stiffness, which is believed to cause the multiple frequency in $\tilde{\text{Re}}_u$. From this point, the present results clearly reveal that, the torsional stiffness, represented by the spring added at pivot point, definitely plays its role in the overall wing dynamic response both in x and θ direction. With F approaching infinity, the pitching motion is fully eliminated, the wing becomes a rigid body with 1DoF in x direction, and thus it is expected to be more stable and regular under the external forced flapping motion. Indeed, we found that only one peak frequency exists in its PSD.

- **Aspect ratio**: The wing aspect ratio influences the boundary separating in Mode A and B slightly. Decreasing AR leads to the boundary moving to higher *F*. Apart from that, aspect ratio also changes the Mode transition and the ratio of $\tilde{\text{Re}}_u$ frequency relative to flapping frequency (F_n/f). Comparing 2D wing in Figure 4.5 (a-b) with 3D wing in Figure 4.5 (c-d), it is shown that, an increase in *F* causes a 3D wing transferring from Mode A directly to Mode B-2.

- **Density ratio**: Above trends are valid for all density ratios investigated. However, the exact boundary location is affected by density ratio (σ). In fact, decreasing density ratio causes the flow regime transition from Mode A to B at a relatively large frequency ratio (*F*).

Along with the key information provided by FFT analysis above, the typical vorticity topology contours at a given density ratio $\sigma = 8.0$ are shown in Figure 4.6 and Figure 4.7 to represent the relevant wake vorticity structure variation with a gradually increasing *F* from Mode A, B-1 to B-2. All vorticity plots shown in the figures are taken at the instantaneous time at which the wing pitches to the maximum angle. For a 3D wing, the vorticity contour is taken at wing half span section. It is shown that, the

vortical structure resembles the classic reverse von Kármán vortex street in the wake of a propulsive body, revealing the existence of a forward moving state. This behaviour is consistent with the experimental and numerical findings of a 2D foil in the work of previous studies (Alben and Shelley, 2005; Lu and Liao, 2006; Vandenberghe et al., 2006; Vandenberghe et al., 2004; Zhang et al., 2009). However, some differences do exist. For a small frequency ratio (F), a less stiff wing with the presence of Mode A, the pitching angle is relatively larger as compared to that of large F, where Mode B appears, the vortex shedding street becomes much wider, and more vortices sheds within one cycle, which leads to the co-existing of various PSD modes in the wake as shown previously. Increasing F causes the increasing of system stiffness and thus the wing pitching at a smaller angle. As a consequence, the wake becomes narrower and more regular, and fewer vortexes shed in one cycle as compared to the cases with small F. Though the above observation is generally true for both 2D and 3D wing, the detailed difference can be noticed from the 3D wing wake topology plotted using a Q-criterion theory as shown in Figure 4.8. At a low aspect ratio, like AR=2.0, a vortex ring forms via the combination of two tip vortex generating at the two ends of wing-span direction.

(To be continued.)

89

(a) (b)
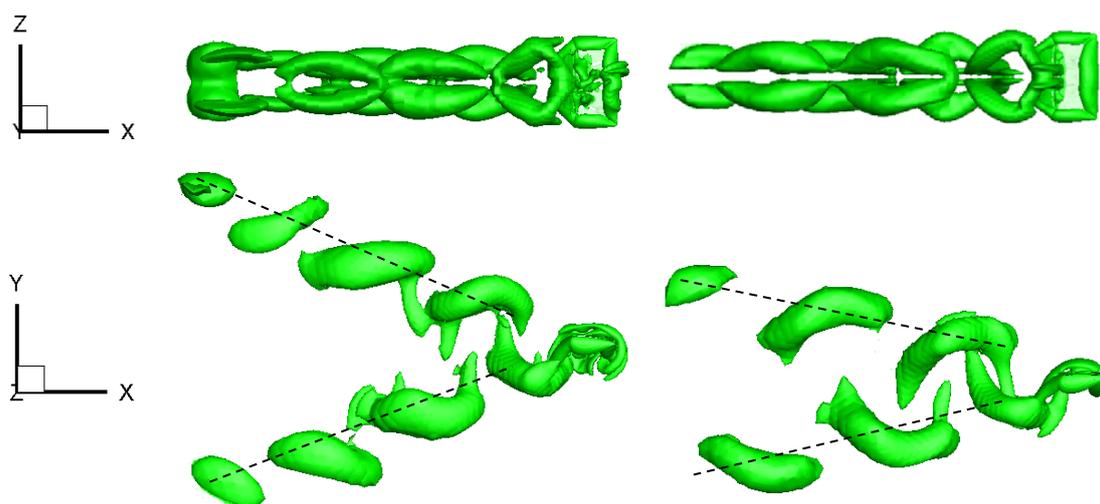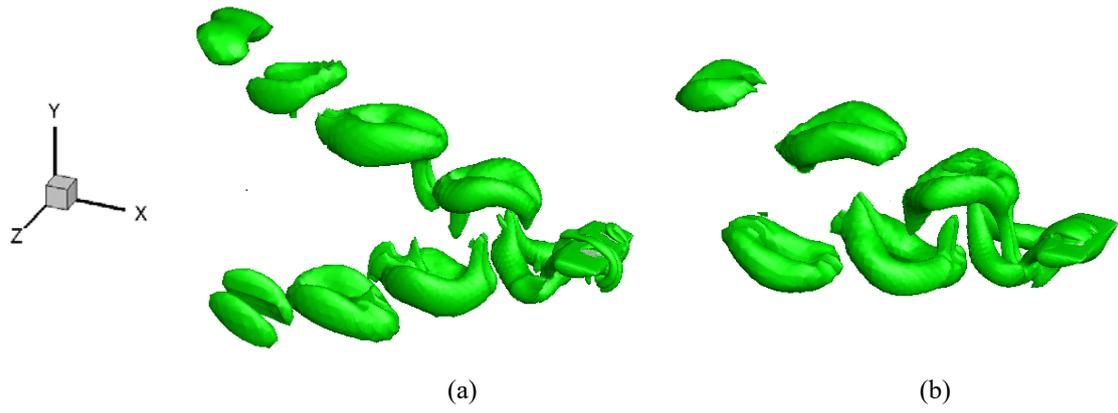
Figure 4.8 Vortex topology (Q contour) for 3D wing at different frequency ratio, with magnitude of iso-surfaces as 0.0002 ((σ=8.0, h=0.5, Re_{fr}=80 and AR=2.0)). (a) F=3.0. (b) F=8.0.
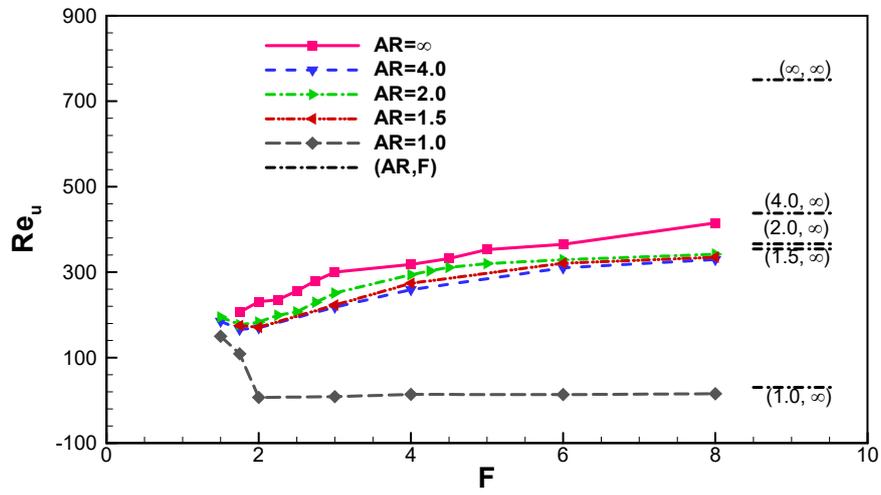
(a)
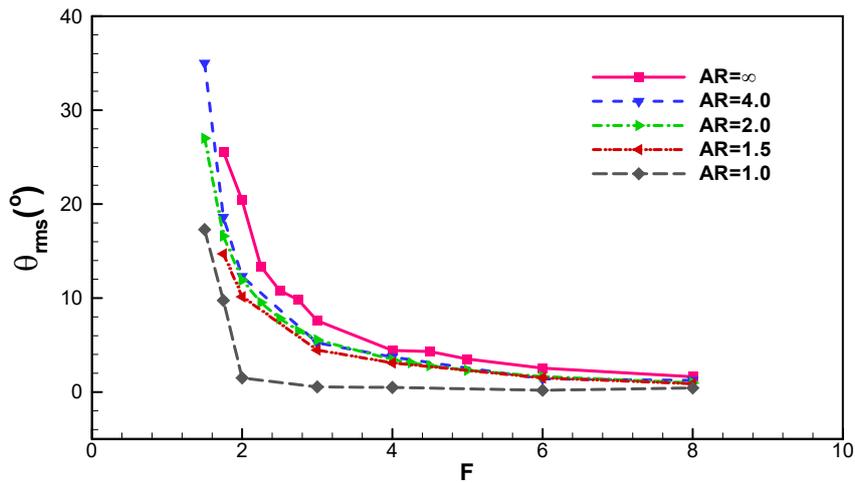
(b)

Figure 4.9 Final approached time-mean Re_u and θ_{rms} (σ=8.0, Re_{fr}=80, x/c=0). (a) Induced non-dimensional lateral velocity. (b) Induced pitching angle.

4.4.3 Effects of Aspect Ratio, Frequency Ratio (flexibility) and

Pivot-point

In this section, the effects of various parameter will be investigated. Our attention specially focuses on the aspect ratio (AR), frequency (F) and position of pitching axis. The variations of time-averaged lateral velocity (Re_u) and the root-squared pitching angle (θ_{rms}) with the increase of frequency ratio (F) at various aspect ratios (AR) are shown in Figure 4.9. The corresponding 1DoF case results ($F=\infty$) are also present as the dash-dot line in the right side of Figure 4.9 (a).

It is shown from Figure 4.9 that, for a moderate AR (ranging from 2.0 to 4.0) and a large F ($F > 4.0$), the differences in Re_u and θ_{rms} are small. However, a 2D foil (AR = ∞) obviously has larger propulsion velocity and pitching angle than those of a 3D wing. The impact of aspect ratio becomes more evident when the 3D wing becomes very short at AR=1.0, where both lateral and rotational motions are remarkably independent on the frequency ratio F, different from the trend observed for AR ≥ 1.5.

One striking finding from Figure 4.9 is that, apart from a very low aspect ratio case with AR = 1.0, the lateral Re_u increses monotonically with frequency ratio of the wing for rest of AR examined. This implies that the performance of a wing with torsional spring is even worse than a wing without spring, which seems contractory to the study of Spagnolie et al. (2010) and Zhang et al. (2010). To find out the problem, we performed a series of investigation on the pivot point effect by varying it from center-chord ($x/c = 0$) to leading edge ($x/c = 0.5$). The results are presented in Figure 4.10 for a 2D and 3D wing, respectively. Clearly found from the plots, the pivot point has a very apparent impact on the stiffness influence for wing propulsion. Our two-dimensional results plotted in Figure 4.10 (a) show that, below a threshold picthing axis, $x/c = 0.3$ here, a wing without torsional spring acheieves a better propulsion performance than a wing with spring. Beyond this value, Re_u vs F curve presents a non-monotanical trend. At a low F less than 2.0, where the wing is very flexible in rotational direction, the wing propulsion velocity increases sharply with F, enhibiting a flexible detrimental effect. Once F is large than 2.0, Re_u decreases with F, thus indicating a better performance of a flexible wing than a rigid wing. Our results

for $x/c > 0.3$ are remarkably similar to all relevant flexible wing flapping observations where the pitching axis is fixed at the leading edge (Spagnolie et al., 2010; Zhang et al., 2010). Another notable feature observed from Figure 4.10 is that, such pitching axis influence decays when the wing becomes more and more stiff (via increasing F), and is expected to lose its impact eventually when the wing turns into rigid.
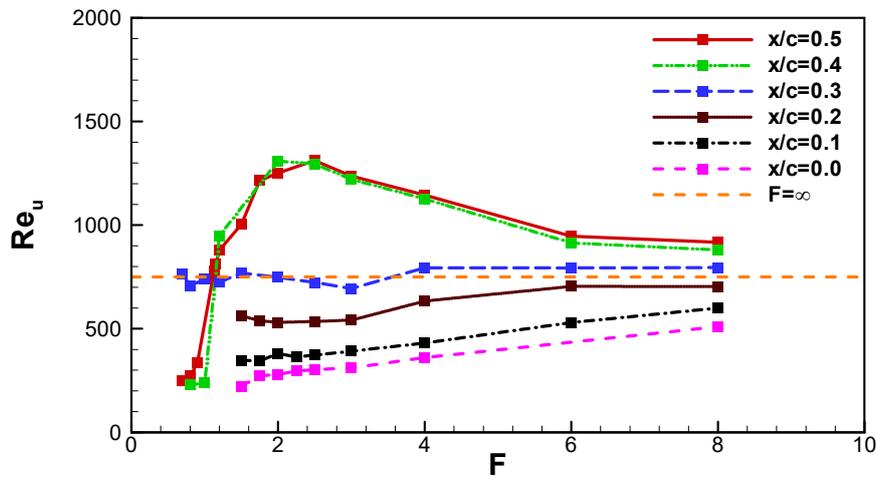
(a)
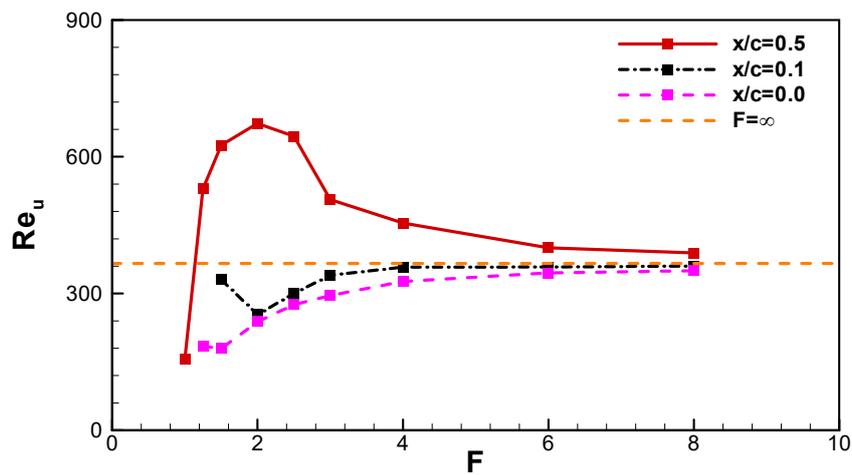
(b)

Figure 4.10 Effect of pitching axis on Re_u vs F (x/c=0 represents the wing pitching at its center-chord). (a) AR=∞. (b) AR=2.0.

(a)

(b)
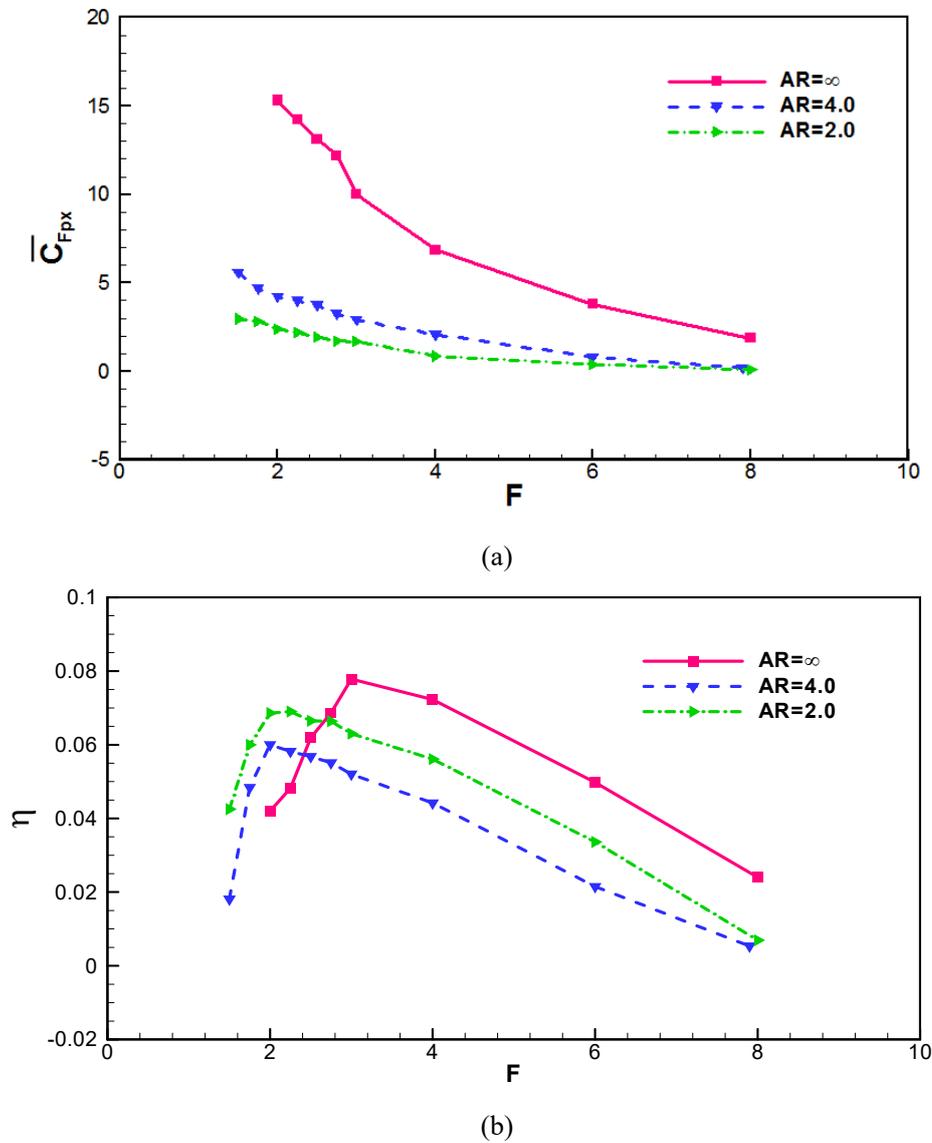
Figure 4.11 Frequency ratio (F) effect on the horizontal thrust force and efficiency (σ=8.0, Re_{fr}=80). (a) Thrust force coefficient. (b) Efficiency.

To further demostrate the above facts from the present study, the time-mean thrust pressure force (C_{Fpx}) in the lateral (x) direction and the corresponding propulsion efficiency η defined in Eq. (4.9) are plotted in Figure 4.11 with various frequency ratios (F) and AR. Obviously seen from the plots, the thrust force decreases monotonically with F for all AR examined. The maximum C_{Fpx} reaches at the

minimum frequency ratio at around $F = 1.5$ studied. However, an optimal efficiency is obtained around $F = 2.0$ and $F = 3.0$ for 2D foil and 3D wing, respectively. This definitely reinforces the optimal propulsion mechanism in the field of biology as revealed by relavant publications cited above (Kang et al., 2011; Ramananarivo et al., 2011). Refer to the flow status results presented in Section 5.3, we can conclude that the most desirable and efficient propulsion mode is Mode A. Compared to live fliers, the relative low efficiency shown in Figure 4.11 (b) might be due to the discrepancy in problem parameters selecting, such as flapping frequency (Re_{fr}) and density ratio (σ), which are different from the real animals as we mentioned in Sec. 4.1.

4.4.4 Effect of Density Ratio

The results for density ratio (σ) effect on Re_u and θ are summarized in Figure 4.12 for various aspect ratios (AR) and frequency ratios (F). Generally, the impact of density ratio on the lateral velocity Re_u is smaller than its influence on θ. In addition, the density ratio impact is influenced by the wing aspect ratio. For a 2D wing under 2DoF, represented by (∞, *) in the figure, increasing density ratio leads to a slightly enlarged Re_u and a small pitching angle. This trend is also relevant to wing stiffness (F). Large F implies a much stiffer wing, thus the density ratio effect is less apparent. This is clearly reflected by the wing with a (∞, ∞) combination, where the pitching angle is equal to zero and thus Re_u remains a constant as 755. With a 3D wing, given a density ratio (σ), again, we found that large aspect ratio has a relatively large propulsive velocity and rotational angle. For the present problem, i.e. a self-propelled 3D wing with 2DoF, this finding is especially important, as it links the system dynamic response to the external fluid force. In particular, the inertial force influence on the system stability via the density ratio. With a fixed density ratio, the mass of a small AR wing must be smaller than a wing with large AR. The small mass represents small inertia, and more sensible to the variation from the external force or moment.

(a)

(b)
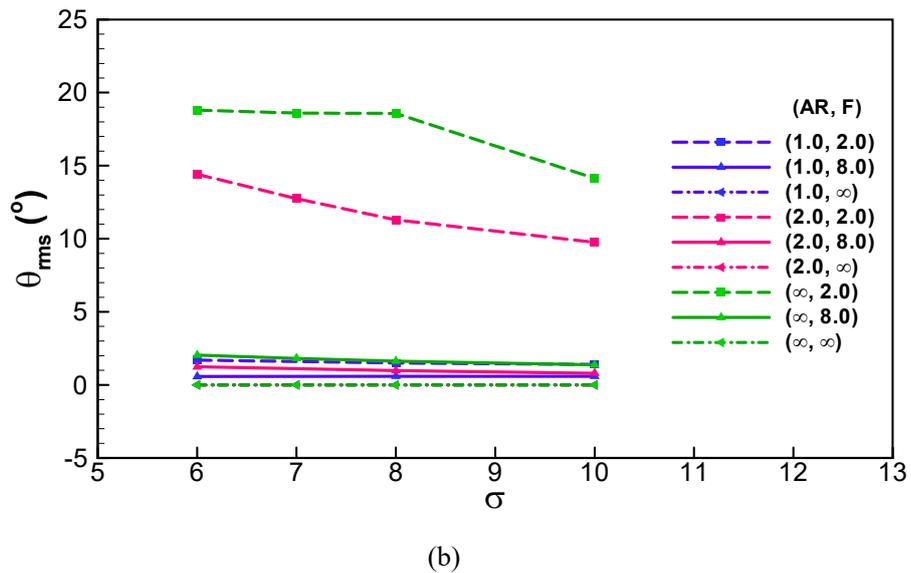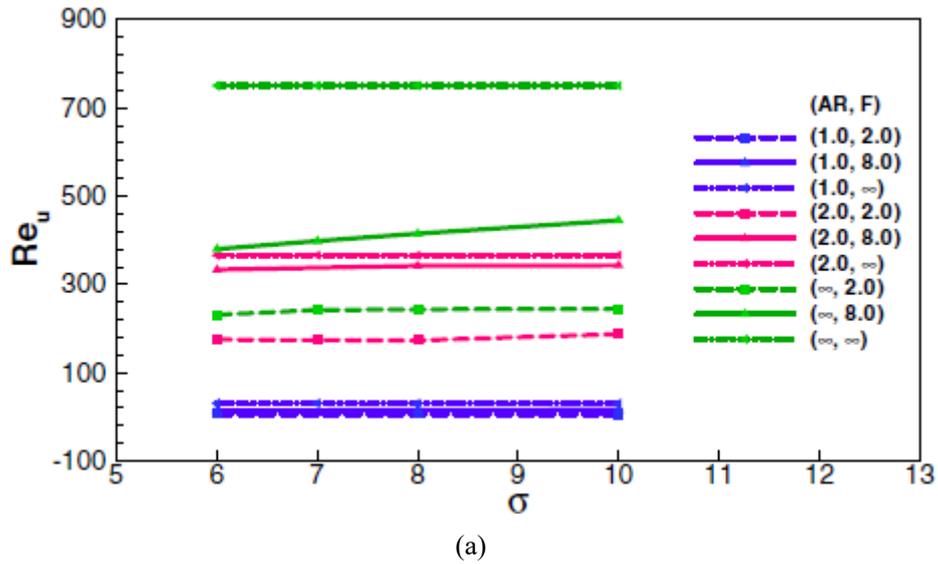
Figure 4.12 Density ratio effect on the induced lateral velocity and pitching angle (Re_{fi}=80) (a) Averaged induced non-dimensional lateral velocity Re_u. (b) Induced pitching angle θ.

The development history of $\tilde{Re}_u$ and θ are plotted in Figure 4.13 for various density ratio at AR = 2.0 and F = 2.0. Obviously seen, due to the larger inertia, the system with large density ratio presents a small variation both on $\tilde{Re}_u$ and θ. The evolution

time to reach the final stable state is also increased. It should be pointed out that the wings of insects and birds usually have much larger density ratios on the order of several thousands (Ramananarivo et al., 2011), which compared to the relatively low density ratios in the present study, may enhance the stability of the dynamic flight system in terms of the nonlinear interaction between aerodynamics and inertial dynamics.
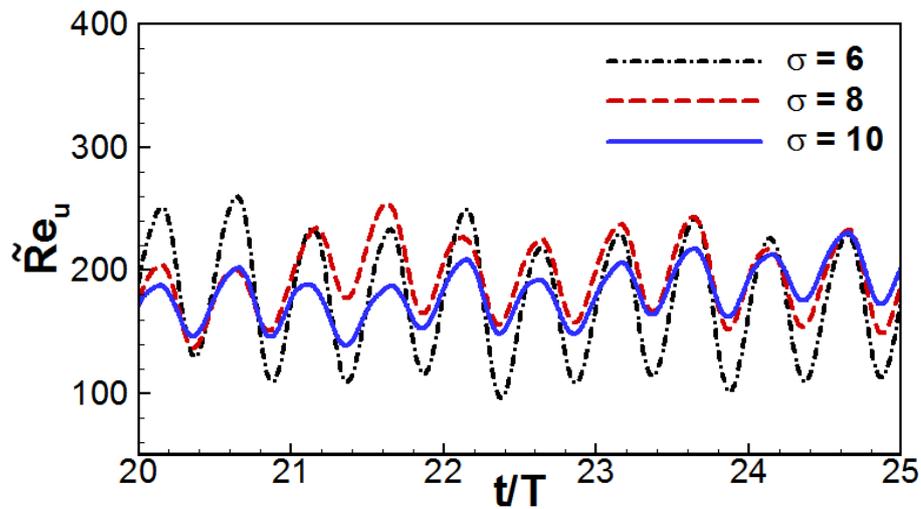
(a)
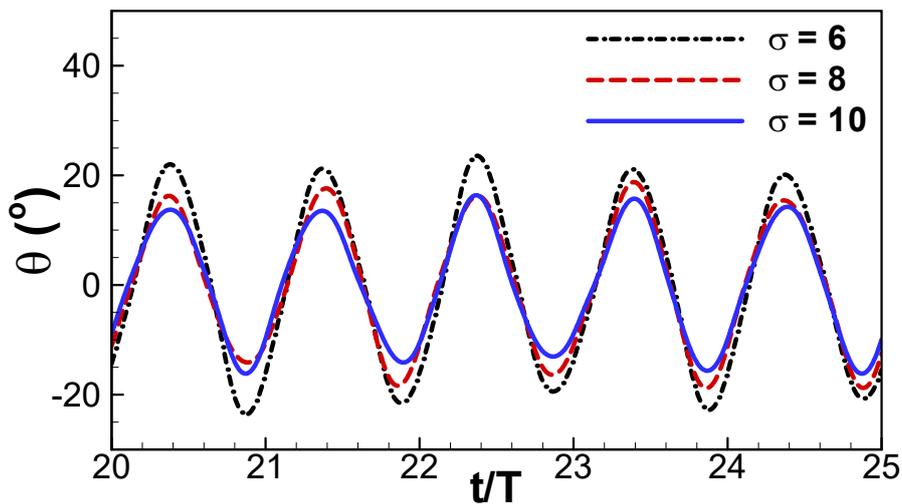
(b)

Figure 4.13 Density ratio effect on the evolution of $\tilde{\text{Re}}_u$ and θ (Re_{fr}=80, AR=2.0 and F=2.0). (a) Induced non-dimensional lateral velocity $\tilde{\text{Re}}_u$. (b) Induced pitching angle θ.

4.5 Discussion

The present study aims to understand the fundamental fluid mechanism utilized by some live animals using a flapping motion for their thrust/lift generation and propulsion, which is made possible by the wings' inherent flexible with this simplified model. Our aim is to investigate this system dynamic response to the symmetry breakdown. It is believed that the results obtained are vital to elucidate the flexible wing propulsion mechanism.

The simulations show that the development history of lateral and rotational motion is similar to the studies of Spagnolie et al. (2010) and Zhang et al. (2010) for a two-dimensional foil and flat plate. In particular, the evolution follows left/right symmetry, an asymmetry, and eventually a stable forward or backward movement combined with a rotational pitching. However, our simulations of a low aspect ratio wing show that, a 3D wing takes a longer developing history for breaking the symmetric flow structure around the wing and reaching its final stable state than a 2D wing. Such a three-dimensional effect that is responsible for enhancing or stabilizing force generation can also be observed in flying insects and manoeuvring fish that fly or swim at low Reynolds numbers by flapping their wings or pectoral fins with low aspect ratios as compared to those of bat and birds.

Analysis of the data within the fully developed flow regimes shows that the wing always pitches at the same frequency as forced flapping frequency, irrelevant to the wing's torsional stiffness and this is consistent with the study of Zhang et al. (2010), which indicates that the low aspect ratio wing edge does not affect the dynamics of passive pitching in this aspect. On the other hand, for the lateral motion, both results show that the induced lateral velocity oscillating frequency is profoundly dependent on the wing torsional stiffness, varying from multiple frequencies to one dominant frequency with the increase in the wing's stiffness [Figure 7 in Zhang et al. (2010)]. In addition, apart from Mode B-2 where the $\tilde{R}e_u$ frequency is twice of flapping frequency found by Zhang et al. (2010) for their flat plate, we observed Mode B-1 state for our 2D wing, in which $\tilde{R}e_u$ oscillating frequency appears to be the same as the flapping frequency. Considering the different parameters and geometry examined

in the two studies, we can conclude that the dynamic response of such a flapping wing system is complicated, and very much dependent on the various system kinematic and structural parameters.

Further studies on the hydrodynamic performance of these wings in the fully developed state show that, the wing aspect ratio, frequency ratio, density ratio and even the pitching axis have remarkable effects on their propulsion performance. The wings with large aspect ratios always show large thrust force and thus a large Re_u than those of short spans. The vortex structure around the wing body shows that this is the result of a stronger reverse von Kármán vortex street generated in the wake of large AR wing. Surprisingly, we found that the stiffness influence on the wing propulsion is strongly linked to the pitching axis. Introduction of the pivot point away from chord-centre to the leading edge leads to an improvement of propulsion performance. Further studies on this aspect would be our near future direction. In addition, the analysis of thrust force and efficiency relation with wing torsional stiffness shows that, maximum thrust is generated when the wing flaps at its natural frequency, while the optimal efficiency is instead obtained if the wing flaps at the half of its natural frequency. This conclusion remarkably resembles the observations from biological fliers and swimmers, even though some parameters in the present studied is beyond the range of that of real animal. Our results also shows the predominant range for torsional stiffness impact on the propulsion of wing is between frequency ratios of F=0.7 to 4.0.

Chapter 5   Mobile Multi-body System

5.1 Introduction

Here in the current chapter, the basic philosophy of Mobile Multi-body System (MMS) model is introduced in aspects of design of MMS model and dynamics of the system. Governing equations of MMS model are derived, following by numerical algorithms of solutions. A method is illustrated for implementing the multi-body dynamics into CFD solver for solving the problems of MMS model in fluid. Emphasis is to create a solution for such coupling problems with both internal dynamics (multi-body dynamics) and external dynamics (hydrodynamics), so that the induced external motion under internal undulatory body propulsion can be predicted accurately through fully resolved numerical simulations. The algorithm and verification cases are given, and an innovative test case is applied on a simplified model of an articulated fish body with a rigid head and soft tail for exploring the flexibility effect on fish propulsion performance, in which case the soft tail is modelled by two rigid segments connected through a spring joint.

5.2 Mobile Multi-body System (MMS)

We aim to propose a model that has the following advantages:

- This model can mimic the swimming fish or flying bird/insect as a whole system, including both the actuated and passive parts;

- This model can be considered as a prototype model for the design of robotic fish or bird/insect with the internal dynamics being taken into account.

One of the most effective approaches is to discretize the continuum of the fish/bird

body into finite segments/elements to mimic the entire structure or bones, and use hinges/actuators to link all the segments to mimic the inertial muscle forces, so the internal body dynamics can be taken into account. The present MMS model addresses all aspects mentioned above. The treatment of the connection joints enables us to study the effect of internal dynamics in the cases of a passive joint (mimicking relaxing parts of body with passively induced motion) and an active joint (mimicking simulated muscles producing motion actively).

5.2.1 Design of MMS Model – From Two/Three DoF to Many DoF

The MMS model can be considered as a combination of a series of linked rigid segments. With different arrangements of rigid bodies and joints, different structures can be created. In the following, serial-type structure and tree-type structure are revealed respectively.

5.2.1.1 Serial-Type Structure

To mimic the undulation of fish body, several rigid bodies are arranged one by one serially. The schematic view is shown in Figure 5.1. The red elliptical elements represent the rigid bodies, and their sizes can be determined by the real fish geometry, e.g. the element sizes are decreasing gradually from the fish head to fish tail in Figure 5.1. The small black circulars are the hinges, the types of which may have different kinematic behaviour at different locations according to the body posture of propulsion.
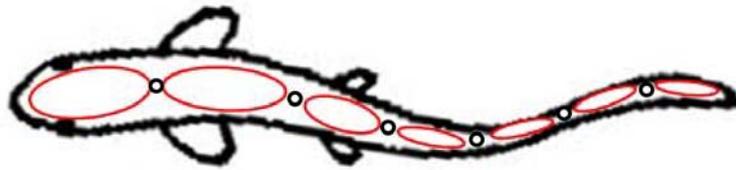
Figure 5.1 Schematic of serial-type structure to mimic fish body undulation.

Comparing to a single flapping foil/wing model which has maximum three DoF two-dimensionally (two DoF in lateral and translational directions and one rotational DoF), current MMS model may have up to 3n DoF in two dimensional space (herein n is the number of rigid elements). From the control point of view, with sufficient DoF, the manoeuvrability and flexibility of the system can be significantly improved, and the fish-like undulation can be mimicked accurately.

5.2.1.2 Tree-Type Structure

The tree-type structure is given in Figure 5.2, which is used to design a robotic flying bird (Porez et al., 2014a). As shown in Figure 5.2, the robotic bird is made up with one main body and two flapping wings with two rigid elements in each wing. In this model, there are two hinges attached between each pair of adjacent elements, so that the rotation motion of the wing can be controlled in two directions.
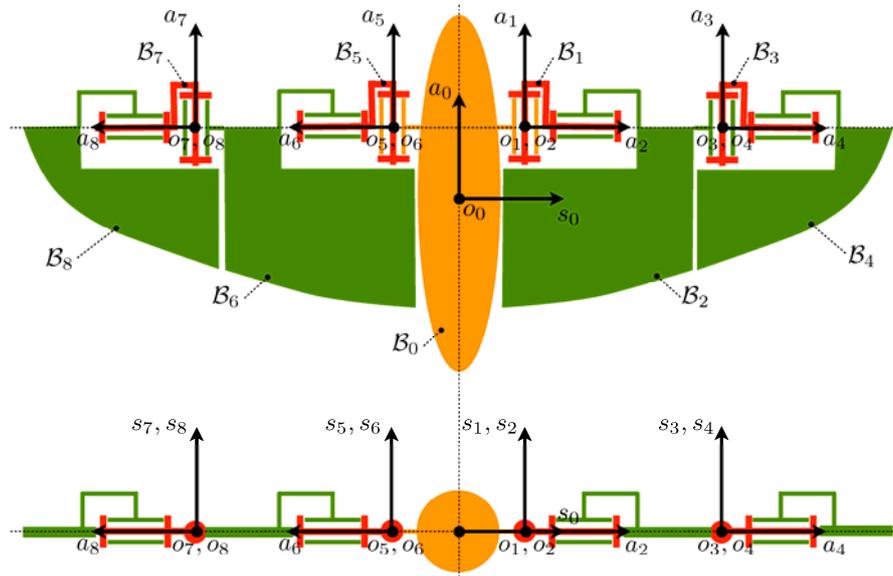
Figure 5.2 Schematic of tree-type structure of a robotic flying bird. Courtesy of Porez et al. (2014a).

The construction of MMS system is more straightforward comparing to that of fully deformable structure. However, the dynamics of the system is not simple due to the complexity lead by the interactions between rigid elements and hinges. In the following, the governing equations of the model dynamics and the relevant algorithms to solve the equation system are demonstrated thoroughly mainly on the serial-structure, which is the focus of this study in the current preliminary stage.

5.2.2   Components of MMS Model

The schematic view of a simple MMS model is shown in Figure 5.3, in which the model is with serial-type structure and joints/hinges evolution is governed by stress-strain laws or control torques. The model composes of a sequence of (N+1) rigid segments interconnected through (N) revolute hinges. Each rigid segment

follows the coupled motion induced by adjacent segments and transferred through the revolute hinges with 1DoF in pitch direction.
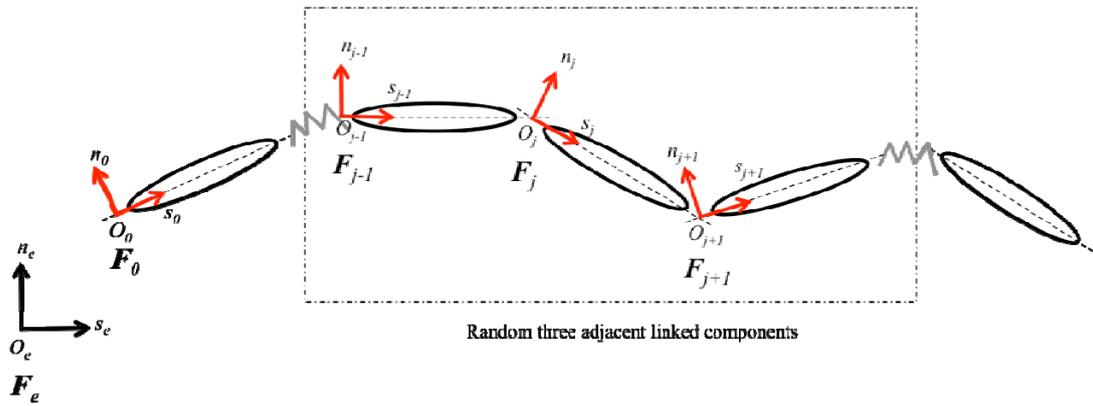
Figure 5.3 Representation of frames location at the MMS model.

Basically, there are two types of joint models considered in this study, i.e. active joint and passive joint. The active joint behaves as an actuator with an independent motor driving the pair of connected shafts. The pitch motion of passive joint is induced from the interaction with its preceded and succeeded segments internally following the environment change of external conditions.

The active joint applies angle controlling system model, and the relative angle between two adjacent rigid segments are prescribed on the hinge as

$$r = r_0(t) \,. \tag{5.1}$$

The passive joint operates torsional spring system model. A typical stiffness-damper spring system is shown in Eq. (5.2),

$$\tau = -R^* \dot{r} - K^* r, \tag{5.2}$$

where R^* and K^* represent damping and stiffness respectively, r and $\dot{r}$ are pitching angle and angular velocity, and τ is torque applied for driving the motion.

5.2.3   Parameterisation and Notations

In accordance with Figure 5.3, we attach a fixed spatial frame denoted by $\boldsymbol{F}_e = (O_e, s_e, n_e, a_e)$, where O_e represents the origin of frame, the unit vector a_e is normal to the model moving plane, s_e and n_e are in the horizontal and vertical directions respectively. These links are denoted by B_0, B_1, …, B_n, from B_0 toward the tip of the branch in increasing order, and B_0 represents the reference body. In the following, j and i ($i = j$-1) are denoted as the indices of the current body and its antecedent in the branch respectively. Mobile frame, $\boldsymbol{F}_j = (O_j, s_j, n_j, a_j)$, is attached to arbitrary body B_j, and the centre, O_j, coincides with the centre of the joint j (the joint between B_i and B_j). The unit vector s_j supports the line from O_j to O_{j+1}, n_j is in normal direction, and a_j points to the angular joint axis. In particular, the origin of $\boldsymbol{F}_0$ locates at an arbitrary position on the centreline of reference body and represents the location of entire MMS model relative to the fixed frame.

At any time t, the model configuration is expressed with joint relative angles, $r(t)=(r_1,…, r_n)^{\mathrm{T}}(t)$, defining the relative angular positions of the joint axis between the adjacent bodies. The mobile frame of the reference body, $\boldsymbol{F}_0$, with respect to the fixed frame, $\boldsymbol{F}_e$, is attached through orientation matrix, $^eR_0$, and position vector, $^eP_0$. The time evolution of $^eR_0$ and $^eP_0$ defines net motion of MMS model. The notation convention is defined that for any physical variable modelled by a tensor, the right lower index represents body index (to which it is related) while the left upper exponent indicates index of the projection frame. When the tensor related to a body is expressed in the mobile frame of this body, the upper index is omitted. The temporal derivative $\partial./\partial t$ is sometimes denoted by a upper dot.

5.2.4   Newton – Euler Framework Application

The transformation of each pair of frames can be derived based on Newton – Euler Framework, and it can be demonstrated as the schematic diagram shown in Figure 5.4.

The transformation from $\boldsymbol{F}_i$ to $\boldsymbol{F}_j$ can be achieved in a few steps, and each of them can be expressed as a function of relative parameters/variables, shown as below:
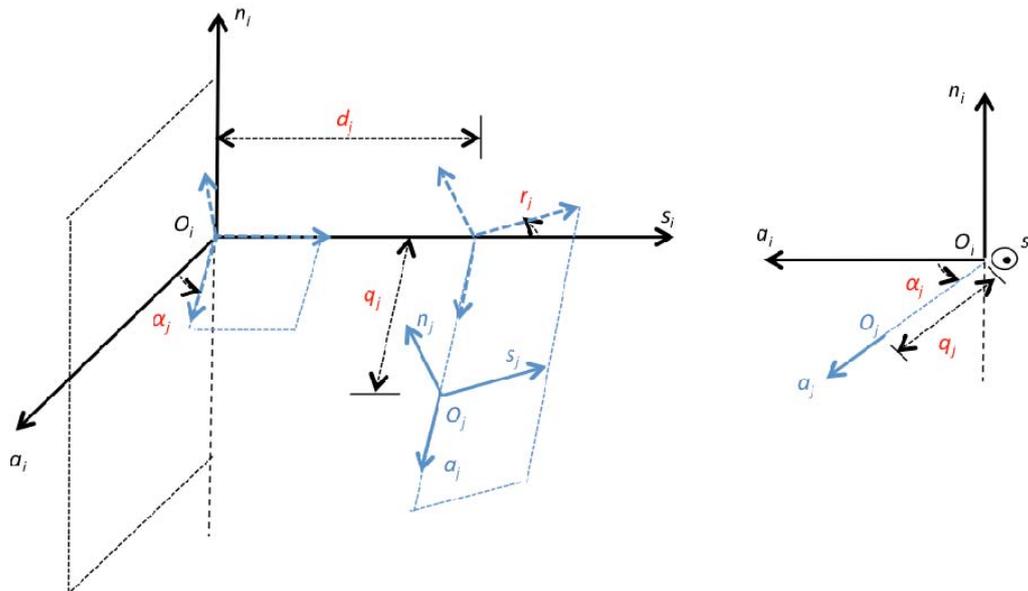
Figure 5.4 Representation of frame transformation.

- rot(s, α_j): rotate the frame with an angle of α_j about axis s;

- trans(s, d_j): translate the frame with a distance of d_j along axis s;

- rot(a, r_j): rotate the frame with an angle of r_j about axis a;

- trans(a, q_j): translate the frame with a distance of q_j along axis a.

The homogeneous transformation matrix defining frame $\boldsymbol{F}_j$ relative to $\boldsymbol{F}_i$ is a result of matrix production in form of a (4×4) matrix,

$$^iT_j = \text{rot}(s, \alpha_j)\text{trans}(s, d_j)\text{rot}(a, r_j)\text{trans}(a, q_j)$$

$$= \begin{pmatrix} \cos r_j & -\sin r_j & 0 & d_j \\ \cos\alpha_j \sin r_j & \cos\alpha_j \cos r_j & -\sin\alpha_j & -q_j \sin\alpha_j \\ \sin\alpha_j \sin r_j & \sin\alpha_j \cos r_j & \cos\alpha_j & q_j \cos\alpha_j \\ 0 & 0 & 0 & 1 \end{pmatrix} \qquad (5.3)$$

$$= \begin{pmatrix} ^iR_j & ^iP_j \\ 0 & 1 \end{pmatrix}$$

We define a (3×3) matrix, ^iR_j, and a (3×1) vector, ^iP_j, as orientation matrix and position vector of frame $\boldsymbol{F}_j$ with respect to frame $\boldsymbol{F}_i$ respectively. In the present study, the relative angle, r, between axis s of two adjacent mobile frames dominant the robot configuration, therefore matrix ^iR_j can be represented as $^iR_j(r_j)$.

The transformation matrix of mobile frame relative to the fixed frame can be expressed as

$$^eT_j = {}^eT_i\, {}^iT_j(r_j)$$

$$= {}^eT_i \begin{pmatrix} ^iR_j(r_j) & ^iP_j \\ 0 & 1 \end{pmatrix}. \qquad (5.4)$$

Position of the origin of mobile frame can be expressed in the fixed frame as

$$^eP_j = {}^eP_i + {}^eR_i\, {}^iP_j. \qquad (5.5)$$

Velocity of B_j is denoted by a (6×1) vector, ^jV_j, and the relation to the velocity of B_i is expressed as

$$^jV_j = \begin{pmatrix} ^jv_j \\ ^jw_j \end{pmatrix}$$

$$= \begin{pmatrix} ^jR_i({}^iv_i + {}^iw_i \times {}^iP_j) \\ ^jR_i\, {}^iw_i + \dot{r}_j a_j \end{pmatrix}. \qquad (5.6)$$

$$= Ad_{^jg_i}\, {}^iV_i + \dot{r}_j A_j$$

Here, ^jv_j and ^jw_j are (3×1) vectors of linear and angular velocities, represented in the

fixed frame. $A_j = (0_3^T, a_j^T)$ is a (6×1) unit vector, with a_j^T as $(0, 0, 1)^T$ representing the degree of freedom of joint hinges. Ad_{jg_i} is an adjoint map operator allowing to change the (6×1) velocity vector ^iV_i from frame F_i to frame F_j, as

$$Ad_{jg_i} = \begin{pmatrix} ^jR_i & ^jR_i{}^i\hat{P}_j^T \\ 0 & ^jR_i \end{pmatrix}.$$

(5.7)

Here, the hat notation changes a (3×1) vector into its associated (3×3) skew-symmetric tensor, for any vector $\mathbf{A}$ in size of 3×1 and tensor $\mathbf{B}$ in size of 3×3, they have the relationship as $\hat{\mathbf{A}}\mathbf{B} = \mathbf{A} \times \mathbf{B}$. ^iP_j is considered as a radius displacement matrix of transferring the angular velocity to linear velocity, and the transformation is made as below,

$$^i\hat{P}_j^T = \begin{pmatrix} 0 & ^iP_j(a_j) & -^iP_j(n_j) \\ -^iP_j(a_j) & 0 & ^iP_j(s_j) \\ ^iP_j(n_j) & -^iP_j(s_j) & 0 \end{pmatrix}.$$

(5.8)

By time differentiation of Eq. (5.6), the acceleration, $^j\dot{V}_j$, is given by

$$^j\dot{V}_j = \begin{pmatrix} ^j\dot{v}_j \\ ^j\dot{w}_j \end{pmatrix}$$
$$= \begin{pmatrix} ^jR_i(^i\dot{v}_i + ^i\dot{w}_i \times ^iP_j + ^iw_i \times (^iw_i \times ^iP_j)) \\ ^jR_i{}^i\dot{w}_i + (^jR_i{}^iw_i) \times (\dot{r}_j a_j) + \ddot{r}_j a_j \end{pmatrix},$$
$$= Ad_{jg_i}{}^i\dot{V}_i + \varsigma_j + A_j\ddot{r}_j$$

(5.9)

where ς_j is a part of acceleration as shown below,

$$\varsigma_j = \begin{pmatrix} ^jR_i(^iw_i \times (^iw_i \times ^iP_j)) \\ (^jR_i{}^iw_i) \times (\dot{r}_j a_j) \end{pmatrix}.$$

(5.10)

In addition, the force transformation from frame F_j to frame F_i is expressed as

$$i f_j = (Ad_{j_{g_i}})^T f_j$$

$$= \begin{pmatrix} {}^i R_j & 0 \\ {}^i \hat{P}_j \, {}^i R_j & {}^i R_j \end{pmatrix} \begin{pmatrix} F_j \\ M_j \end{pmatrix}, \tag{5.11}$$

where f_j is (6×1) force and moment vector exerted by body i on body j.

5.2.5 Governing Equations for Dynamic Motions

Following derivation of the transformation matrix between different frames, governing equation of each element is derived in this section. By applying Newton's Second Law and Euler's theorem to the jth body, dynamic equations of B_j can be obtained in Newton – Euler form as

$$f_j - (Ad_{j+1_{g_j}})^T f_{j+1} = M_j \, {}^j \dot{V}_j + \beta_j - f_{ext,j}. \tag{5.12}$$

Here, $f_{ext,j}$ is a (6×1) vector, representing external fluid force and moment exerting on B_j, and β_j is a (6×1) vector representing Coriolis and centrifugal forces, as shown here

$$\beta_j = \begin{pmatrix} {}^j w_j \times ({}^j w_j \times MS_j) \\ {}^j w_j \times ({}^J I_j \, {}^j w_j) \end{pmatrix}. \tag{5.13}$$

M_j is an (6×6) inertia tensor of body j as below, and M_j, $M\hat{S}_j$ and I_j are (3×3) tensors of the body mass, the first inertia moments and angular inertia with respect to link j respectively.

$$M_j = \begin{pmatrix} M_j & -M\hat{S}_j \\ M\hat{S}_j & I_j \end{pmatrix} \tag{5.14}$$

Up to now, the governing equations of MMS model are derived, but with the increasing number of elementary bodies, the solution turns complicated. In the following sections, relevant algorithms for solving this equation system is demonstrated.

5.2.6 Development of Governing Equations

Eq. (5.12) can be constructed to be an equation system with variables of internal interactive forces and moments, acceleration term, and external forces and moments of individual segment as shown in Eq. (5.15).

$$f_N - 0 = M_N \,{}^N\dot{V}_N + \beta_N - f_{ext,N}$$

$$f_{N-1} - Ad^T_{N_{g_{N-1}}} f_N = M_{N-1} \,{}^{N-1}\dot{V}_{N-1} + \beta_{N-1} - f_{ext,N-1}$$

$$\vdots$$

$$f_j - Ad^T_{j+1_{g_j}} f_{j+1} = M_j \,{}^j\dot{V}_j + \beta_j - f_{ext,j} \qquad (5.15)$$

$$f_i - Ad^T_{j_{g_i}} f_j = M_i \,{}^i\dot{V}_i + \beta_i - f_{ext,i}$$

$$\vdots$$

$$0 - Ad^T_{1_{g_0}} f_1 = M_0 \,{}^0\dot{V}_0 + \beta_0 - f_{ext,0}$$

A further development can be made on building a recursive equation system by coupling Eq. (5.9) with Eq. (5.15). Taking B_i and B_j for example, the dynamic equations turn as Eq. (5.16), when the acceleration term of B_j is expressed by the relevant terms of B_i based on Eq. (5.9).

$$\vdots$$

$$f_j - Ad^T_{j+1_{g_j}} f_{j+1} = M_j (Ad_{j_{g_i}} {}^i\dot{V}_i + \varsigma_j + \ddot{r}_j A_j) + \beta_j - f_{ext,j}$$

$$f_i - Ad^T_{j_{g_i}} f_j = M_i \,{}^i\dot{V}_i + \beta_i - f_{ext,i} \qquad (5.16)$$

$$\vdots$$

An adjoint map operator, $Ad^T_{j_{g_i}}$, transferring variables from F_j to F_i can be multiplied on the dynamic equation of B_j, and the internal force and moment component, f_j, will be eliminated after being added with the equation of the antecedent body B_i. The variables in the right hand side of equations are mostly available except the individual segment acceleration $({}^i\dot{V}_i)$ and connected joint angular acceleration $(\ddot{r}_j)$, where the former is the main unknown variable and the latter depends on the joint control system. In general, when the elimination procedure is completed from body index N

to 0, the acceleration term of reference body (B_0) can be calculated through a derived equation that is under an expression similar as Newton's Second Law.

The way to make elimination depends on the joint model. Main differences between actuated and passive hinge model are the availability of angular acceleration. Actuated hinge has known angular acceleration at the beginning of the recursive time step. Passive hinge is under the contrary situation that the angular acceleration is obtained as an output variable under the condition of known applied torque. It is noted that the solution of actuated joints is straightforward, whereas that of passive joints has one additional step of substituting the unknown angular velocity by torque and other relevant terms. The details are illustrated in the following sub-sections.

5.2.6.1 *Actuated (Active) Joints*

If we assume when body index i belongs to (0, N-1),

$$\mathrm{M}_i^* = \mathrm{M}_i + Ad_{j_{g_i}}^T \mathrm{M}_j^* Ad_{j_{g_i}} , \tag{5.17}$$

$$\beta_i^* = (\beta_i - f_{ext,i}) + Ad_{j_{g_i}}^T (\mathrm{M}_j^*(\varsigma_j + \ddot{r}_j A_j) + \beta_j^*) , \tag{5.18}$$

and when $i = $ N,

$$\mathrm{M}_N^* = \mathrm{M}_N ,$$

$$\beta_N^* = (\beta_N - f_{ext,N}) ,$$

all the variables represented in local frame of B_i in Eq. (5.16) turns into a typical Newton's Second Law's expression as following, after summing up all the dynamic equations of bodies with index bigger than i recursively.

$$f_i = \mathrm{M}_i^* {}^i\dot{V}_i + \beta_i^* . \tag{5.19}$$

In the frame of reference body, all the internal forces and moments are eliminated, and the acceleration of the reference body turns as,

$$^{0}\dot{V}_{0} = -(M_{0}^{*})^{-1}\beta_{0}^{*}. \tag{5.20}$$

The variables of M_{0}^{*} and β_{0}^{*} can be calculated through the recursive loops, so that the acceleration of reference body can be obtained. Once the accelerations of reference body are available, the accelerations for any other bodies can be easily computed from Eq. (5.9). The torques applied on the actuated joints by the adjacent bodies can be calculated from the following equation:

$$\tau_{j} = A_{j}^{T}(M_{j}{}^{j}\dot{V}_{j} + \beta_{j} - f_{ext,j}). \tag{5.21}$$

5.2.6.2 Passive Joints

For passive joints, the torque (τ_{j}) can be calculated in advance through typical stiffness-damper spring system as Eq. (5.2). Combining Eq. (5.9) and Eq. (5.21) as shown below,

$$\tau_{j} = A_{j}^{T}(M_{j}(Ad_{j_{g_{i}}}{}^{i}\dot{V}_{i} + \varsigma_{j} + A_{j}\ddot{r}_{j}) + \beta_{j} - f_{ext,j}), \tag{5.22}$$

the angular acceleration of joint j, $\ddot{r}_{j}$, can be expressed as

$$\ddot{r}_{j} = (H_{j})^{-1}(\tau_{j} - A_{j}^{T}(M_{j}(Ad_{j_{g_{i}}}{}^{i}\dot{V}_{i} + \varsigma_{j}) + \beta_{j} - f_{ext,j})),$$

$$\text{with} \quad H_{j} = A_{j}^{T}M_{j}A_{j} . \tag{5.23}$$

Thus a substitution of $\ddot{r}_{j}$ by τ_{j} can be conducted on the governing equation of B$_{j}$ [Eq. (5.12)], and the terms in the right hand side turns in a form as

$$M_{j}{}^{j}\dot{V}_{j} + \beta_{j} - f_{ext,j} = (M_{j} - M_{j}A_{j}(H_{j})^{-1}A_{j}^{T}M_{j})Ad_{j_{g_{i}}}{}^{i}\dot{V}_{i}$$

$$+ (M_{j} - M_{j}A_{j}(H_{j})^{-1}A_{j}^{T}M_{j})\varsigma_{j} \tag{5.24}$$

$$+ M_{j}A_{j}(H_{j})^{-1}(\tau_{j} - A_{j}^{T}(\beta_{j} - f_{ext,j})) + \beta_{j} - f_{ext,j}$$

If we assume, when i belongs to (0, N-1),

$$M_{i}^{*} = M_{i} + Ad_{j_{g_{i}}}^{T}\kappa_{j}Ad_{j_{g_{i}}}, \tag{5.25}$$

$$\beta_{i}^{*} = (\beta_{i} - f_{ext,i}) + Ad_{j_{g_{i}}}^{T}\alpha_{j}, \tag{5.26}$$

with

$$\kappa_j = M_j^* - M_j^* A_j (H_j)^{-1} A_j^T M_j^*, \tag{5.27}$$

$$\alpha_j = \kappa_j \varsigma_j + M_j^* A_j (H_j)^{-1} (\tau_j - A_j^T \beta_j^*) + \beta_j^*, \tag{5.28}$$

and when $i = N$,

$$M_N^* = M_N,$$

$$\beta_N^* = (\beta_N - f_{ext,N}),$$

all the sum-up variables represented in frame of B_i turns to a form as in Eq. (5.19). The acceleration of reference body can be obtained similarly as active joint.

5.2.7   MMS Model Solution by a Hybrid Method

Generally, essential motion variables of the system in global coordinate are characterised by a vector, X_{state}, including information of the position of reference body $(^e g_0, {}^e P_0,)$, linear and angular velocities of reference body $(^e V_0)$, and angular velocity of all the hinge joints $(r, \dot{r})$. $P_{control}$ is a variable with information of input joint conditions, i.e. pitching acceleration for active joint $(\ddot{r}_a)$ and torque applied on the passive joint (τ_p). N_{output} indicates the variables to be obtained from the MMS algorithm, with information of torque of actuating the active joint (τ_a), and angular acceleration of passive joint $(\ddot{r}_p)$.
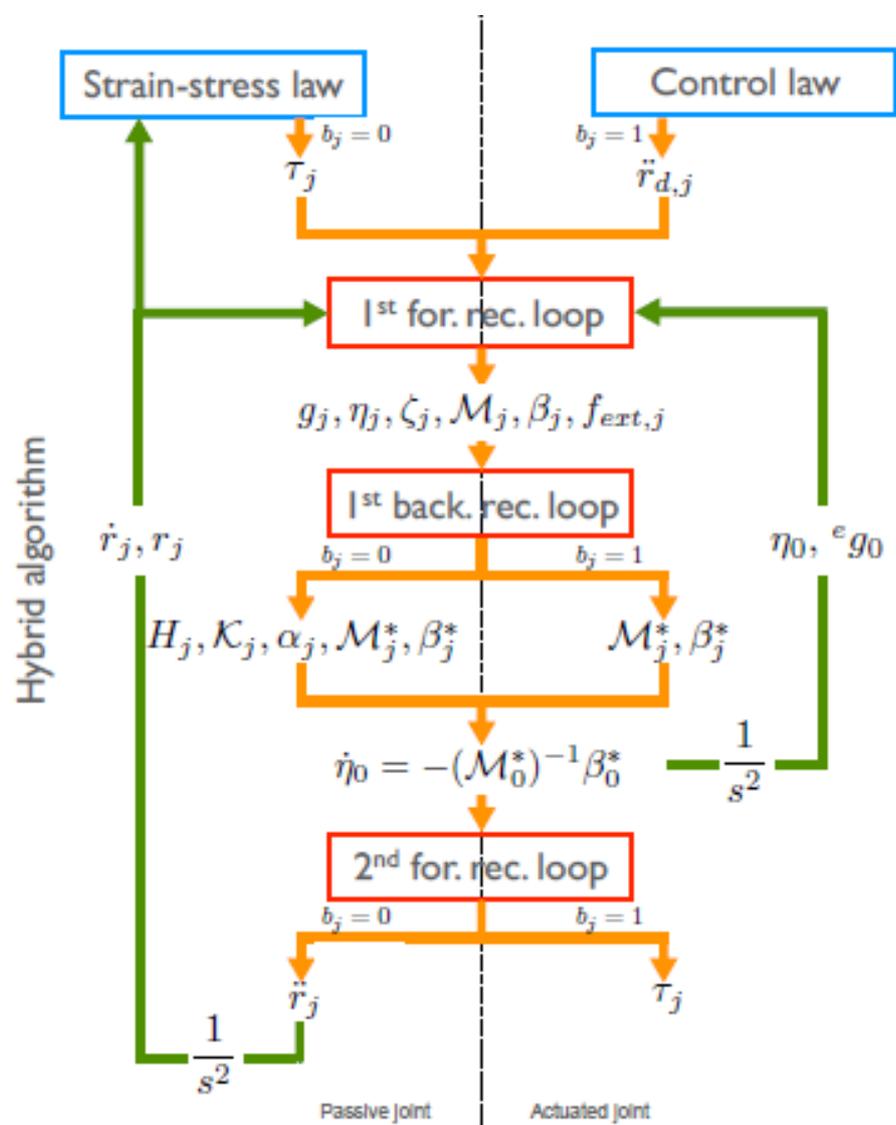
Figure 5.5 Flow chart of the proposed hybrid algorithm. [Refer to Fig. 2 in Porez et al. (2014a)]

$$\begin{aligned}
\mathrm{X}_{\text{state}} &= (^e g_0, {}^e V_0, {}^e P_0, r, \dot{r}) \\
\mathrm{P}_{\text{control}} &= (\ddot{r}_a, \tau_p) \\
\mathrm{N}_{\text{output}} &= (\tau_a, \ddot{r}_p)
\end{aligned} \qquad . \qquad (5.29)$$

In accordance with the assumptions and dynamic equations aforementioned, the flow chart of solutions algorithm is systematically arranged as in Figure 5.5 refer to the previous work from Porez et al. (2014a) (note that a few variables in the chapter are

presented by different characters in Figure 5.5). The integrated MMS algorithm can be summarised as a function of $\mathfrak{R}$ as

$$\mathfrak{R}(X_{state}, P_{control}, f_{ext}) = (\dot{X}_{state}, N_{output}). \tag{5.30}$$

This algorithm resolves three recursive loops, and each set of equations is executed in the order of body index (presented with subscript j). The joint type is recognised by a conditional operator, b_j, and then the passive joints with $b_j=0$ follow the formulations in left side of flow chart in Figure 5.5 and treated as the forward dynamics; the active joints with $b_j=1$ follow the other side of flow chart and treated as the inverse dynamics.

The first loop is a forward recursive loop starting from the first component (body index $j=0$) of the system and ending up at the last component (body index $j=n$). The forces and moments exerted by fluid and joint model, e.g. internal torque (τ_j) on the hinges for passive joints and angular pitch accelerations ($\ddot{r}_j$), are applied as input condition in this loop. All the state dependent variables related to subsequent computing, such as transformation matrices (^iR_j), relevant velocities (^jV_j), inertia tensors (M_j), centrifugal forces (β_j) external force ($f_{ext,j}$), etc., are calculated and relocated in this stage.

Following by a backward loop from the last segment to the first one, inertia matrix (M_j^*) and centrifugal forces (β_j^*) are calculated, and the dynamic equations of each segment can be summed up together. The linear and angular accelerations of the reference body ($^0\dot{V}_0$) can then be computed accordingly with a transformed type of Newton's Second Law.

The third loop computes accelerations ($\ddot{r}_j$) of the passive joints and torque (τ_j) applied

on the actuated joints, which are the expected outputs of this algorithm. The global

movement velocity presented by the reference segment ($^0V_0$) and the angular position

and velocity (r_j and $\dot{r}_j$) can be obtained and allow updating the external state before

beginning the next iteration.

The detailed recursive steps are illustrated as below:

a) *The First Forward Recursion on the Kinematics*

From the available current robot state (X_{state}), the algorithm starts by the following

forward recursion:

```
For j=0, 1, …, N, compute:
```
- The matrices for frame transformation, ^iR_j, ^iP_j , ^eT_j

  and $Ad_{^jg_i}$, in Eq. (5.3), Eq. (5.4), Eq. (5.5) and Eq.

  (5.7);

- The velocity vector, ^jV_j, in Eq. (5.6);

- The acceleration term, ς_j, in Eq. (5.10);

- The inertia tensor, M_j, in Eq. (5.14);

- The body Coriolis and centrifugal forces β_j from Eq.

  (5.13);

- The external forces $f_{ext,j}$ from FLUENT Solver.

```
End for.
```

b) *The Backward Recursion on the External Forward Dynamics*

Once all the state-dependent variables are known, the next step of the computational

algorithm consists in executing the following recursion:

```
For j=N, N-1, …, 1, compute:
If b_j=1:
```

- The generalised inertia matrix $\mathbf{M}_j^*$ from Eq. (5.17);

- The generalised inertia matrix β_j^* from Eq. (5.18);

```
Else (if b_j=0):
```

- H_j from Eq. (5.23);

- κ_j from Eq. (5.27);

- α_j from Eq. (5.28);

- The generalized inertia matrix $\mathbf{M}_j^*$ from Eq. (5.25);

- The generalized forces β_j^* from Eq. (5.26);

```
End for.
```

Once the recursion loop is carried out, compute the accelerations, ${}^iV_i$, from Eq. (5.19).

c) *The Second Forward Recursion on the Internal Dynamics*

Finally, the algorithm ends with a second forward recursion initialised by the current state and ${}^0\dot{V}_0$:

```
For j=1, 2, …, N, compute:
If b_j=1:
```

- The acceleration of body from Eq. (5.9);

- The torque τ_j from Eq. (5.21);

```
Else (if b_j=0):
```

- The acceleration of hinge angle $\ddot{r}_j$ from Eq. (5.23);

- The acceleration of body from Eq. (5.9).

End for.

The detailed formulas are well documented in a publication of Porez et al. (2014a). This method is successfully implemented on movement prediction of a fish robot model constructed by 8 linked rigid segments and a bird robot model as a tree like system with a few rigid and elastic segments (Porez et al., 2014a; Porez et al., 2014c) coupled with a classic analytical hydrodynamic model (the large amplitude elongated body theory). This hybrid algorithm for MMS model can minimize computational complexity and save execution time, and offer a simple access to couple with the fluid field by the well-arranged recursive loops.

5.3 Coupling with Fluid Solver

After the derivation of governing equations of MMS model, the external force and moment terms in these equations are required to be obtained from the fluid solver. Similar to the previous chapters (Chapter 3 and Chapter 4), the CFD package ANSYS-FLUENT (version 14) is used as the fluid solver, and the MMS algorithm is embedded in FLUENT solver by using an in-house User Defined Function (UDF) written with C language. The interactive data transferring between two solvers are the instantaneous fluid forces and moments and kinetic motions of elements. The detailed algorithms are described as in the following sub-sections.

5.3.1 Fluid Solver

The governing equations for the FLUENT solver are the two-dimensional continuity and momentum equations for incompressible viscous fluid, which have been presented in Chapter 2 as Eq. (2.1). The Dynamic Mesh and UDF function are

activated for calculating and capturing the body motions. The forces and moments that exerting on moving surfaces by surrounding fluid are expressed in terms of the integrated pressure and viscous stress, and both of them are taken into account at every time step in this study.
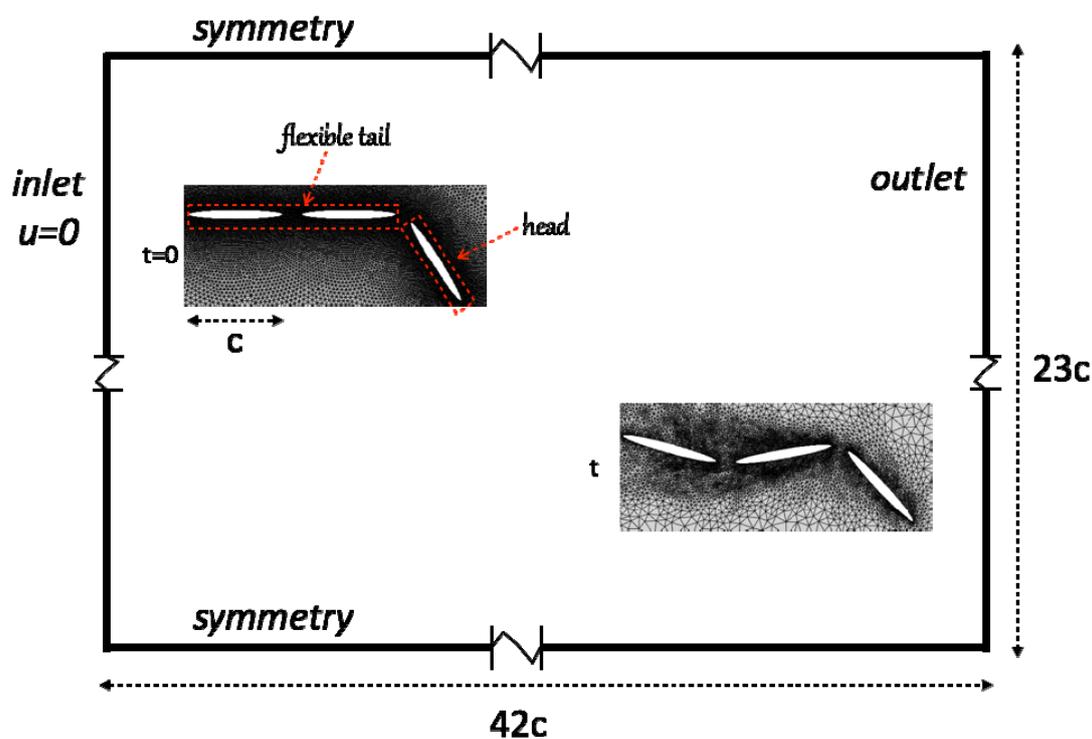
Figure 5.6 Information of domain size, mesh quality and boundary conditions.

The boundary condition on the rigid segment surface is set as no slip wall, an inlet velocity is defined on the left side of computational domain, and a pressure outlet is applied on the right boundary as shown in Figure 5.6. Regarding to the dynamic mesh method, the re-meshing and smoothing parameters are both chosen carefully. The re-meshing is accomplished by the local cell method, and the smoothing process is done with a diffusion function. The parameters applied are all well tested by a mesh density independent test.

All the settings for fluid solver are based on the availability of schemes of ANSYS-FLUENT package. A 2D pressure-based transient fluid solver is selected, and the fluid field is set as laminar viscous model. Fractional-Step Method (FSM) scheme is activated under pressure-velocity coupling panel. With FSM scheme, the

momentum equations are decoupled from the continuity equation using a mathematical technique called approximate factorization. The formalism used in the approximate factorization allows controlling the order of splitting error, hence improves the robustness of solutions with moving boundaries. The spatial discretization of both pressure and momentum are with the second order upwind accuracy.

Comparing with previous flapping wing models with non-deformable structured mesh, a treatment of dynamic mesh is applied on this model for enabling the moving-deforming mesh simulation. A high quality triangular mesh is generated for the simplification of pre-processing procedure and also for the convenience of activating smoothing and re-meshing function. During the simulation, the mesh quality is evaluated at every time-step, and both smoothing and re-meshing schemes are adapted to update the mesh to meet the resolution requirement. The re-meshing is accomplished by local cell method, which recognises and re-meshes the cells based on a few parameters, e.g. cell skewness and minimum/maximum length scales. The smoothing process is done with a diffusion function, which relocates the boundary node position according to the vertex geometric centre. The mesh of a test model is illustrated in Figure 5.7 that the mesh quality remains very well around boundary surface after undulating 20 periodic cycles and moving to a location that is $25c$ (c is chord length of individual segment) away from the initial position, although the surrounding mesh turns coarser comparing to the initial stage. In the test case, there are 300 cells distributed along each segment surface and the time-step size is selected as $0.001T$, which are adequate enough for accurate simulation at relatively low Reynolds number condition without flow separation phenomenon.

(a)

(b)
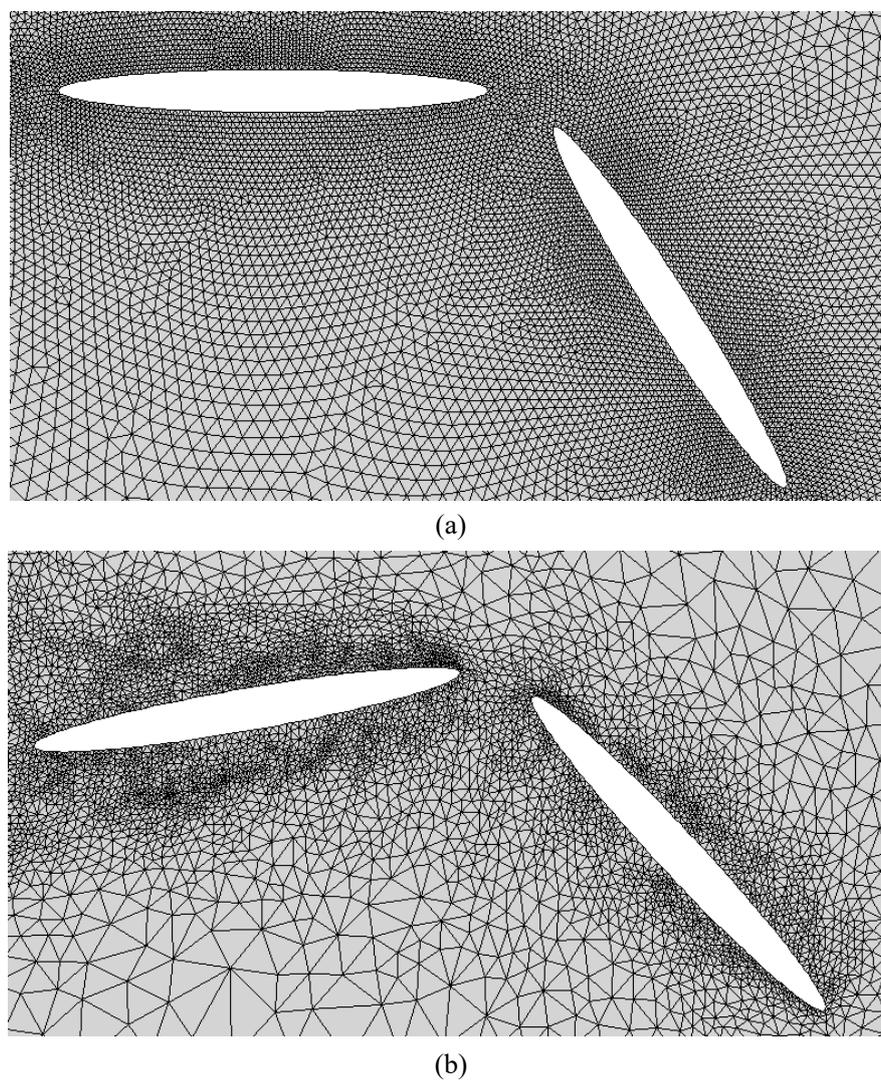
Figure 5.7 Comparison between (a) initial mesh and (b) deformed mesh of two segments after 20 periodic cycles.

5.3.2   Coupling Algorithm

The coupling process between MMS algorithm and fluid solver is made through an interactive data transferring between two solvers with fluid forces and moments (f_{ext}) of fluid solver and statement vector (X_{state}) of MMS model. Basically, the simulation iteration loop starts from updating the imposed position which is available from the last time step, and fluid domain is solved for obtaining hydrodynamic forces and

moments, and then with the fluid forces and moments as input conditions, the multi-body dynamic solver calculate updated position for next time step.

Specially, before the next time step starts, a fourth-order predictor and fifth-order corrector explicit time discretization method of Eq. (5.31) is utilized to achieve an accurate solution of the MMS statement vector.

$$
\begin{aligned}
\dot{X}_{state}\big|_n &= \Re(X_{state}\big|_n, P_{control}\big|_n, f_{ext}\big|_n) \\
X_{state}\big|_{pre} &= X_{state}\big|_n + \left(\tfrac{23}{12}\right)\dot{X}_{state}\big|_n \Delta t - \left(\tfrac{16}{12}\right)\dot{X}_{state}\big|_{n-1}\Delta t + \left(\tfrac{5}{12}\right)\dot{X}_{state}\big|_{n-2}\Delta t \\
\dot{X}_{state}\big|_{cor} &= \Re(X_{state}\big|_{pre}, P_{control}\big|_{(n+0.5)}, f_{ext}\big|_n) \\
X_{state}\big|_{n+1} &= X_{state}\big|_{pre} + \left(\tfrac{9}{24}\right)\dot{X}_{state}\big|_{cor}\Delta t + \left(\tfrac{19}{24}\right)\dot{X}_{state}\big|_n \Delta t - \left(\tfrac{5}{24}\right)\dot{X}_{state}\big|_{n-1}\Delta t + \left(\tfrac{1}{24}\right)\dot{X}_{state}\big|_{n-2}\Delta t
\end{aligned}
. \quad (5.31)
$$

In current study, it is not achievable to conduct fully iterated correction between fluid solver and MMS algorithm simultaneously due to a limitation of the FLUENT package that the hydrodynamic forces and moments can be calculated only once during each time step. Therefore to ensure the computational accuracy, the iteration is employed on the execution procedure of MMS algorithm using criteria of $\dot{X}_{state}$ so that an accurate motion can be achieved from MMS solutions, and hence the fluid solver can work out an accurate hydrodynamic forces and moments accordingly.

Moreover, to ensure the robustness for any choice of body mass, a method of identifying and adding a virtual fluid inertia matrix to the body inertia is applied. This approach extends a similar approach used by both Shiels et al. (2001) and Eldredge (2008).

5.4 Validation and Verification

To assess the reliability of our coupling method with both MMS algorithm and CFD solver, two validation cases, with either active joint or passive joint models, are carried out for verification. In a sum, the results agree well with the previous

numerical work. In addition to these two test cases, another case with active hinges controlled by external torque instead of prescribed angle is also tested, and it shows that the algorithm is feasible for various control methods and reversible between the transformation of angle controlling system and torque controlling system. The computational details are presented in the following sub-sections.
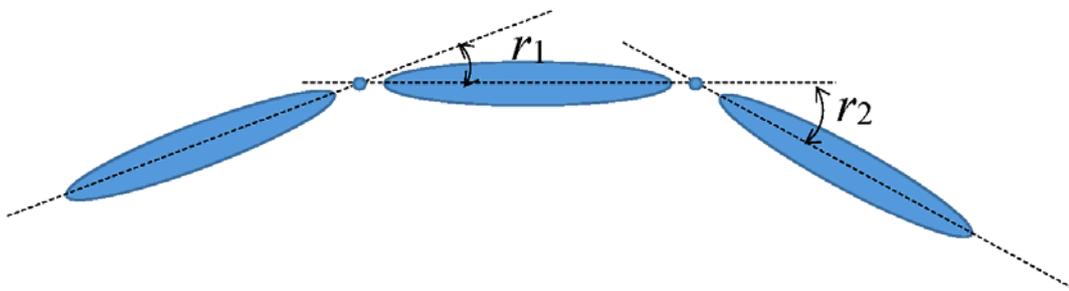
Figure 5.8 Schematic of three linked rigid bodies.

5.4.1 Validation of Actuated Joint Model

This case validates the right part (Figure 5.5) of the MMS algorithm for a system with active hinges controlled by prescribed angles. Following the previous work of Eldredge (2008), the model is built as a massless articulated system consisting three linked rigid bodies and the two joints (Figure 5.8). The rigid bodies have identical elliptical section area of aspect ratio 0.1 with chord length c, and the distance from tip to hinge is set to $0.1c$. Each hinge between the pair of the rigid bodies is independently controlled, with the prescribed angle as

$$
\begin{aligned}
r_1(t) &= -\cos(t - \frac{\pi}{2}), \\
r_2(t) &= -\cos(t).
\end{aligned}
\tag{5.32}
$$
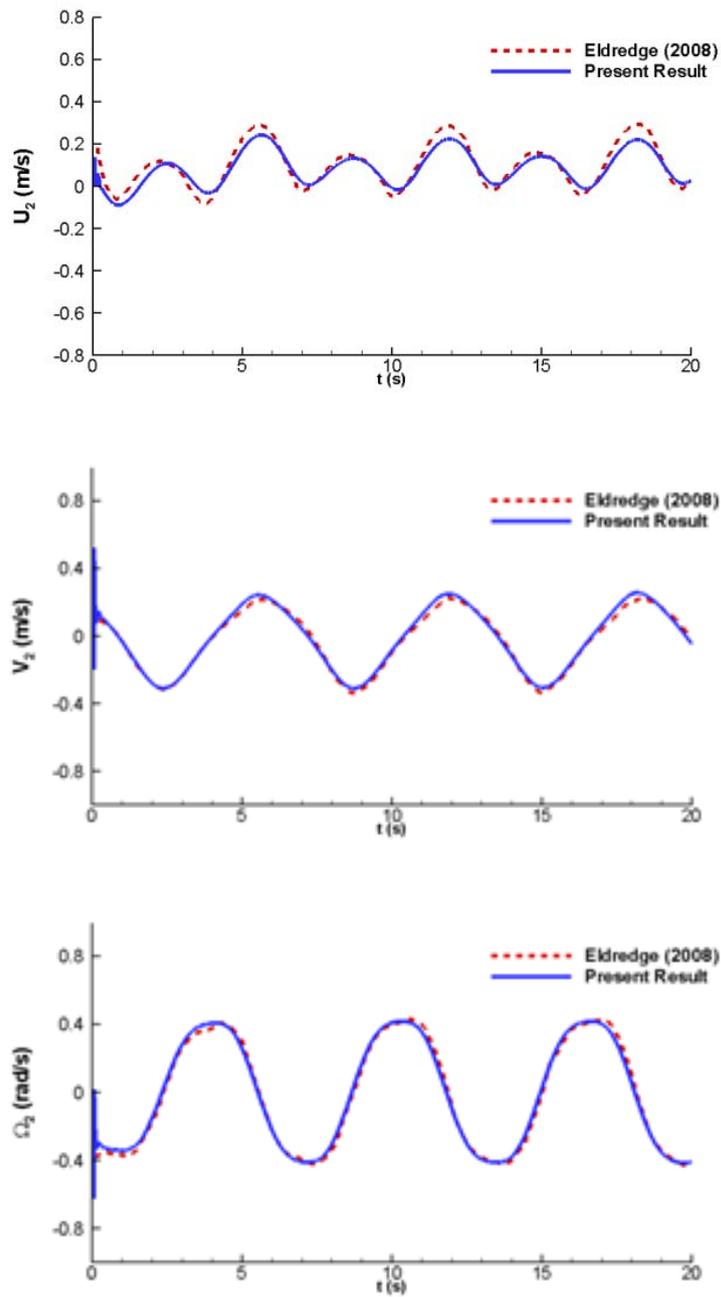
Figure 5.9 Comparison with the results of Eldredge (2008) on the *x*- and *y*- velocity components and angular velocity.

t=0. 8T

t=1. 6T

t=2. 39T
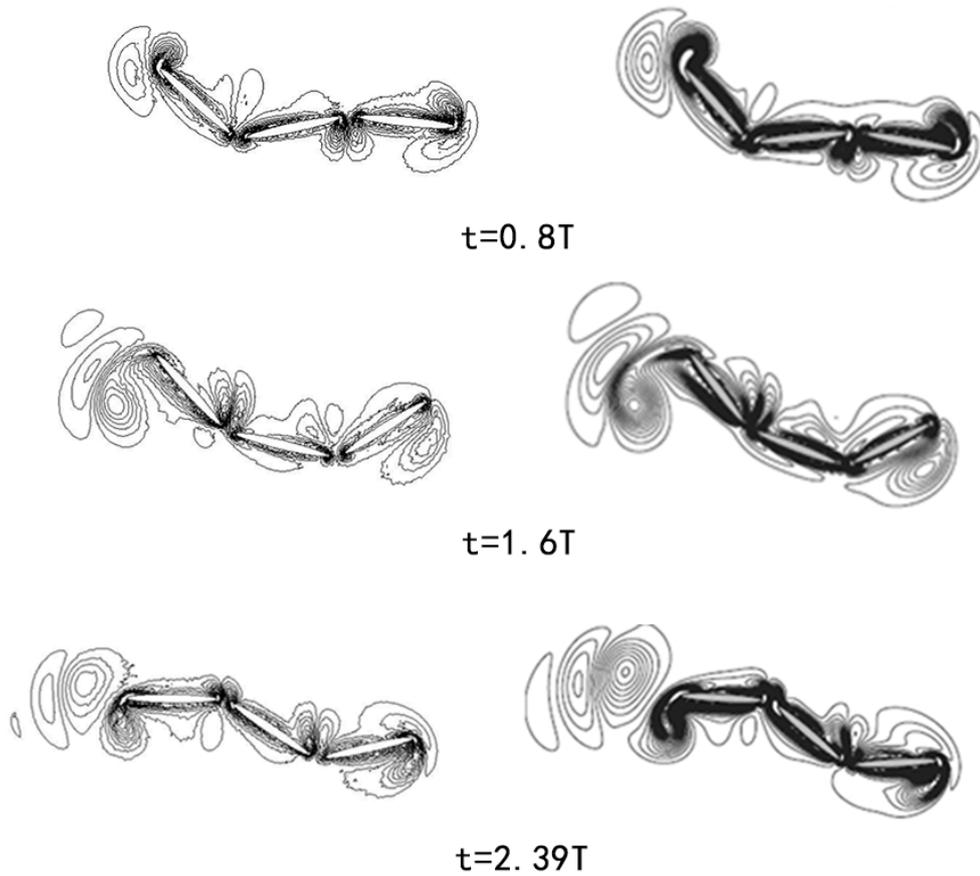
Figure 5.10 Comparison with the results of Eldredge (2008) on vorticity structures. The left column is from current results and the right column is from the literature.

The entire linked system has 3DoF in x, y and pitching directions, i.e., it is free to move in all directions in two dimensions under propulsion of linked segments controlled by prescribed angles. An undulation Reynolds number, fixed at 200, can be defined from the peak angular velocity of intersection angle as

$$\mathrm{Re} = \frac{\dot{r}_{max} c^2}{\upsilon},$$ (5.33)

where υ is the fluid dynamic viscosity. The results are well matched with Eldredge (2008) in translational velocity components, angular velocity and vortex structures, as shown in Figure 5.9 and Figure 5.10, respectively. In Figure 5.9, U_2, V_2 and Ω_2

represent the horizontal velocity, vertical velocity and the angular velocity of the middle body.

5.4.2   Validation on Passive Joint Model

To validate the left part of the algorithm (Figure 5.5) for passive joints, the model with two rigid segments linked by a torsional spring as shown in Figure 5.11 is simulated. The upper body has been imposed with sway and pitch motion, and the motion of the lower body is governed by fluid forces and constraint of the linked hinge. This case has been well illustrated in the previous work from Toomey and Eldredge (2008). Our results of the induced angle and the fluid forces agree well with numerical simulations as shown in Figure 5.12.
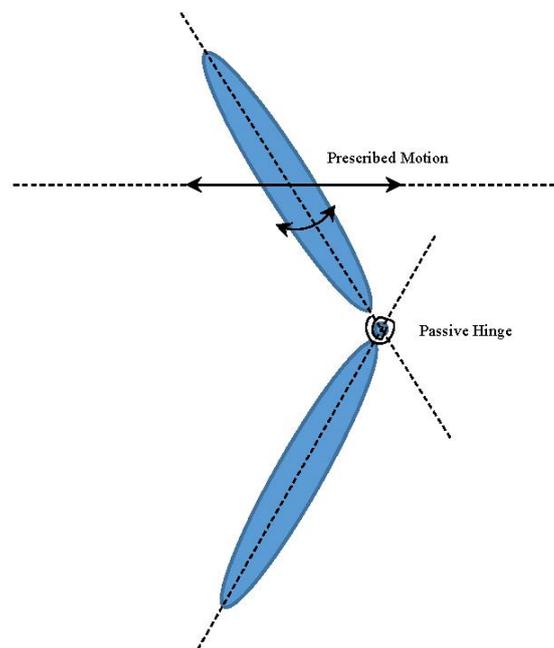
Figure 5.11 Schamtic of two linked bodies with a passive hinge.
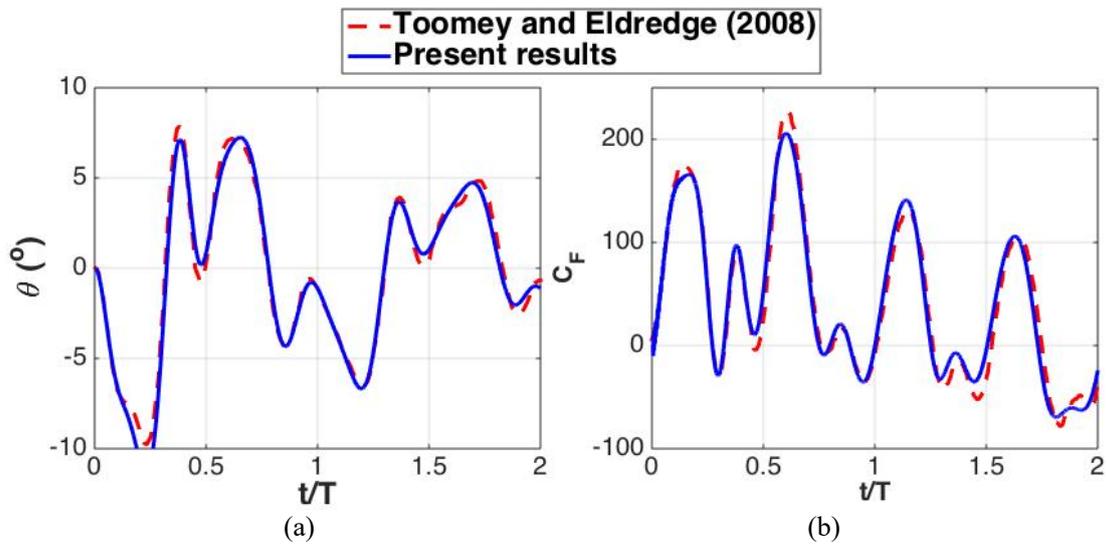
Figure 5.12 Comparison with Toomey and Eldredge (2008), (a) induced angle (θ) at the passive joint (b) dimensionless total lift force of the entire system (C_F).
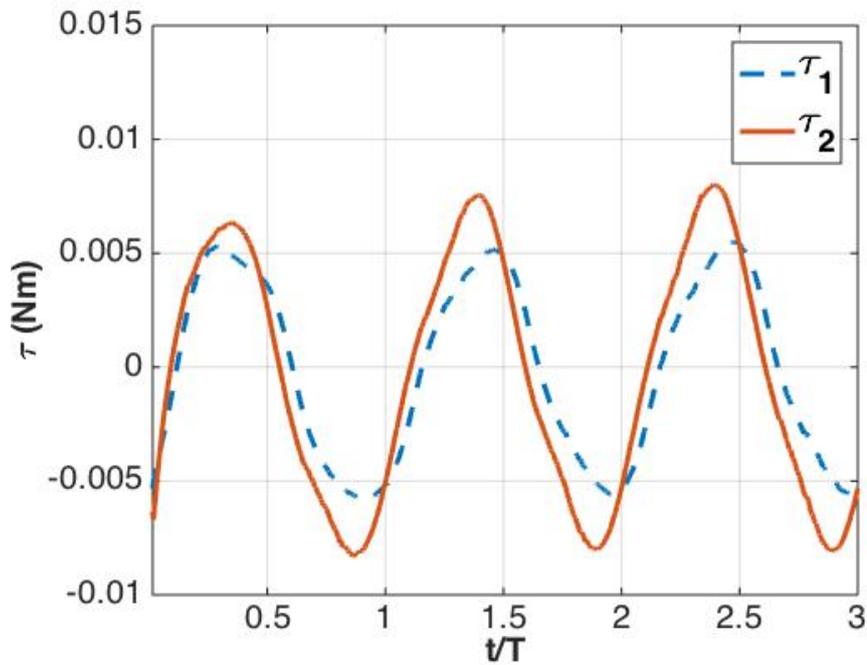
Figure 5.13 External torques applied on the hinges.

5.4.3   Controlled by Torque

For verifying the feasibility of the algorithm applications on different control systems, a case is tested with a model of the same geometry as the validation case in Sec. 5.4.1, while with hinges controlled by external input torques instead of angles. The multi-body system is allowed to move freely in the water. The torques obtained from the validation case in Sec. 5.4.1, as shown in Figure 5.13, is applied on the joints as the external input torques.
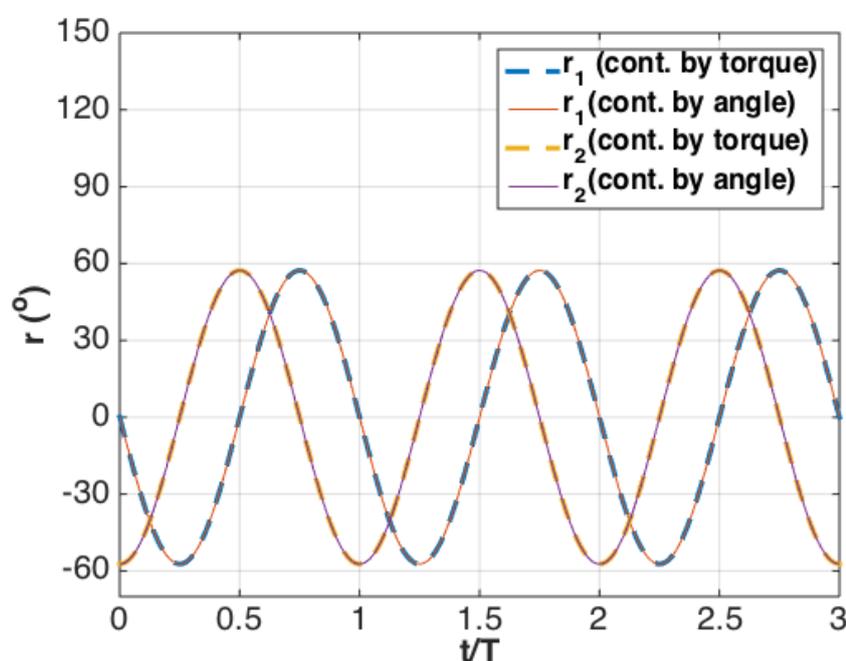
Figure 5.14 Comparison of results of induced and prescribed angles at hinges between approaches of torque controll and angle controll.

The results show that the induced angle is exactly the same as the prescribed sinusoidal profiles (Figure 5.14). The understanding of this test is twofold: the algorithm is capable for models with joints using torque control system; the algorithm is reversible between different ways of control with angle and torque. The kinetic motion of the multi-body system is a consequence of coupling interaction with internal dynamics and external fluid forces. Once a certain amount of torque is imposed, the fish body turns to expected posture with the help of internal constraints

under interactions with external environment. There have been previous research studies on exploring the mechanism of internal muscular forces (Altringham and Ellerby, 1999; Long, 1998; Tytell et al., 2010). The fish motion can be easily captured by camera with experimental observation, however the internal muscle forces are hardly caught. An inspiration obtained from this test case is that the coupled simulation of MMS algorithm and fluid solvers may be a possible way to estimate the internal forces and moments required for achieving a certain posture when the movement and muscle elastic properties are known.

5.5 Test Case – a MMS Model with Three Rigid Components

The work in the previous chapters has indicated that the pitch flexibility can affect the hydrodynamic performance of wing-like system, and there have been applications with this mechanism on propulsion and energy harvesting of renewable energy device (Xiao and Zhu, 2014) and biomimetic robot design (Shyy et al., 2007) with proper designs. In this section, a MMS model is simulated with both passive and active joints, aiming to investigate the tail flexibility effect on propulsion, where the tail flexibility is realised by applying different spring stiffness and damping coefficients at passive joint, and the analysis is made from the hydrodynamic points of view with considerations of fluid forces exerting on the model components, power consumption, and efficiency as well as vortex structures.

Current model has the same geometry as the case in Sec. 5.4.1, shown in Figure 5.8. We assume that the left two rigid bodies mimic fish tail with flexibility consisting of a passive joint in the middle, and the right rigid body is fish body with an active joint as the tail peduncle. There is a prescribed pitch angle between fish body and tail at the peduncle joint, mimicking tail that flaps to propel the entire body. This prescribed

relative motion between head and tail is same as r_2 in Sec. 5.4.1. The passive joint is a stiffness-damper spring, governed by Eq. (5.34), where R^* and K^* are damping and stiffness respectively.

$$\tau = -R^* \dot{r} - K^* r \qquad (5.34)$$
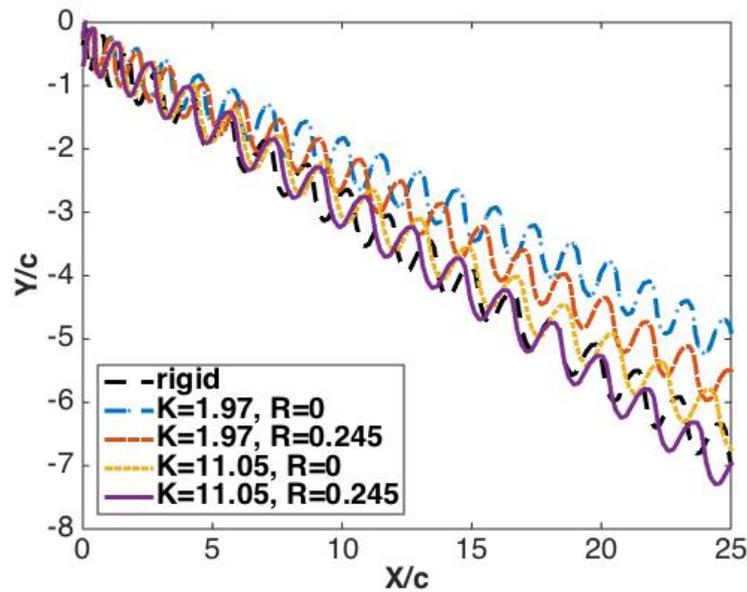
(a)
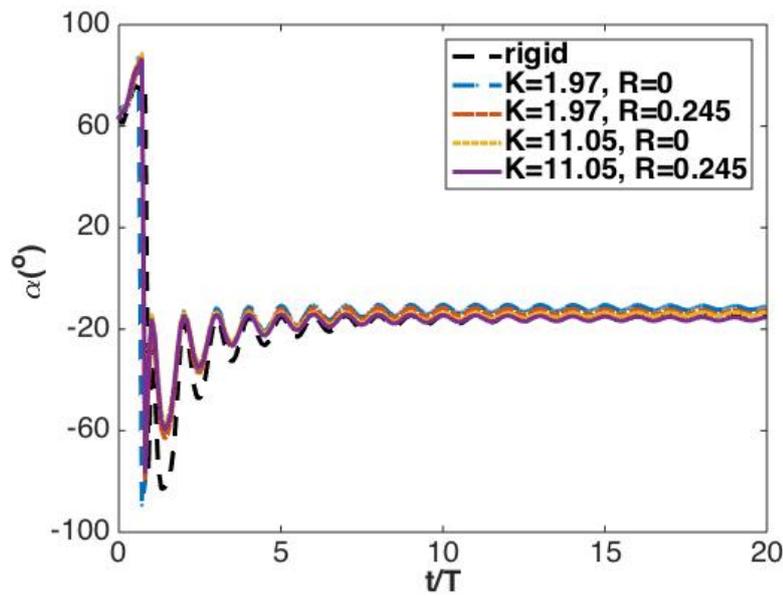
(b)

Figure 5.15 (a) Trajectory of the entire system tracked by the location of the active joint (b) Orientation angle of the motion trace [$\alpha = \mathrm{atan}(Y/X)$].

The damping and stiffness can be represented by the non-dimensional coefficients as

$$R = R^* / (\rho f c^4), \tag{5.35}$$

$$K = K^* (\rho f^2 c^4), \tag{5.36}$$

where f is the flapping frequency. Referring to the stiffness and damping coefficients selected by Toomey et al. (2010), K and R vary between 5.1 to 51.4 and 0.2 to 0.7 respectively.

In the current study, the parametric test is carried out with combinations of six stiffness coefficients (varying from 1 to 27) and two different damping coefficients (0 and 0.245). The smaller stiffness leads a softer tail. One more case with rigid tail is also included as a baseline for comparison. The rigid tail is designed by prescribing a zero pitch angle on the passive joint all over the cycles.

5.5.1   Locomotion Trajectory

The trajectory of entire system and instantaneous induced angle at the passive joint are the most desired kinematic quantities and can be directly measured from the simulations. As shown in Figure 5.15 (a), the trajectory is tracked by monitoring the location of the hinge joint between articulated fish body and tail, i.e. the position of the active joint. The fish motion starts in quiescent flow condition, and accelerates gradually into a quasi-steady stage under undulatory propulsive motion. The induced motion of the system follows a zig-zag trace, and moving direction is determined mainly by phase shift of the induced pitch at passive joint under different stiffness and damping coefficients. The orientation angle (α) of the motion trace line shown in Figure 5.15 (b), presenting the moving direction within global coordinate, is quantified by inverse tangent formula [α=atan(Y/X)] using the trajectory in Figure 5.15 (a).

As plotted in Figure 5.15, the induced motion reaches the quasi-steady status after

approximately 10 revolutions. The fish undergoes a development procedure of balancing friction force and thrust force. At start-up stage, thrust force is bigger than friction force, and causes accelerated motion. Theoretically in Stokes regime, viscous force is proportional to moving velocity, so the viscous force and thrust force can balance with each other when the velocity is big enough, then leads to a stable quasi-steady stage. Although the studies on start-up stage is of importance to understand mechanisms of manoeuvrability and stability, the result analysis in the following sub-sections will mainly focus on the fully developed stage. The average values of the variables yielding global analysis can provide a general view of the induced locomotion under specific undulatory body posture. It is noted that velocities and forces in the following sub-sections are all transformed in semi-local coordinates with axis along travelling direction and perpendicular direction, which are decided by average induced angle [average α in Figure 5.15 (b)] in the quasi-steady stage.

5.5.2   Induced Velocity

The velocity components, V_x and V_y, are presented in the traveling direction and the perpendicular direction respectively. The instantaneous velocities in quasi-steady stage with selected combinations of stiffness and damping coefficients are plotted in Figure 5.16. It is shown that all the amplitudes, mean values and phases of V_x vary with the parameters, while the amplitudes of V_y are slightly different with mean value remaining zero. In addition, the phase difference of V_x is a consequence of the phase shift of the induced pitch motion at the passive joint.
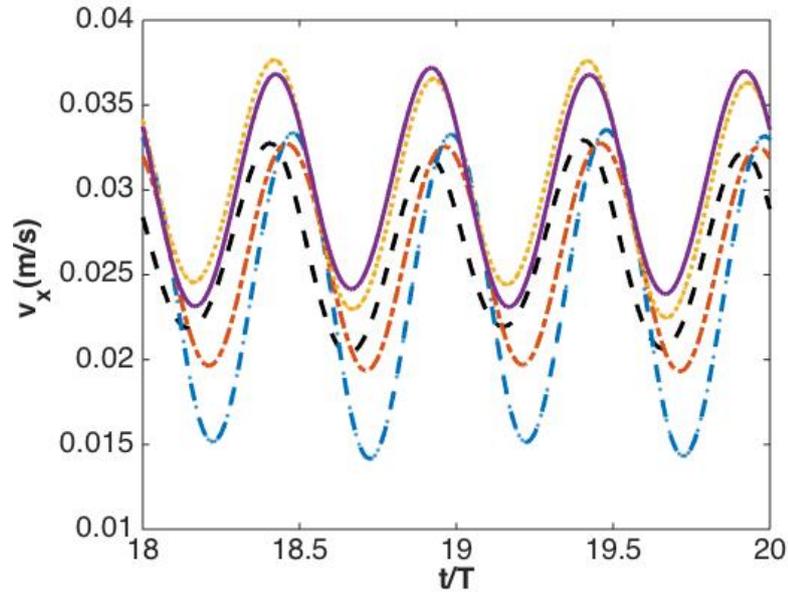
(a)
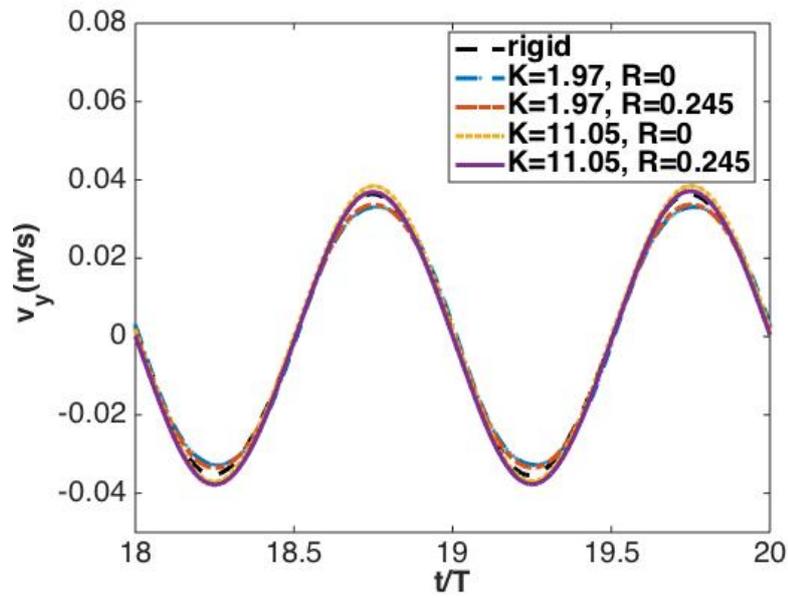
(b)

Figure 5.16 Instantaneous velocities in a semi-local coordinate, poining to (a) travelling direction and (b) perpendicular direction.
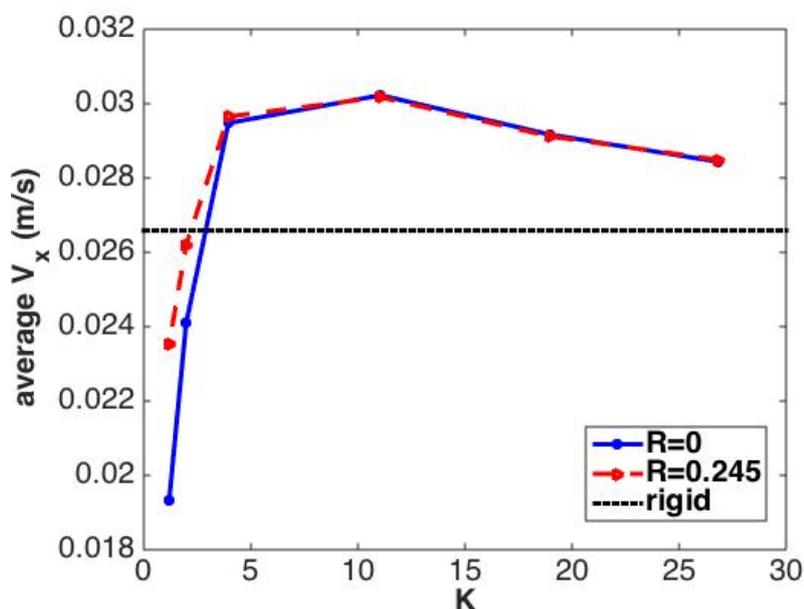
Figure 5.17 Average velocity in travelling direction with different stiffness and damping
coefficients.

V_x is one of the most important variables that used to measure the propulsive
performance. Therefore, the average V_x is calculated and plotted as in Figure 5.17. It
can be seen that the mean travelling velocities increase dramatically when stiffness
coefficient is below 3.95, and decrease gradually after a mild rise to the peak point. The
effect of damping coefficient on the induced velocity is dependent on stiffness
coefficient. The average velocities are larger with damper applied when the stiffness
coefficient is smaller than 11.05, while the differences disappear when the stiffness is
bigger. It is interesting to observe that the articulated fish models in most cases travel
faster than the one with rigid tail, and there is an optimal stiffness coefficient, leading to
the fastest swimming velocity, as a result of appropriately induced angle and phase at
passive joint. The increase of velocity with flexible tail agrees with findings in the
previous work from Bergmann et al. (2013), in which similar findings have been
obtained through examining caudal fin elasticity effect by changing lumped
parameters.
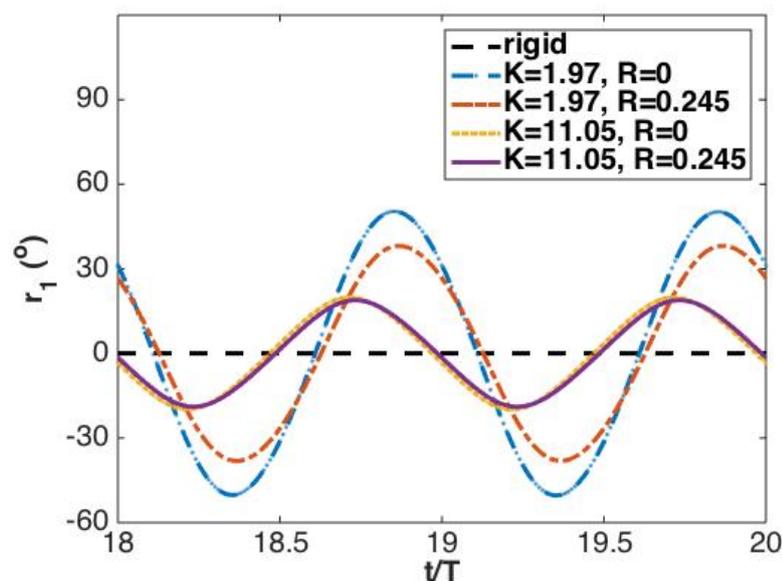
Figure 5.18 Instantaneous induced angle at passive joint (within the undulatory cycle from 18 to 20).

5.5.3 Induced Pitch Angle at Passive Joint

The instantaneous induced angles at passive joint (r_1) under selected parameters are shown in Figure 5.18. The angles are periodic in each revolution, so the amplitude (r_{amp}) and phase (ϕ) are arranged in Figure 5.19 for exploring the trends under different parameters. It can be seen that the stiffness plays an important role on both r_{amp} and ϕ. It is reasonable that r_{amp} is bigger when the joint is less stiff, though a spike occurs when the joint stiffness is further reduced. All r_{amp} are smaller than the imposed angle amplitude (57°) at the active joint. The phase (ϕ) decreases with bigger stiffness, and it shows that the induced motion turns to be more consistent with the active motion when the tail is stiffer. With damper applied, the induced angle has smaller amplitude, and the impact of damping coefficient on r_{amp} is dependent on the stiffness, that the difference of r_{amp} with or without damper turns to be smaller when the joint stiffness becomes bigger. The damper cause delayed action of the passive joint, and lead to a bigger phase change.
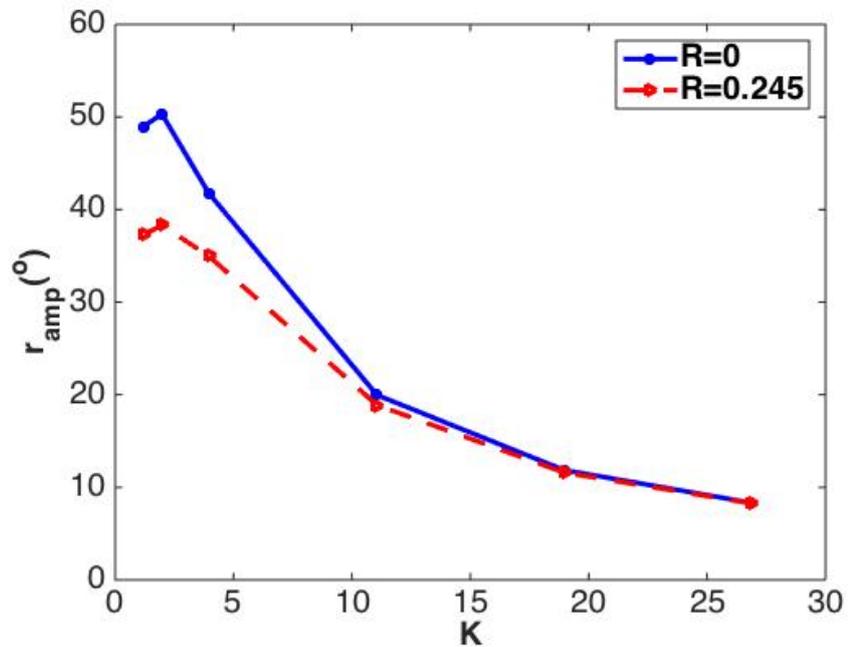
(a)
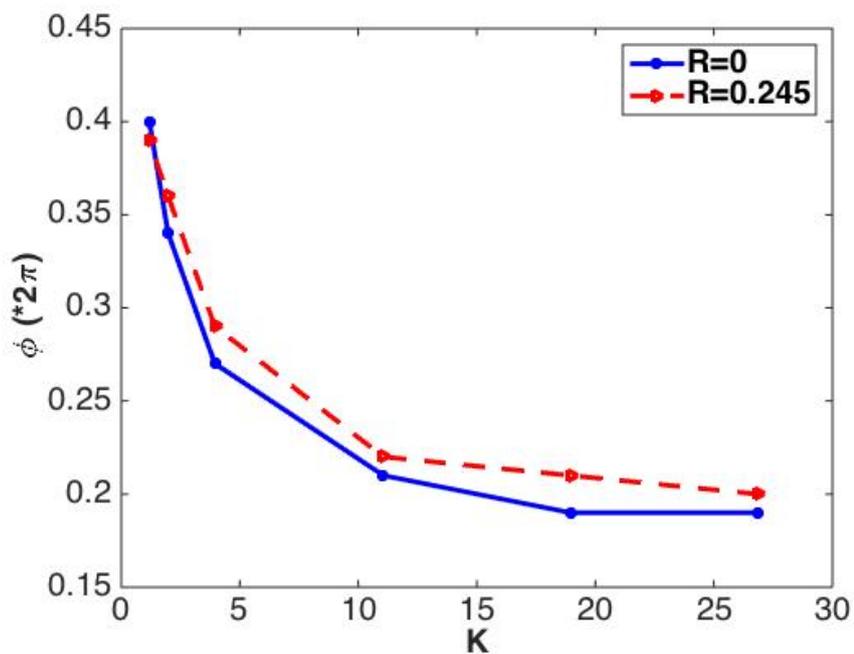
(b)

Figure 5.19 (a) Amplitude (r_{amp}) and (b) phase shift (ϕ) of induced pitch angle.

The induced angle at passive joint is always a result coupling with external surrounding

fluid and internal elements. It is noticed that the flexibility of the spring determines whether the induced pitch is dominated by internal or external variables at the passive joint. One example for internal properties domination is that when the spring stiffness is big enough, especially in the case of the rigid tail, there is no relative pitch motion induced between two connected rigid components. The external environment takes in charge of the induced motion when the spring stiffness is small, such that in a case with the passive joint as a fully revolute joint with no stiffness and damping, the soft part of the tail would just follow the fluid pattern generated by wake structure and bypass flow. This can explain the observation in Figure 5.19 (a) that the induced angle turns smaller before and after the stiffness coefficient (K) of 1.97, as it transfers from external dominating condition to internal dominating conditions.

5.5.4 Fluid Forces and Moments

The instantaneous fluid forces acting on the rigid components under selected parameters are plotted in Figure 5.20. The average forces in both travelling and perpendicular directions are approximately zero at the quasi-steady stage. The swimming mode falls in a low Reynolds region. The amplitudes of pressure forces (F_{px} and F_{py}) are bigger than those of viscous forces (F_{vx} and F_{vy}), but both of them are within the same magnitude scope. The middle body always has the biggest pressure force comparing with the other two. When the induced pitch at passive joint is less excited as a consequence of bigger stiffness, the pressure force reduces dramatically, while the viscous force remains the same.

The instantaneous torque history are plotted in Figure 5.21, where τ_1 is restoring torque induced by the interactions of the elements and fluid, and τ_2 is input torque produced by electric actuator motor at active joint. τ_1 is obtained from the stiffness-damper spring equation, and τ_2 is an output from the function $\mathfrak{R}$. The torque curves are periodic and phase shift exist, the average torque is approximately zero, and the amplitude mainly depends on the stiffness. It can be observed from Figure

5.22 that the torques of active joints are bigger than those of passive joints, and all of them increase dramatically before reaching a flat level with increased spring stiffness. The torques of both active and passive joints are slightly bigger in the cases with flexible tails than those with rigid tail.
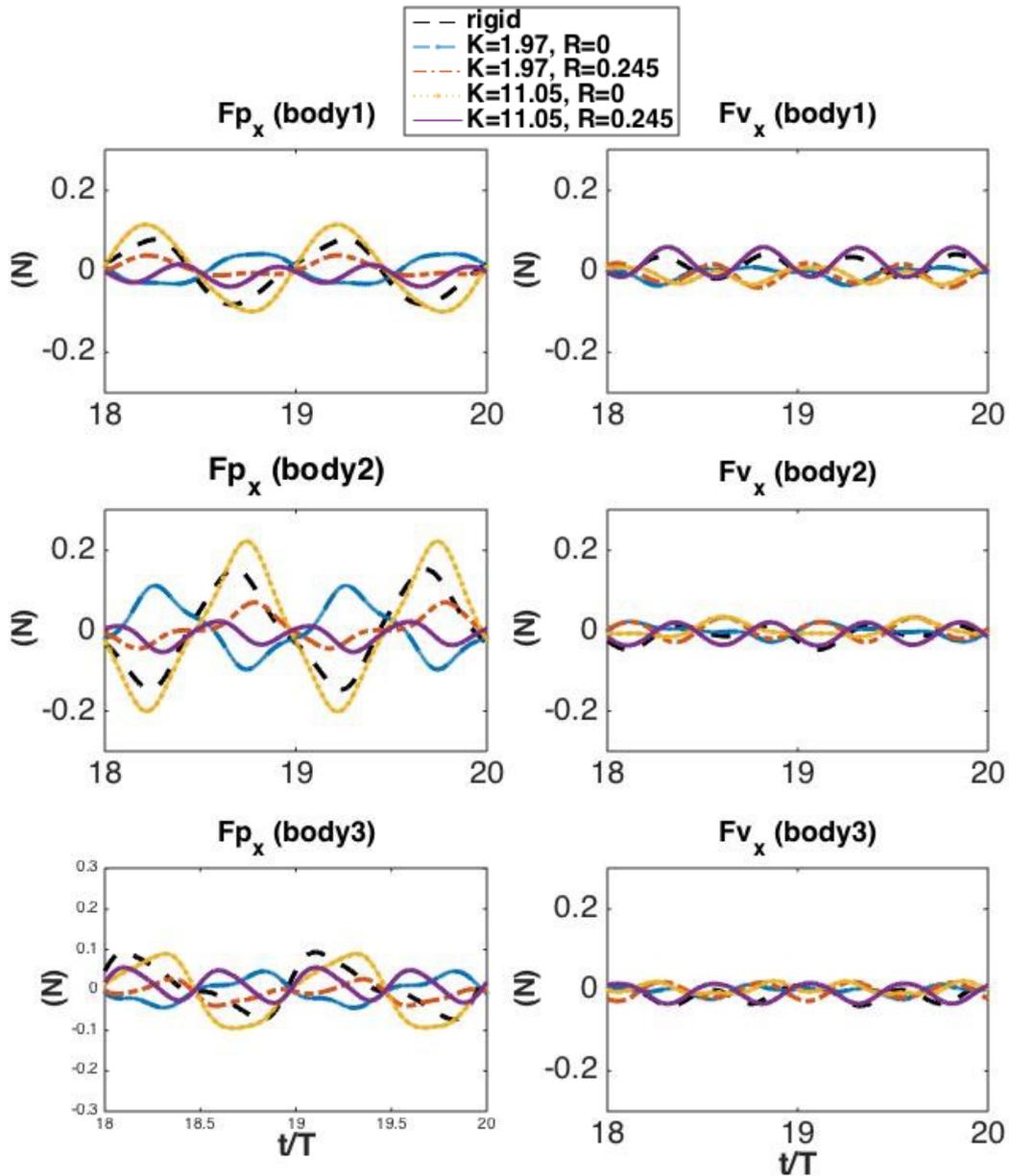
(a)

(*To be continued.*)
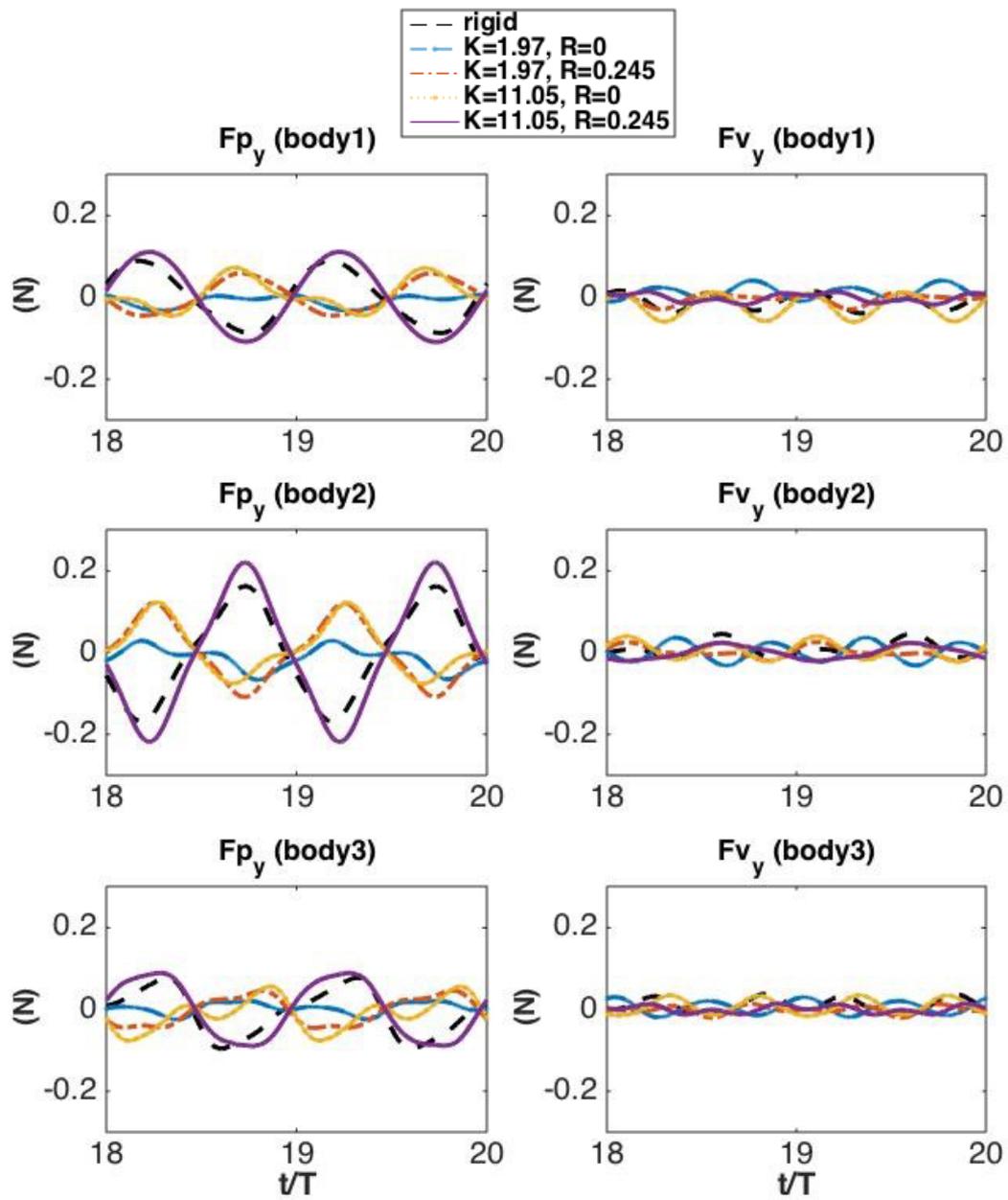
(b)

Figure 5.20 Instantaneous pressure and viscosity fluid forces over each rigid segment (a) in travelling direction and (b) perpendicular direction.
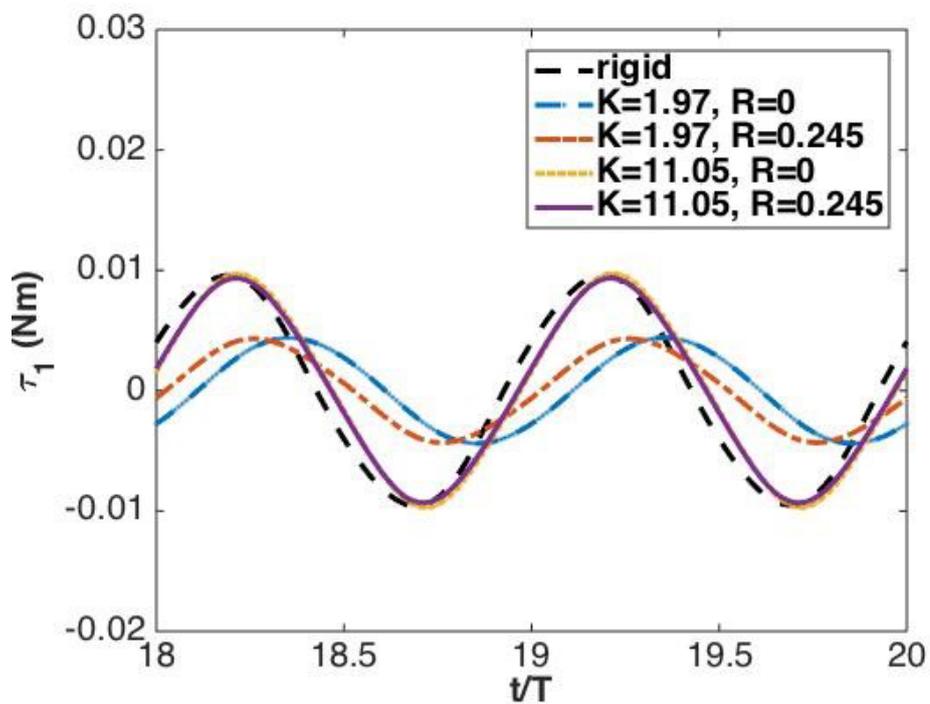
(a)
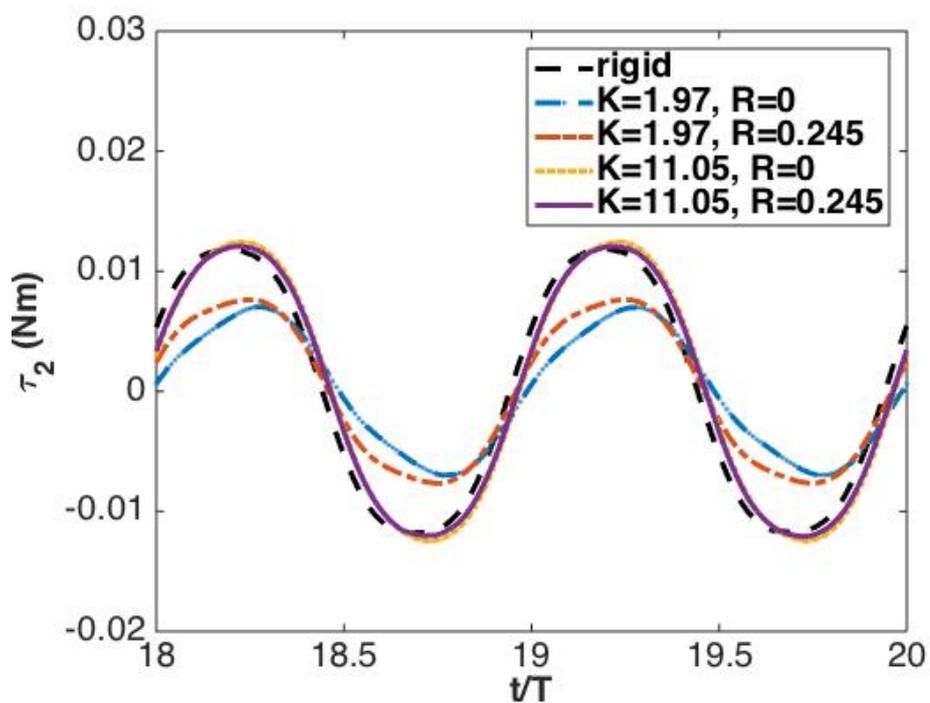
(b)

Figure 5.21 Torque history (a) at passive joint (τ_1) and (b) at active joint (τ_2).
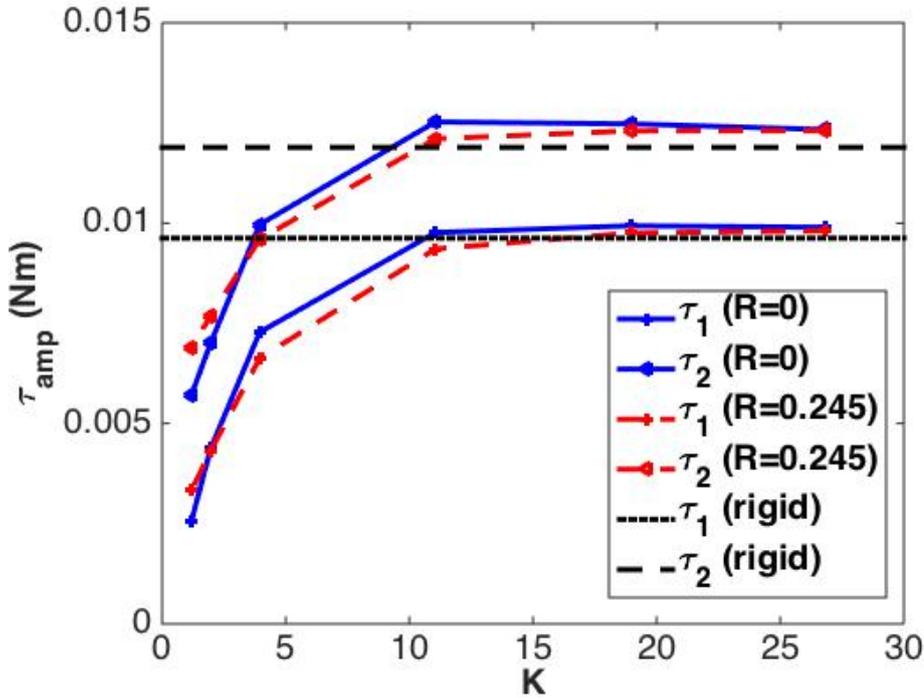
Figure 5.22 Torque amplitude under different parameters.

5.5.5 Power

The power can be used to quantify energy consumed for propulsion. In the current multi-body system model, the power applied at active joint is the only input energy resource, which contributes to the kinetic motion and can be consumed by the induced motion at passive joint only when damper is considered. The power, P, is calculated as in Eq. (5.37), power history is plotted in Figure 5.23, and average power is shown in Figure 5.24, where P_1 is power at passive joint and P_2 is input power at active joint.

$$P = \tau \cdot \dot{r}. \tag{5.37}$$

It is seen from Figure 5.23 that the power curves at passive joint have similar amplitudes, and phases shift around according to the applied parameters. The power at active joint is constantly positive and with different amplitudes. The positive and negative values denote the spring can either store power (negative P) or release power (positive P). The phase shift of power curve is a consequence of that of induced pitch

angle. The average power at the passive joint without damper is approximately zero as shown in Figure 5.24 (a), indicating the spring only store or release power without power consumption. While with damper, the average power turns negative, showing that power loss exists.
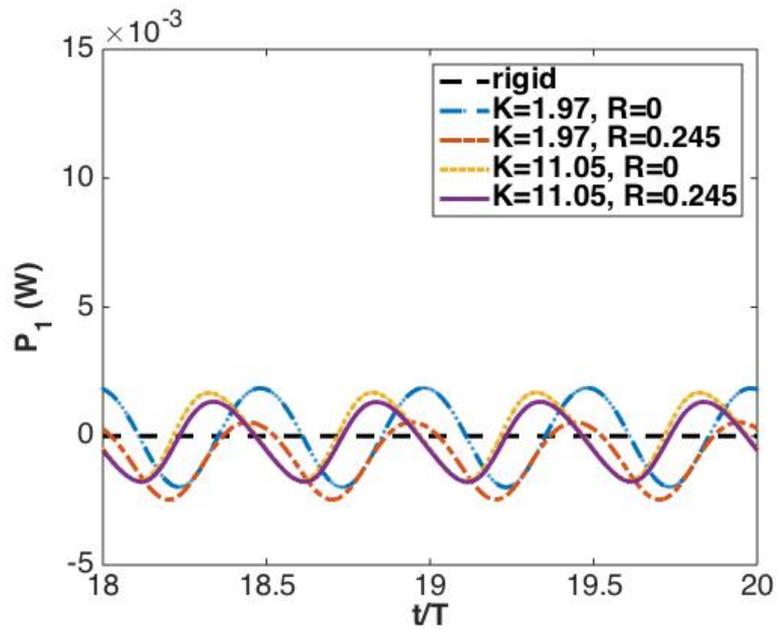
(a)
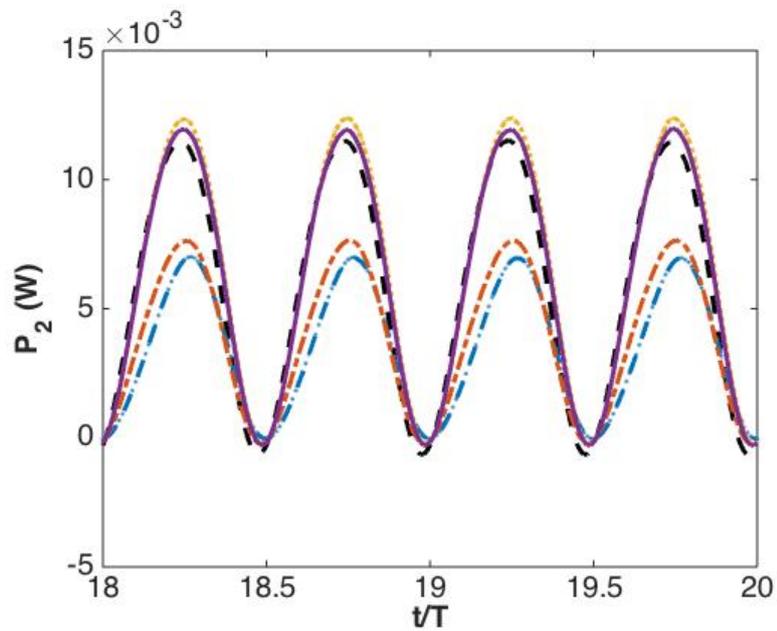
(b)

Figure 5.23 Instantaneous power applied on (a) passive joint (b) active joint.
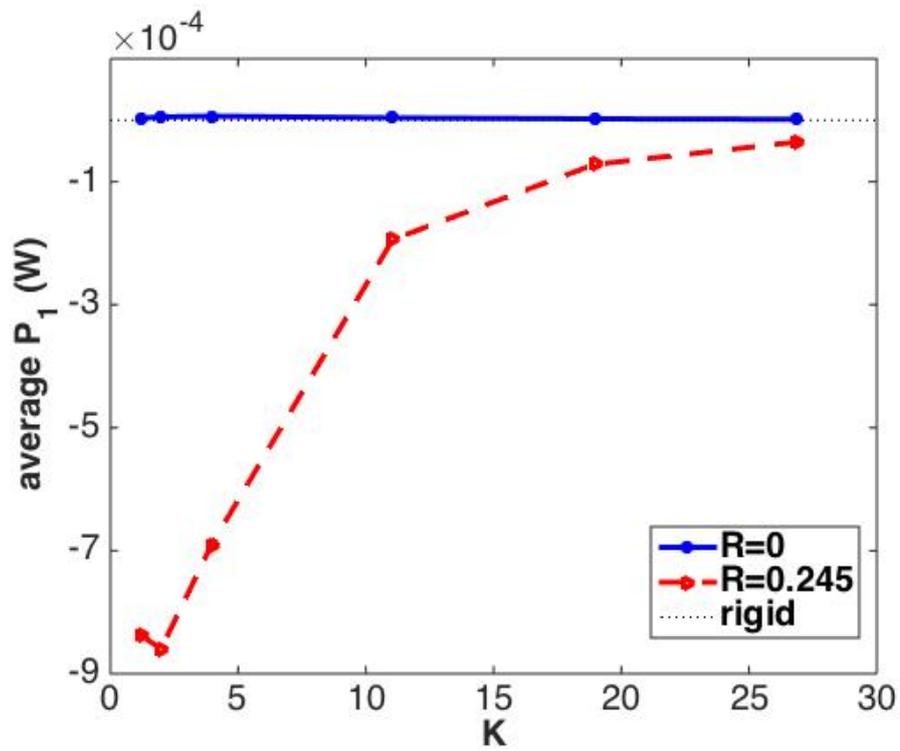
(a)
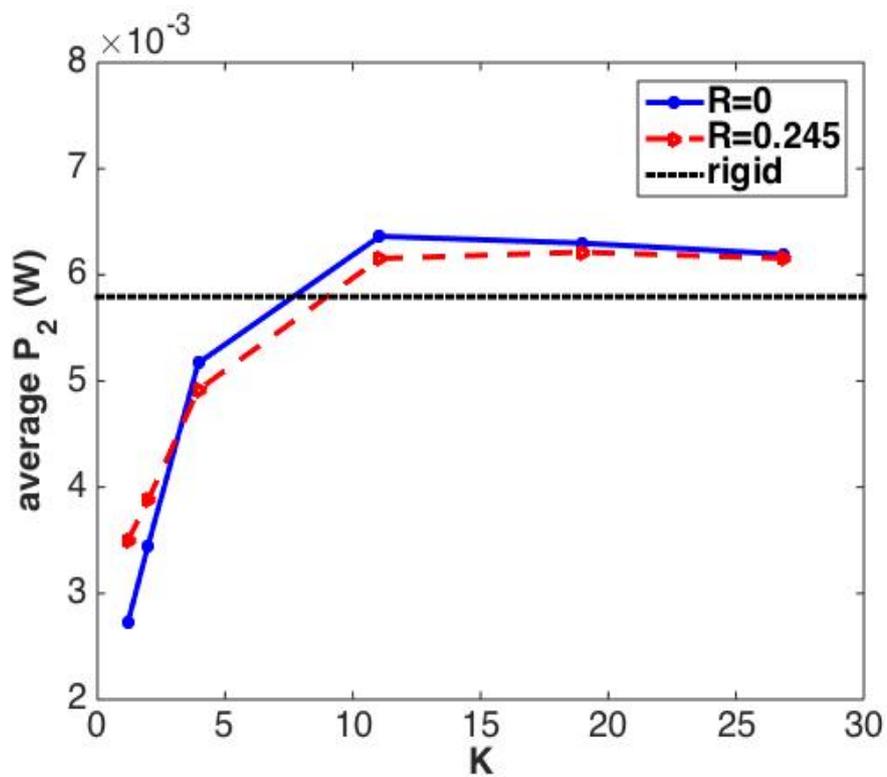
(b)

Figure 5.24 Average power at (a) passive joint and (b) active joint.

5.5.6 Vorticity Contour

From the vorticity contour shown in Figure 5.25, a typical reverse von Kármán vortex street is observed although the undesired vortex leak from the gap between adjacent elements. The strength of the vortex street can enhance the thrust force, and the wake structure is highly dependent on the undulatory profile, especially the flexibility of the tail. The cases with faster swimming speed show stronger vortex strength.
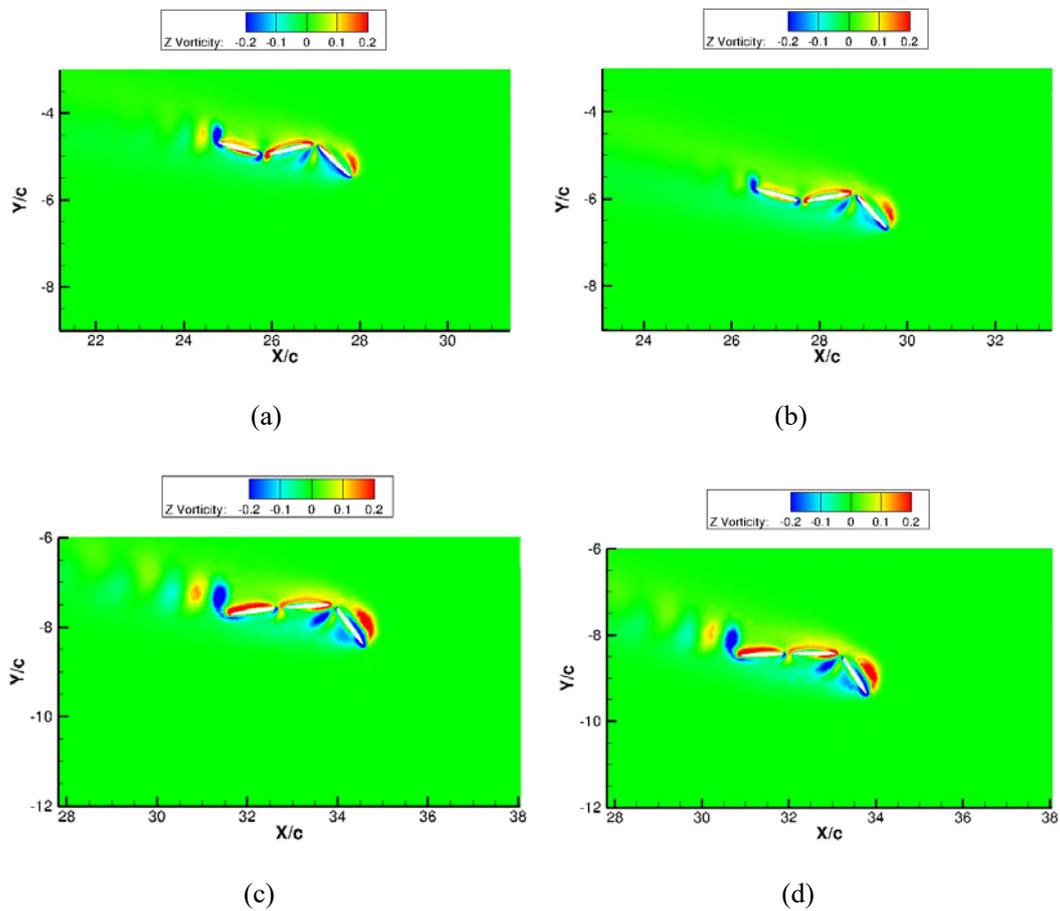
Figure 5.25 Vorticity contour of cases with (a) K=1.97, R=0, (b) K=1.97, R=0.245, (c) K=11.05, R=0, (d) K=11.05, R=0.245 at time instant t/T=19.

5.6 Discussion

In nature, fish species can achieve a wide range of body undulatory motion to adapt to the changes of hydrodynamic loads under the different environment (Blight, 1976, 1977). They have developed advanced swimming patterns, for example, the *carangiform* swimming mode is preferred by fast swimmers (e.g. mackerel), and the *anguilliform* swimming mode is beneficial to the swimmers (e.g. eel) requiring mobile manoeuvrability and high propulsion efficiency. There are complex interactions between muscle mechanical properties, fish body form, swimming mode, and swimming speed (Altringham and Ellerby, 1999). This can be seen as a problem coupling with two subjects, one is the internal dynamics indicating how fish activate body undulation, and the other is external dynamics illuminating how fish move in water under specific undulatory pattern.

The proposed method of MMS algorithm coupling with CFD solver is developed and proved competently to solve such problems. It is an essential achievement in this chapter by creating a general solution for investigating the biomimetic system through CFD simulations, especially the multi-body system. Though practically fish motion is propelled by muscle stimulation instead of eclectic motor, it is complicated to produce man-made muscle to fully mimic the real animal muscle. In this situation, the MMS model with participations by internal torque, body stiffness, and phase delay, etc., is of importance for providing a clue on advanced biomimetic investigation. The undulation motion can be mimicked accurately by adjusting the ways of control on linked hinges, and the more segments and hinges applied, the more precise undulation motion is achieved. Moreover, the coupling procedure with fluid solver is straightforward, and hydrodynamic performance can be obtained by the mature CFD techniques.

The test cases in Section 5.5 is very simplified with an articulated fish model, which is a three linked rigid segment system with an arbitrary sinusoidal pitch motion

applied at active joint between body and tail, and a linear spring model applied at passive joint to mimic flexible tail. The test case does not present any specific swimming mode in nature, but the flexibility mechanism can be examined from this schematic. In general, there is an optimal stiffness, under which the model swims with the fastest velocity. Effect of damper can be drawn only when stiffness is small. The damper can shift the phase of induced angle by delaying the response of spring, and hence change the propulsion posture, which causes different swimming speed. Comparing with the rigid tail, the flexible tail lead faster speed when the stiffness and damping coefficients are in a suitable range. The properties of spring stiffness and damper, the induced/prescribed pitch angle and torques are typical variables from the aspect of internal dynamics. The fast speed is a result of increase of lateral forces produced by bigger input torque, and also a consequence of less power loss due to a properly induced undulatory swimming pattern, which are all related to the subject of external dynamics. It is seen form the test case that the variables from both internal and external dynamics can be clearly illustrated.

The analysis of the internal variables effect on external behaviour should be more enhanced with more investigations. The future work would be to focus on activating advanced ways of control, and implement the method on more practical physical model for further exploration of undulatory mechanisms.

Chapter 6 Discussion

This chapter reviews models and methods to tackle the problems and reflects on the results and contributions. Potential further research work is also recommended.

6.1 Key Findings

All the key findings are arranged in this section, and listed in the individual sub-section of each case.

6.1.1   Flapping Wing with 1DoF in Lateral Direction (Chapter 3)

The locomotion of a prescribed plunging wing with one degree of freedom in lateral direction in stationary fluid has been studied systematically by a three-dimensional fluid-motion coupling method. The key findings are as below:

- The 2D symmetry breaking down process is reviewed, and the 3D wing phenomenon is illustrated of a transit period within which the vortex collides with others, resulting in vortex dipole to accelerate the velocity. Then a stable state is achieved when viscous force and propulsion force are balanced.

- There is a significant increase in the amplitude of thrust coefficient for wings with bigger aspect ratios, which lead faster lateral velocities.

- Wings with short aspect ratios (AR=1.0 and 2.0) produce circular vortex rings, as the TV is close to each other along a short aspect distance. For wing with AR=4.0, the tip-vortices are not well merged, resulting in the vortex shape being stretched thinner and forming elongated loops. Generally, the latter structure is beneficial to generating stronger jet flow, reducing energy dissipation, and thus facilitating a faster traveling speed.

- Re_u increases monotonically with Re_{fr}. Re_u turns into a linear function of Re_{fr} when Re_{fr} is over a critical value, ranging from 40-60 in the current study. Induced velocity becomes larger as the aspect ratio increases at fixed Re_{fr}.

- The present simulations indicate that low-aspect-ratio wings lead to the same St number as large-aspect-ratio ones under stronger flapping frequencies. Besides, the St number mostly appears within the interval of 0.2-0.5.

- Wings reach similar final average velocities after initial evolution cycles. The ones with larger mass ratio take more cycles to achieve the quasi-steady velocity, and have smaller fluctuations.

- The moving direction is sensitive to the initial mesh condition. It can be seen that the perturbation has no effect on final quasi-steady velocity amplitude, but clearly has some effect on travelling direction and evolution process.

6.1.2   Flapping Wing with 2DoF in Lateral and Rotational Directions (Chapter 4)

The numerical study also investigated the dynamics of a three-dimensional low aspect ratio wing that flaps up and down with the pitching and horizontal motions are passively induced. The wing system stiffness is introduced and modelled by a torsional spring at the pivot point. The key findings are as below:

- Symmetry breakdown phenomenon also exists, and the wing starts its lateral movement almost at the same time when its rotational motion starts. The wings with larger aspect ratios take more cycles to break the symmetry and generate stronger reverse von Kármán Vortex Street.

- The spectral analysis dictates that the induced pitch motion follow one dominant frequency, while the induced lateral motion vary from multiple frequencies to one dominant frequency with increase of wing's stiffness. According to the latter one, the flow status is classified into three different

modes.

- The less stiff wing has relatively wider vorticity shedding street and decreased lateral velocity.

- The wing with large aspect ratios shows large thrust force and thus faster induced lateral velocity than those of short spans.

- The impact of density ratio on the lateral velocity is smaller than its influence on induced pitch motion, and the density ratio impact is influenced by the wing aspect distance.

- Adjustment of the pivot point location away from chord-centre to the leading edge leads improvement of propulsion performance, and the stiffness influence on the wing propulsion is strongly linked to the pitching axis.

6.1.3   Multi-body System (Chapter 5)

A hybrid algorithm for the multi-body system was implemented into the CFD solver. It was evaluated by a self-propelled articulated system with three rigid components linked with active and passive joints. The main results shown from this part of work is as below.

- The MMS algorithm is successfully implemented in CFD solver, and the validation results match well with the previous published work.

- The verification and test cases indicate that the method is capable of dealing with various undulatory motions through different ways of hinge control.

- The joint flexibility effect is examined through the innovative test case, and it shows that the proper soft tail can enhance the propulsion performance.

6.2 Achievements against Objectives

The main aim of this PhD study was to investigate the fundamental fluid mechanisms involved in flapping and undulatory propulsive motion by means of numerical simulations of bio-inspired models.

The first minor objective is as follows:

- *Implementing computational techniques on simulations that require moving boundary condition, and developing coupled method between CFD solver and kinetic equations for solving self-propelled motion of fluid-structure interaction models.*

Two physical models are investigated with three-dimensional flapping wing with flexibilities in lateral and rotational directions, and another independent study is on the model of a multi-body system with rigid components connected by revolute joints. The numerical techniques are successfully implemented on Fluid-Structure Interaction problems with unsteady dynamic moving boundaries. The supplemental validity of the developed numerical methods using flow solver ANSYS FLUENT with developed User Defined Function code is demonstrated by comparing with previous work.

The second objective is achieved in Chapter 3 and Chapter 4 by flapping wing models:

- *Examining hydrodynamic performance of flapping motion with the simplified model of three-dimensional rigid wing, and clarifying the effects of different geometric and kinematic parameters on propulsion production, especially in the conditions of low aspect ratio with one or two degrees of freedom released.*

The problems with parameters that control the system kinematic and dynamic features are presented along with a systematic analysis on the simulating results. We start with

examination on how the lateral and pitching movement of wing is activated by its vertical flapping motion, followed by a discussion on the results in the fully developed quasi-steady state. Our particular interest is centred on the three-dimensional and pitch–pivot-point influence, which is done by comparison of two-dimensional and three-dimensional wing data and bias pitching axis.

The following objective is addressed in Chapter 5:

- *Developing a method to solve the coupling problems with multi-body dynamics and fluid dynamics through implementing Mobile Multi-body System (MMS) algorithm with CFD solver, which should be capable of simplifying the numerical simulations on the models with undulatory motion.*

A Newton-Euler based algorithm with manipulator dynamics to resolve the problems with both forward and inverse dynamics is successfully implemented with CFD solver. The numerical method is tested with verification cases, and innovative cases are made on a prototype with both active joints and passive joints. The effect of joint flexibility on the propulsion is illustrated with a parametric study.

6.3 Novelties and Contributions to the Field

6.3.1 Novelties

To the best of author's knowledge, this thesis introduces novel research in the following aspects:

- The simplified bio-inspired locomotion system is classified into two categories, undulatory motion and flapping motion, and the classic studies on hydrodynamic performance of such models are thoroughly reviewed from the

application on propulsion based system and energy harvesting based system.

- The simulations are produced along with the proper treatments on both pre-processing and post-processing for the self-propelled three-dimensional wing model, and the way of generating cases and analysing results can be used on the other related models.

- Physical phenomenon of symmetry breakdown of the three-dimensional flapping wing model under various kinetic and geometric parameters is recorded systematically in both Chapter 3 and 4.

- Numerical initial perturbation effect on the self-induced lateral motion is documented in Chapter 3.

- Aspect ratio effect is systematically illustrated from hydrodynamic point of view on the three-dimensional flapping wing model with the released freedom in either lateral direction or combination of lateral and pitching direction in both Chapter 3 and 4.

- The hybrid algorithm based on Newton-Euler Framework for solving Mobile Multi-body System model is successfully implemented into full resolved CFD simulations. The coupling method is capable of mimicking the undulatory motion and predicting the self-induced motion.

- Innovative test case is made on a simplified articulated fish model, and the hinge type is developed with both passive and active joints. The simulation results are illustrated with both internal and external variables, and confirm that the flexibility of fish tail can enhance the propulsive performance.

6.3.2 Contributions to Existing Literature

The following publications were generated throughout the timespan of the PhD studies related to this thesis.

<u>Journal papers:</u>

- **J. Hu**, Q. Xiao*, M. Porez, F. Boyer, A coupling method between multi-body dynamics and hydrodynamics for fully resolved simulation of bio-inspired robots, *under review*.

- **J. Hu**, Q. Xiao*, Three dimensional effects on the translational locomotion of a passive heaving wing, *Journal of Fluids and Structures*, 2014, Vol. 4, pp. 77-88.

- Q. Xiao*, **J. Hu**, H. Liu, Role of flexibility and inertia on the dynamics of low-aspect-ratio flapping wings, *Bioinspiration & Biomimetics*, 2014, Vol. 9, pp. 016008.

<u>Conference papers:</u>

- **J. Hu**, Q. Xiao and A. Incecik, Dynamic Response of a Flapping Foil with a Non-sinusoidal Kinematic Motion, *the 21st International Offshore and Polar Engineering Conference, (ISOPE)*, 2011-NK-02, 2011, Maui, Hawaii, USA, Vol.2, pp. 239-245.

- **J. Hu**, Q. Xiao, Numerical Simulation for Self-propelled 3D Flapping Wing -- Comparison with Two-dimensional Case. *6th International Conference on Model Transformation (ICMT)*, 2012, Harbin, China.

- **J. Hu**, Q. Xiao, An Exploration of A Passive Articulated Fish-like System, ASME 2013, *32nd International Conference on Ocean, Offshore and Arctic Engineering, (OMAE)*, 10808, 2013, Nantes, France

6.4 General Discussion

In the present study, the bio-inspired locomotion is simplified as the flapping motion of a three-dimensional wing model and the undulatory motion of an articulated

multi-body system model. CFD simulations are carried out for investigation. The particular focus is on the hydrodynamic performance of the self-induced locomotion.

The flapping wing model is designed with left-right symmetric geometry, and proposed with induced motion in lateral direction and combination of both lateral and pitching directions under prescribed plunging motion in Chapter 3 and 4. The drawbacks are that symmetric geometry of the wing is not ideal for propulsion, and the prescribed motion profile is also very simplified. The robotic fish caudal fins are usually designed with better geometry and use smarter propulsive profiles. However it is believed that the results obtained are vital to elucidate the flapping wing propulsion mechanism.

Firstly, the phenomenon of symmetry breakdown itself is of interest to locomotion start-up and stability issues. The moving direction is selected by the initial environment perturbations that play an important role only at the beginning stage. The vortex dipoles grow and develop quickly with the symmetry breakdown, and the wing finally reaches a quasi-steady status after transit period. The fundamental mechanism indicates that it could be effective to improve the design of devices aiming for propulsion or balance through adjusting the initial perturbation and controlling the generation and development procedure of vortex dipoles.

Secondly, the induced locomotion is highly dependent on geometric and kinematic parameters. The wing with longer span-wise length takes fewer cycles to break the symmetry, and moves with faster induced lateral velocity in quasi-steady status under the same prescribed motion profile. The long span-wise length is responsible for enhancing force generation, and the short span-wise length is corresponding to stabilizing the motion. This can also be observed in flying insects and manoeuvring fish that fly or swim at low Reynolds numbers by flapping their wings or pectoral fins with low span-wise length as compared to those of bat and birds.

Thirdly, the freedom in pitching can accelerate the symmetry breakdown. Analysis of the data within the fully developed flow regimes shows that the wing always pitches at the same frequency as forced plunging frequency. Interestingly, the frequency of induced lateral velocity is profoundly dependent on the wing torsional stiffness and density, varying from multiple frequencies to one dominant frequency with the increase in the wing's stiffness and density. It is noticed that the induced lateral velocity can be enhanced when the pitching axis is far from the middle of chord centre line. The stiffness influences on the wing propulsion is strongly linked to the pitching axis. These findings highly resemble the observations from biological fliers/swimmers, even though some parameters in the present studied is beyond the range of that of real animal.

Besides the flapping motion, the undulatory motion is achieved by adapting the multi-body system model in Chapter 5. The coupling method between MMS algorithm and fluid solver holds the potential for mimicking the undulation profile of the real fish species. The advantage is that both internal and external variables can be clearly captured, and there are multiple ways to control the undulatory profile through setting joint types and number of body elements. The verifications and validations are carried out for confirming the accuracy of the coupling method. The innovative test case indicates the joint flexibility effect on propulsion performance, that the induced locomotion is a result of the body posture which is controlled by proper spring stiffness and damper applied at the passive joint. It is of importance for the exploration of smart bio-inspired control mechanisms.

Regarding the numerical simulation, both structured and unstructured mesh are appropriately conducted on different cases. Flow fields of all the cases in this thesis are simulated by laminar flow as the problems lie in the acceptable range of low Reynolds number with no flow separation. The dynamic mesh plays a significant role in the self-included locomotion simulations. It should mention that the comparisons of CFD results with experiments are limited in this thesis, whereas the validations are

carefully examined by repeating the classic published cases numerically. CFD simulations may consume longer time than the fast method based on empirical equations, but it could provide enormous information and draw clear picture of the physical fluid status.

6.5 Recommended Future Work

In the present study, propulsive performance of individual flapping wing has been investigated, and a method using MMS algorithm coupled with CFD solver has been successfully established. The major effort has been to mimic bio-inspired swimming by the flapping wing model and rigid multi-body system model. However due to the limited research period and limited computing resources, the present studies cannot cover every relevant topic. In the field of bio-inspired study and biomimetic modelling, there are still many interesting phenomenon to be explored. Based on the available work, a few points are recommended here for the future work.

- *Investigation of the function of different fins and their elasticity effect*
  It is widely accepted that fish fins play different roles in fish swimming. The future studies should straightforwardly mimic the fish fins with proper geometries and advance prescribed propulsive locomotion. The different types of fish fins are worthwhile to be investigated.

- *Studies on fish starting, manoeuvrability and stability*
  Coupling with the recommended study on functions of different kinds of fish fins, the hydrodynamic mechanisms of released swimming fish can be further explored in the aspects of starting (e.g. C-start), turning, acceleration and stability. The structure of entire fish body with fins can be generated with multi-body system with tree-type structure.

- ***General applications in modelling and designing biomimetic robot including soft robot***

  The method of MMS algorithm coupled with CFD solver can be implemented on the models with more complicated geometries and more advanced hinges, for better imitating the locomotion. It has wide applications in modelling biomimetic robot. Recently, studies on soft robot have attracted a lot of attentions. The coupled method might be capable of modelling soft robot, such as jellyfish, octopus, etc, through smart ways of control.

- ***Applications based on both active and passive control***

  Bio-mimetic studies aim to explore its mechanism and apply them to optimize the design of man-made devices. Apart from imitating shape geometry and locomotion of animals, the approach based on passive control is also very popular. For example, the energy harvesting devices are designed with both active and passive control (Xiao and Zhu, 2014). The applications in drag reduction and energy harvesting can be further explored.

Chapter 7 Conclusions

- The current study has led to greater insight into the hydrodynamics of low-aspect-ratio wings, which is common among many species of fish that employ flapping-like mode for propulsion. Based on the model of an undulatory fish body using rigid articulated component elements, the current study has proposed a new method for understanding the fundamental hydrodynamics and internal dynamics. Numerical simulations are conducted for the cases with a coupling method between CFD solver and in-house codes for dealing with self-propelled locomotion. The bio-mimetic locomotion including flapping motion and undulatory motion is systematically investigated, and also well documented in this thesis.

- The investigation of the flapping wing model shows that the induced wing motion is a result of system stability breakdown. Initial perturbation plays a role in the evolution development, and the passively rotational pitching help with the symmetry breakdown. The wings with larger aspect ratios take more cycles to break the symmetry and generate stronger reverse von Kármán Vortex Street. When the kinematic motion is fully developed, the wing reaches a periodic stage with induced pitching frequency identical to its forced flapping frequency and multi-spike frequencies of lateral velocity. There is a significant increase in the amplitude of thrust coefficient for wings with bigger aspect ratios, which lead faster lateral velocities. Induced velocity turns into a linear function of flapping frequency over a critical range. Low-aspect-ratio wings lead to the same *St* number as large-aspect-ratio ones under stronger flapping frequencies. The less stiff wing has relatively wider vorticity shedding street and decreased lateral velocity. The impact of density ratio on the lateral velocity amplitude is smaller than its influence on induced pitch motion, and the density ratio effect is

influenced by the wing aspect distance. Adjustment of the pivot point location away from chord-centre to the leading edge leads improvement of propulsion performance, and the stiffness influence on the wing propulsion is strongly linked to the pitching axis. All the findings address the effects of wing aspect ratio, inertia, torsional stiffness and pivot point on the dynamics response of a low aspect ratio rectangular wing under an initial zero speed flow field condition. The results provide fundamental understanding of flapping wing's kinematic performance, and it can definitely provide technical support for the design of conceptual underwater devices with flapping wings for propulsion and manoeuvrability control, as shown in Figure 7.1.
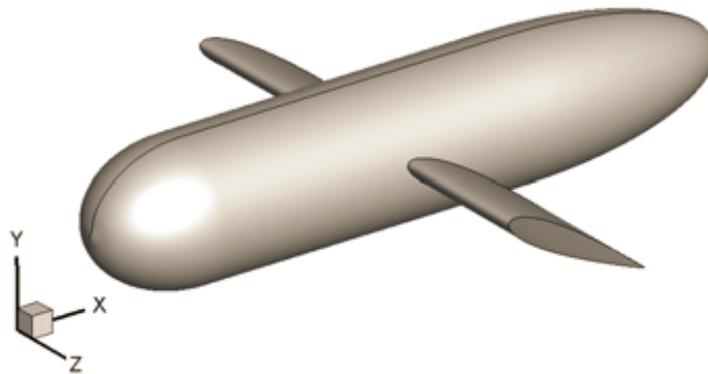
Figure 7.1 A conceptual underwater device with flapping wings for propulsion and manoeuvrability control.

- The other main contribution in this thesis is about mimicking undulatory motion with a series of linked rigid bodies, i.e. a multi-body system. A hybrid algorithm for the multi-body system is successfully implemented into the CFD solver. The connection between two adjacent rigid elements can be modelled as the revolute hinge joint, with either a passively induced pitch motion or actively prescribed pitch motion. The innovative results are obtained by simulating a simplified articulated system and parametric study indicates the tail flexibility plays an important role on the propulsion performance. The method leads a way to model various machinery controlled undulatory motions.

Bibliography

Akhtar, I., Mittal, R., 2005. A Biologically Inspired Computational Study of Flow Past Tandem Flapping Foils, 35th AIAA Fluid Dynamics Conference and Exhibit, Toronto, Ontario Canada.

Alben, S., Shelley, M., 2005. Coherent locomotion as an attracting state for a free flapping body. P Natl Acad Sci USA 102, 11163-11166.

Alben, S., Shelley, M.J., 2008. Flapping states of a flag in an inviscid fluid: Bistability and the transition to chaos. Phys Rev Lett 100.

Altringham, J.D., Ellerby, D.J., 1999. Fish swimming: Patterns in muscle function. J Exp Biol 202, 3397-3403.

Anderson, J.M., Streitlien, K., Barrett, D.S., Triantafyllou, M.S., 1998. Oscillating foils of high propulsive efficiency. J Fluid Mech 360, 41-72.

Argentina, M., Mahadevan, L., 2005. Fluid-flow-induced flutter of a flag. P Natl Acad Sci USA 102, 1829-1834.

Barrett, D.S., Triantafyllou, M.S., Yue, D.K.P., Grosenbaugh, M.A., Wolfgang, M.J., 1999. Drag reduction in fish-like locomotion. J Fluid Mech 392, 183-212.

Beal, D.N., Hover, F.S., Triantafyllou, M.S., Liao, J.C., Lauder, G.V., 2006. Passive propulsion in vortex wakes. J Fluid Mech 549, 385-402.

Benkherouf, T., Mekadem, M., Oualli, H., Hanchi, S., Keirsbulck, L., Labraga, L., 2011. Efficiency of an auto-propelled flapping airfoil. J Fluid Struct 27, 552-566.

Bergmann, M., Iollo, A., Mittal, R., 2013. Influence of caudal fin elasticity on swimmer propulsion, 2nd Symposium on Fluid-Structure-Sound Interactions and Control, Hong-Kong / Macau, pp. hal-00906927.

Blight, A.R., 1976. Undulatory swimming with and without waves of contraction.

Nature 264, 352-354.

Blight, A.R., 1977. The muscular control of vertebrate swimming movements. Biological Reviews 52, 181-218.

Blondeaux, P., Fornarelli, F., Guglielmini, L., Triantafyllou, M.S., Verzicco, R., 2005. Numerical experiments on flapping foils mimicking fish-like locomotion. Phys Fluids 17.

Buchwald, R., Dudley, R., 2010. Limits to vertical force and power production in bumblebees (Hymenoptera: Bombus impatiens). J Exp Biol 213, 426-432.

Carling, J., Williams, T.L., Bowtell, G., 1998. Self-propelled anguilliform swimming: Simultaneous solution of the two-dimensional Navier-Stokes equations and Newton's laws of motion. J Exp Biol 201, 3143-3166.

Cheng, B., Fry, S.N., Huang, Q., Deng, X., 2010. Aerodynamic damping during rapid flight maneuvers in the fruit fly Drosophila. J Exp Biol 213, 602-612.

Cho, H., Zhu, Q., 2014. Performance of a flapping foil flow energy harvester in shear flows. J Fluid Struct 51, 199-210.

Combes, S.A., Daniel, T.L., 2001. Shape, flapping and flexion: Wing and fin design for forward flight. J Exp Biol 204, 2073-2085.

Combes, S.A., Daniel, T.L., 2003a. Flexural stiffness in insect wings I. Scaling and the influence of wing venation. J Exp Biol 206, 2979-2987.

Combes, S.A., Daniel, T.L., 2003b. Flexural stiffness in insect wings II. Spatial distribution and dynamic wing bending. J Exp Biol 206, 2989-2997.

Connell, B.S.H., Yue, D.K.P., 2007. Flapping dynamics of a flag in a uniform stream. J Fluid Mech 581, 33-68.

Deng, J., Caulfield, C.P., Shao, X.M., 2014. Effect of aspect ratio on the energy extraction efficiency of three-dimensional flapping foils. Phys Fluids 26.

Deng, J., Shao, X.M., Ren, A.L., 2006. Numerical Study on Propulsive Performance

of Fish-Like Swimming Foils. J Hydrodyn 18, 681-687.

Deng, J., Teng, L.B., Pan, D.Y., Shao, X.M., 2015. Inertial effects of the semi-passive flapping foil on its energy extraction efficiency. Phys Fluids 27, 053103.

Dong, G.J., Lu, X.Y., 2005. Numerical analysis on the propulsive performance and vortex shedding of fish-like travelling wavy plate. Int J Numer Meth Fl 48, 1351-1373.

Dong, H., Mittal, R., Najjar, F.M., 2006. Wake topology and hydrodynamic performance of low-aspect-ratio flapping foils. J Fluid Mech 566, 309-343.

Drucker, E.G., Lauder, G.V., 1999. Locomotor forces on a swimming fish: Three-dimensional vortex wake dynamics quantified using digital particle image velocimetry. J Exp Biol 202, 2393-2412.

Eldredge, J.D., 2008. Dynamically coupled fluid-body interactions in vorticity-based numerical simulations. J Comput Phys 227, 9170-9194.

Eldredge, J.D., Toomey, J., Medina, A., 2010. On the roles of chord-wise flexibility in a flapping wing with hovering kinematics. J Fluid Mech 659, 94-115.

Farnell, D.J.J., David, T., Barton, D.C., 2004a. Coupled states of flapping flags. J Fluid Struct 19, 29-36.

Farnell, D.J.J., David, T., Barton, D.C., 2004b. Numerical simulations of a filament in a flowing soap film. Int J Numer Meth Fl 44, 313-330.

Faruque, I., Humbert, J.S., 2010a. Dipteran insect flight dynamics. Part 1 Longitudinal motion about hover. J Theor Biol 264, 538-552.

Faruque, I., Humbert, J.S., 2010b. Dipteran insect flight dynamics. Part 2: Lateral-directional motion about hover. J Theor Biol 265, 306-313.

Featherstone, R., 1983. The calculation of robot dynamics using articulated-body inertias. The International Journal of Robotics Research 2, 13-30.

Ferziger, J.H., Peric, M., 1996. Computational methods for fluid dynamics. Springer,

Berlin ; London.

Freymuth, P., 1988. Propulsive Vortical Signature of Plunging and Pitching Airfoils. Aiaa J 26, 881-883.

Gao, N., Aono, H., Liu, H., 2011. Perturbation analysis of 6DoF flight dynamics and passive dynamic stability of hovering fruit fly Drosophila melanogaster. J Theor Biol 270, 98-111.

Garrick, I.E., 1937. Propulsion of a flapping and oscillating airfoil.

Glowinski, R., Pan, T.W., Hesla, T.I., Joseph, D.D., 1999. A distributed Lagrange multiplier fictitious domain method for particulate flows. Int J Multiphas Flow 25, 755-794.

Guerrero, J., 2009. Numerical Simulation of the Unsteady Aerodynamics of Flapping Flight, Department of Civil, Environmental and Architectural Engineering. University of Genoa.

Guglielmini, L., Blondeaux, P., 2004. Propulsive efficiency of oscillating foils. Eur J Mech B-Fluid 23, 255-278.

Heathcote, S., Gursul, I., 2007. Flexible flapping airfoil propulsion at low Reynolds numbers. Aiaa J 45, 1066-1079.

Heathcote, S., Wang, Z., Gursul, I., 2008. Effect of spanwise flexibility on flapping wing propulsion. J Fluid Struct 24, 183-199.

Hedrick, T.L., Cheng, B., Deng, X.Y., 2009. Wingbeat Time and the Scaling of Passive Rotational Damping in Flapping Flight. Science 324, 252-255.

Hover, F.S., Haugsdal, O., Triantafyllou, M.S., 2004. Effect of angle of attack profiles in flapping foil propulsion. J Fluid Struct 19, 37-47.

Hu, J.X., Xiao, Q., 2014. Three-dimensional effects on the translational locomotion of a passive heaving wing. J Fluid Struct 46, 77-88.

Hu, J.X., Xiao, Q., Incecik, A., 2011. Dynamic response of a flapping foil with a

non-sinusoidal kinematic motion, 21st International Offshore and Polar Engineering Conference (ISOPE), Hawaii, USA, p. 239.

Ishihara, D., Horie, T., Denda, M., 2009. A two-dimensional computational study on the fluid-structure interaction cause of wing pitch changes in dipteran flapping flight. J Exp Biol 212, 1-10.

Kajtar, J.B., Monaghan, J.J., 2010. On the dynamics of swimming linked bodies. Eur J Mech B-Fluid 29, 377-386.

Kang, C.K., Aono, H., Cesnik, C.E.S., Shyy, W., 2011. Effects of flexibility on the aerodynamic performance of flapping wings. J Fluid Mech 689, 32-74.

Kang, C.K., Shyy, W., 2013. Scaling law and enhancement of lift generation of an insect-size hovering flexible wing. J R Soc Interface 10.

Khalil, W., Gallot, G., Boyer, F., 2007. Dynamic modeling and simulation of a 3-D serial eel-like robot. Ieee T Syst Man Cy C 37, 1259-1268.

Kim, S., Karrila, S.J., 1991. Microhydrodynamics : principles and selected applications. Butterworth-Heinemann, Boston ; London.

Kinsey, T., Dumas, G., 2008. Parametric study of an oscillating airfoil in a power-extraction regime. Aiaa J 46, 1318-1330.

Kinsey, T., Dumas, G., Lalande, G., Ruel, J., Mehut, A., Viarouge, P., Lemay, J., Jean, Y., 2011. Prototype testing of a hydrokinetic turbine based on oscillating hydrofoils. Renew Energ 36, 1710-1718.

Lamb, H., 1930. Hydrodynamics, 5th ed. Cambridge University Press, Cambridge.

Leroyer, A., Visonneau, M., 2005. Numerical methods for RANSE simulations of a self-propelled fish-like body. J Fluid Struct 20, 975-991.

Lewin, G.C., Haj-Hariri, H., 2003. Modelling thrust generation of a two-dimensional heaving airfoil in a viscous flow. J Fluid Mech 492, 339-362.

Licht, S., Polidoro, V., Flores, M., Hover, F.S., Triantafyllou, M.S., 2004. Design and

projected performance of a flapping foil AUV. Ieee J Oceanic Eng 29, 786-794.

Lighthill, M.J., 1960. Note on the Swimming of Slender Fish. J Fluid Mech 9, 305-317.

Lighthill, M.J., 1971. Large-Amplitude Elongated-Body Theory of Fish Locomotion. Proc R Soc Ser B-Bio 179, 125-132.

Long, J.H., 1998. Muscles, elastic energy, and the dynamics of body stiffness in swimming eels. Am Zool 38, 771-792.

Lu, X.Y., Liao, Q., 2006. Dynamic responses of a two-dimensional flapping foil motion. Phys Fluids 18.

McKinney, W., DeLaurier, J., 1981. Wingmill: an oscillating-wing windmill. Journal of energy 5, 109--115.

Michelin, S., Smith, S.G.L., 2009. Resonance and propulsion performance of a heaving flexible wing. Phys Fluids 21.

Miller, L.A., Peskin, C.S., 2004. When vortices stick: an aerodynamic transition in tiny insect flight. J Exp Biol 207, 3073-3088.

Mittal, R., Iaccarino, G., 2005. Immersed boundary methods. Annu Rev Fluid Mech 37, 239-261.

Mountcastle, A.M., Combes, S.A., 2013. Wing flexibility enhances load-lifting capacity in bumblebees. P Roy Soc B-Biol Sci 280.

Nakata, T., Liu, H., 2012. Aerodynamic performance of a hovering hawkmoth with flexible wings: a computational approach. P Roy Soc B-Biol Sci 279, 722-731.

Ostrowski, J., Burdick, J., 1998. The geometric mechanics of undulatory robotic locomotion. Int J Robot Res 17, 683-701.

Otten, E., 2003. Inverse and forward dynamics: models of multi-body systems. Philos T Roy Soc B 358, 1493-1500.

Patankar, S.V., Spalding, D.B., 1972. Calculation Procedure for Heat, Mass and Momentum-Transfer in 3-Dimensional Parabolic Flows. Int J Heat Mass Tran 15, 1787-&.

Pedro, G., Suleman, A., Djilali, N., 2003. A numerical study of the propulsive efficiency of a flapping hydrofoil. Int J Numer Meth Fl 42, 493-526.

Peng, Z.L., Zhu, Q., 2009. Energy harvesting through flow-induced oscillations of a foil. Phys Fluids 21.

Porez, M., Boyer, F., Belkhiri, A., 2014a. A hybrid dynamic model for bio-inspired robots with soft appendages-application to a bio-inspired flexible flapping-wing micro air vehicle, International Conference on Robotics and Automation. Citeseer.

Porez, M., Boyer, F., Belkhiri, A., 2014b. A hybrid dynamic model for bio-inspired robots with soft appendages - Application to a bio-inspired flexible flapping-wing micro air vehicle. Submitted to IEEE ICRA.

Porez, M., Boyer, F., Ijspeert, A.J., 2014c. Improved Lighthill fish swimming model for bio-inspired robots: Modeling, computational aspects and experimental comparisons. Int J Robot Res 33, 1322-1341.

Ramananarivo, S., Godoy-Diana, R., Thiria, B., 2011. Rather than resonance, flapping wing flyers may play on aerodynamics to improve performance. P Natl Acad Sci USA 108, 5964-5969.

Read, D.A., Hover, F.S., Triantafyllou, M.S., 2003. Forces on oscillating foils for propulsion and maneuvering. J Fluid Struct 17, 163-183.

Sane, S.P., Dickinson, M.H., 2002. The aerodynamic effects of wing rotation and a revised quasi-steady model of flapping flight. J Exp Biol 205, 1087-1096.

Schouveiler, L., Hover, F.S., Triantafyllou, M.S., 2005. Performance of flapping foil propulsion. J Fluid Struct 20, 949-959.

Sfakiotakis, M., Lane, D.M., Davies, J.B.C., 1999. Review of fish swimming modes

for aquatic locomotion. Ieee J Oceanic Eng 24, 237-252.

Shao, X.M., Pan, D.Y., Deng, J., Yu, Z.S., 2010. Numerical Studies on the Propulsion and Wake Structures of Finite-Span Flapping Wings with Different Aspect Ratios. J Hydrodyn 22, 147-154.

Shen, L., Zhang, X., Yue, D.K.P., Triantafyllou, M.S., 2003. Turbulent flow over a flexible wall undergoing a streamwise travelling wave motion. J Fluid Mech 484, 197-221.

Shiels, D., Leonard, A., Roshko, A., 2001. Flow-induced vibration of a circular cylinder at limiting structural parameters. J Fluid Struct 15, 3-21.

Shyy, W., Lian, Y., Tang, J., Viieru, D., Liu, H., 2007. Aerodynamics of low Reynolds number flyers.

Spagnolie, S.E., Moret, L., Shelley, M.J., Zhang, J., 2010. Surprising behaviors in flapping locomotion with passive pitching. Phys Fluids 22.

Taneda, S., Tomonari, Y., 1974. An experiment on the flow around a waving plate. Journal of the Physical Society of Japan 36, 1683-1689.

Tang, S.J., Aubry, N., 1997. On the symmetry breaking instability leading to vortex shedding. Phys Fluids 9, 2550-2561.

Toomey, J., Eldredge, J.D., 2008. Numerical and experimental study of the fluid dynamics of a flapping wing with low order flexibility. Phys Fluids 20.

Triantafyllou, G.S., Triantafyllou, M.S., Grosenbaugh, M.A., 1993. Optimal Thrust Development in Oscillating Foils with Application to Fish Propulsion. J Fluid Struct 7, 205-224.

Triantafyllou, M.S., Triantafyllou, G.S., Gopalkrishnan, R., 1991. Wake Mechanics for Thrust Generation in Oscillating Foils. Phys Fluids a-Fluid 3, 2835-2837.

Tytell, E.D., Hsu, C.Y., Williams, T.L., Cohen, A.H., Fauci, L.J., 2010. Interactions between internal forces, body stiffness, and fluid environment in a neuromechanical

model of lamprey swimming. P Natl Acad Sci USA 107, 19832-19837.

van Loon, R., Anderson, P.D., van de Vosse, F.N., 2006. A fluid-structure interaction method with solid-rigid contact for heart valve dynamics. J Comput Phys 217, 806-823.

Vandenberghe, N., Childress, S., Zhang, J., 2006. On unidirectional flight of a free flapping wing. Phys Fluids 18.

Vandenberghe, N., Zhang, J., Childress, S., 2004. Symmetry breaking leads to forward flapping flight. J Fluid Mech 506, 147-155.

Vanella, M., Fitzgerald, T., Preidikman, S., Balaras, E., Balachandran, B., 2009. Influence of flexibility on the aerodynamic performance of a hovering wing. J Exp Biol 212, 95-105.

Visbal, M., Yilmaz, T.O., Rockwell, D., 2013. Three-dimensional vortex formation on a heaving low-aspect-ratio wing: Computations and experiments. J Fluid Struct 38, 58-76.

Walker, J.A., Westneat, M.W., 2002. Performance limits of labriform propulsion and correlates with fin shape and motion. J Exp Biol 205, 177-187.

Wang, C.J., Eldredge, J.D., 2015. Strongly coupled dynamics of fluids and rigid-body systems with the immersed boundary projection method. J Comput Phys 295, 87-113.

Wang, Z.J., 2000. Vortex shedding and frequency selection in flapping flight. J Fluid Mech 410, 323-341.

Wang, Z.J., 2005. Dissecting insect flight. Annu Rev Fluid Mech 37, 183-210.

Wehner, M., Truby, R.L., Fitzgerald, D.J., Mosadegh, B., Whitesides, G.M., Lewis, J.A., Wood, R.J., 2016. An integrated design and fabrication strategy for entirely soft, autonomous robots. Nature 536, 451-455.

Weihs, D., 1973. Hydromechanics of Fish Schooling. Nature 241, 290-291.

Willmott, A.P., Ellington, C.P., 1997a. The mechanics of flight in the hawkmoth

Manduca sexta .1. Kinematics of hovering and forward flight. J Exp Biol 200, 2705-2722.

Willmott, A.P., Ellington, C.P., 1997b. The mechanics of flight in the hawkmoth Manduca sexta .2. Aerodynamic consequences of kinematic and morphological variation. J Exp Biol 200, 2723-2745.

Wu, T.Y.T., 1961. Swimming of a Waving Plate. J Fluid Mech 10, 321-344.

Wu, T.Y.T., 1971a. Hydromechanics of Swimming Propulsion .1. Swimming of 2-Dimensional Flexible Plate at Variable Forward Speeds in an Inviscid Fluid. J Fluid Mech 46, 337-355.

Wu, T.Y.T., 1971b. Hydromechanics of Swimming Propulsion .2. Some Optimum Shape Problems. J Fluid Mech 46, 521-544.

Wu, T.Y.T., 1971c. Hydromechanics of Swimming Propulsion .3. Swimming and Optimum Movements of Slender Fish with Side Fins. J Fluid Mech 46, 545-568.

Xiao, Q., Liao, W., Yang, S., 2010. How Motion Trajectory Affects the Energy Extraction Performance of an Oscillating Foil, 48th AIAA Aerospace Sciences Meeting Including the New Horizons Forum and Aerospace Exposition, p. 65.

Xiao, Q., Liao, W., Yang, S.C., Peng, Y., 2012a. How motion trajectory affects energy extraction performance of a biomimic energy generator with an oscillating foil? Renew Energ 37, 61-75.

Xiao, Q., Liu, W.D., Hu, J.X., 2012b. Parametric study on a cylinder drag reduction using downstream undulating foil. Eur J Mech B-Fluid 36, 48-62.

Xiao, Q., Sun, K., Liu, H., Hu, J.X., 2011. Computational study on near wake interaction between undulation body and a D-section cylinder. Ocean Eng 38, 673-683.

Xiao, Q., Zhu, Q., 2014. A review on flow energy harvesters based on flapping foils. J Fluid Struct 46, 174-191.

Young, J., S. Lai, J.C., 2004. Oscillation frequency and amplitude effects on the wake of a plunging airfoil. Aiaa J 42, 2042-2052.

Young, J., S. Lai, J.C., 2007. Mechanisms influencing the efficiency of oscillating airfoil propulsion. Aiaa J 45, 1695-1702.

Yu, Z.S., 2005. A DLM/FD method for fluid/flexible-body interactions. J Comput Phys 207, 1-27.

Zhang, J., Liu, N.S., Lu, X.Y., 2010. Locomotion of a passively flapping flat plate. J Fluid Mech 659, 43-68.

Zhang, X., Ni, S.Z., Wang, S.Z., He, G.W., 2009. Effects of geometric shape on the hydrodynamics of a self-propelled flapping foil. Phys Fluids 21.

Zhu, Q., 2012. Energy harvesting by a purely passive flapping foil from shear flows. J Fluid Struct 34, 157-169.

Zhu, Q.A., Peng, Z.L., 2009. Mode coupling and flow energy harvesting by a flapping foil. Phys Fluids 21.

Curriculum Vitae

Jianxin Hu

Email: j.hu@strath.ac.uk / hujianxin123@hotmail.com

EDUCATION BACKGROUND:

Oct 2014 –
Mar 2016:
Postdoc research assistant in Engineering Science Department in University of Oxford, UK (supervisors: Prof. Richard Willden, Prof. Paul Taylor)

Oct 2010 –
Oct 2014:
PhD candidate in Naval Architecture, Ocean and Marine Engineering Department, *University of Strathclyde*, UK (supervisors: Dr. Qing Xiao & Prof. Atilla Incecik,)

Sep 2009 –
Sep 2010:
MSc. in Offshore Floating Systems, Naval Architecture, Ocean and Marine Engineering Department, *University of Strathclyde and Glasgow*. UK

Sep 2005 –
Jun 2009:
BEng. in Naval Architecture and Marine Engineering Department *Harbin Engineering University*. China

RESEARCH BACKGROUND:

Involved Projects:

- SuperGEN project funded by EPSRC, UK, in University of Oxford. (Oct 2014-Mar 2016)
- Research attachment with *Institut de Recherche en Communications et Cybernétique de Nantes*, France (Oct-Dec, 2013)
- Research attachment with *Institute of High Performance Computer*, Singapore (Apr-Oct, 2012)

Publications:

Journals:

- Q. Xiao, K. Sun, H. Liu and J. Hu, Computational study on near wake interaction between undulation body and a d-section cylinder, *Ocean Engineering, 2011, Vol.38, pp. 673-683.*

- Q. Xiao, W. Liu, J. Hu, Parametric study on a cylinder drag reduction using downstream undulating foil, *European Journal of Mechanics B-Fluids, 2012, Vol.36, pp. 48-62.*

- Q. Xiao, J. Hu, H. Liu, Effect of torsional stiffness and inertia on the dynamics of low aspect ratio flapping wings, *Bioinspiration & Biomimetics, 2014, Vol. 9.*

- J. Hu, Q. Xiao, Three dimensional effects on the translational locomotion of a passive heaving wing, *Journal of Fluids and Structures, 2014, Vol. 4.*

- D. Pan, J. Hu, X. Shao, Lees-Edwards boundary condition for simulation of polymer suspension with dissipative particle dynamics method, *Molecular Simulation, 2016, Vol 42(4), pp. 328-336.*

- J. Hu, Q. Xiao*, M. Porez, F. Boyer, A coupling method between multi-body dynamics and hydrodynamics for fully resolved simulation of bio-inspired robots, *under review.*

- J. Hu, R. Willden, Unsteady load reduction by individual pitch control of an axial flow tidal turbine in sheared currents, *under review.*

Conferences:

- J. Hu, Q. Xiao and A. Incecik, Dynamic response of a flapping foil with a non-sinusoidal kinematic motion, *the 21st International Offshore and Polar Engineering Conference, (ISOPE), 2011-NK-02, 2011, Maui, Hawaii, USA, Vol.2, pp. 239-245.*

- Q. Xiao, and J. Hu, Parametric study on a cylinder drag reduction using downstream undulating foil, *presented in the 41st American Institute of Aeronautics and Astronautics (AIAA) Fluid Dynamics Conference and Exhibit, 2011-3896, Honolulu, Hawaii, USA.*

- J. Hu, Q. Xiao, Numerical simulation for self-propelled 3d flapping wing -- comparison with two-dimensional case. *6ᵗʰ International Conference on Model Transformation (ICMT), 2012, Harbin, China.*

- J. Hu, Q. Xiao, An exploration of a passive articulated fish-like system, *ASME 2013, 32ⁿᵈ International Conference on Ocean, Offshore and Arctic Engineering, (OMAE), 10808, 2013, Nantes, France.*

- J. Hu, Richard Willden, Unsteady load relief of an axial flow tidal turbine in sheared flow by individual pitch control, *5th Tidal Energy Workshop, 2016, Oxford, UK.*